ENERGY TRANSFER AND SPIN CHANGING IN COLLISIONS OF RYDBERG ATOMS WITH GROUND-STATE MOLECULES AT $\sim 1~\rm K$

Thesis submitted for the degree of

Doctor of Philosophy

at University College London

Klaudia Gawlas

Department of Physics and Astronomy

University College London

07.08.2022

Declaration of Authorship

I, Klaudia Gawlas, confirm that the work presented in this thesis is my
own. Where information has been derived from other sources, I confirm
that this has been indicated in the thesis.
Signed: Date:

Abstract

The resonant energy transfer process between Rydberg He atoms, with n values near 40, and ground-state NH₃ molecules has been investigated experimentally at collision energies, $E_{\rm kin}$, or temperatures $E_{\rm kin}/k_{\rm B} \sim 1$ K. Weak electric fields have been used to observe multiple individual resonances that resulted from the energy transfer between the inversion intervals in NH₃ and $n_{\rm S} \rightarrow n_{\rm P}$ electronic transitions in He. Experimentally, this was achieved through the use of quantum-state-selective detection of the Rydberg atoms, and an intrabeam collision apparatus that allowed low collision energies and long interaction times. The calculated energy-level structure of Rydberg He atoms, which has been used throughout to aid the interpretation of results in this thesis, has been tested experimentally and confirmed to be accurate for the work described here. In addition, this thesis reports on the first observation of collision-induced spin-changing arising from interactions of Rydberg He atoms with paramagnetic ground-state molecules, in this case O₂.

Impact statement

This thesis describes experimental and theoretical developments associated with studies of electric and magnetic dipole interactions between cold gas-phase atoms and molecules. The work presented was the first in which resonant energy transfer, arising from electric dipole interactions between highly-excited Rydberg atoms and polar ground state molecules, was observed at temperatures below 1 K, and controlled using electric fields. It also represents the first observation of spin-changing collisions between highly-excited Rydberg atoms and paramagnetic ground-state molecules performed at low temperature. These results contribute to efforts in the international community working on cold and ultracold gasphase chemistry. The work described is of particular interest in realising fully quantum-state-controlled chemical reactions, and represents an important advance in the fundamental understanding of these reactions.

Acknowledgements

Firstly, I would like to thank my supervisor, Prof. Stephen Hogan, for sharing his extensive knowledge of atomic physics with me. The work described in this thesis would not have been possible without his guidance and many discussions over the last four years. His optimism and extreme work ethic are two things that I aim to bring into anything I end up pursuing. Thanks also go out to my whole research group, especially Adam, Alex, and Matt, who were always happy to help when I needed it.

My support system outside of university has also been strong. My parents and my husband have believed in my ability to complete this work and continuously motivated me, even during the long lockdowns that stretched out time. Lastly, I want to thank all my friends who have shared their PhD journey with me and allowed me to share mine with them.

Contents

1	Introduction			
	1.1	Rydbe	erg-atom–molecule collisions	12
		1.1.1	Resonant energy transfer	13
		1.1.2	Experimental methods	15
		1.1.3	Collisions with NH_3	16
		1.1.4	Collisions with HF and HCl	22
		1.1.5	Collisions with CO	24
		1.1.6	Collisions with nonpolar molecules	25
	1.2	Low-e	energy collision methods	26
		1.2.1	Crossed-molecular beams	27
		1.2.2	Merged beams	30
		1.2.3	Intrabeam collisions	32
2	The	oretica	l Background	34
	2.1	1 Rydberg states of atoms		34
		2.1.1	Fluorescence lifetimes	35
2.2 Stark effect in helium			effect in helium	38
	2.3	Electr	ic dipole transition moment	42

CONTENTS

3	Experimental setup				
	3.1	Supersonic beams			
	3.2	Laser excitation	49		
	3.3	Detection			
4	Tun	nel ionisation of high Rydberg states in strong electric fields	53		
	4.1	Introduction	54		
4.2 Electric field ionisation of Rydberg atoms		Electric field ionisation of Rydberg atoms	55		
		4.2.1 Hydrogenic systems	55		
		4.2.2 Non-hydrogenic atoms and molecules	57		
	4.3	Experiment	62		
	4.4	Results	64		
	4.5	Conclusions	80		
5 Resonant energy transfer in intrabeam collisions of NH					
5	Res	onant energy transfer in intrabeam collisions of NH ₃ with			
5		onant energy transfer in intrabeam collisions of \mathbf{NH}_3 with lberg He atoms	82		
5					
5	Ryd	berg He atoms	82		
5	Ryd 5.1	lberg He atoms Introduction	82 83		
5	Ryd 5.1 5.2	Introduction	828385		
5	5.1 5.2 5.3 5.4	Introduction	8283858791		
5	5.1 5.2 5.3 5.4	Introduction	8283858791		
5	5.1 5.2 5.3 5.4	Introduction	82 83 85 87 91 93		
5	5.1 5.2 5.3 5.4	Introduction	82 83 85 87 91 93 93		
6	5.1 5.2 5.3 5.4 5.5	Introduction	82 83 85 87 91 93 93		

CONTENTS

Bi	Bibliography					
7	Con	clusions and outlook	123			
	6.5	Conclusions	122			
	6.4	Collision-induced spin changing	118			
	6.3	Electric-field-induced spin changing	114			
	6.2	Spin-orbit Stark map calculation	113			
		6.1.1 Cancelling stray magnetic and electric fields	112			

Chapter 1

Introduction

Atoms (or molecules) in which one of the electrons is excited to a state with a high principal quantum number, n, are referred to as Rydberg atoms (molecules). Amaldi and Segre [1] performed the earliest experiments to investigate the collisions of Rydberg atoms with neutral ground-state atoms in 1934. In these experiments they identified the pressure shifts and broadening of Rydberg levels of Na and K caused by collisions with rare gases. Further work by Fermi [2] revealed for the first time the importance of the short-range interaction between the low-energy Rydberg electron of Na and K, and the rare gas atoms. Since then, with the advent of tunable laser systems, the study of Rydberg atoms and molecules has expanded substantially. Rydberg molecules have many applications in spectroscopy, such as in zero kinetic energy photoelectron spectroscopy (ZEKE), and mass-analysed threshold ionisation spectroscopy (MATI) [3]. Cold Rydberg atoms have been investigated for their applications in quantum optics and quantum information science [4]. Rydberg atoms are also of interest in astrophysics. For example, it has been reported that Radio Recombination Lines (RRL) of Rydberg hydrogen atoms can be used to infer electron temperatures in interstellar media [5]. More recently, the synthesis of long-range diatomic molecules known as Rydberg macro dimers [6, 7, 8] has been reported, as has the synthesis of ultra long-range Rydberg molecules in which an excited Rydberg atom is bound to a ground-state atom as a result of the scattering of the Rydberg electron from the ground-state atom within its orbit [9, 10]. Not surprisingly, there is also much interest in Rydberg atoms and molecules in chemical dynamics. This includes collisions of Rydberg atoms with neutral ground-state atoms and molecules, as well as collisions with ions and surfaces [11].

One of the many important characteristics of Rydberg atoms is the large size of the Rydberg electron (excited electron) wavefunction, which scales as n^2 . For n = 100, the expectation value of the radial position operator, or radius of the classical Rydberg electron orbit, is on the order of 1 μ m [11]. Rydberg atoms in such high-n states can therefore possess large electric dipole moments, and as a result these states are highly susceptible to perturbations by external electric fields. Given the almost macroscopic size of Rydberg atoms, they are extremely prone to collisions in many media. For this reason, the study of collisions of Rydberg atoms with neutral atoms and molecules has attracted much attention. Extensive studies in the 1970's and 1980's focused on collisions of Rydberg atoms with neutral ground-state atoms and molecules, such as NH₃, CO and N₂ at room temperature [12, 13, 14]. These studies, along with recent work by Zhelyazkova and Hogan [15, 16] highlighted the importance of the long-range interactions between Rydberg atoms and neutral ground-state molecules, which can

result in resonant energy transfer between the collision partners.

If energy is resonantly transferred between a colliding Rydberg atom and a polar ground-state molecule, a change of state occurs in both collision partners. Experimentally, this can be studied by determining the state of the Rydberg atoms arriving at a detector after the collision, and comparing this to the state in which the Rydberg atoms were prepared. It is therefore imperative in these types of experiments to have a reliable method to selectively detect different Rydberg states following collisions with neutral molecules to understand the energy-transfer process that occurs.

Collisions between Rydberg atoms and polar molecules are investigated because they present themselves as model systems to study resonant energy transfer due to the nature of their interaction during the collision. The long-range dipole—dipole interactions that exist between Rydberg atoms and polar molecules can be exploited to regulate access to shorter range ion—molecule interactions, such as seen in Ref. [17]. Furthermore, there is the prospect of using the results of such investigations to develop techniques that would allow for the non-destructive detection of ground-state polar molecules [18].

In this chapter, a review of resonant energy transfer in gas-phase atom-molecule collisions is given and is followed by a summary of recent studies in the field of cold chemical reaction dynamics. Chapter 2 describes the energy level structure of Rydberg atoms and the methods of calculations used to determine the energy shifts of Rydberg states that result from the presence of electric fields. In Chapter 3, the experimental set-up and methods used in the work presented here are described. The methods of calculation

described in Chapter 2 are then used in Chapter 4 to aid in the interpretation of experiments conducted to investigate ionisation dynamics, and tunnel ionisation rates of Rydberg states of helium in strong electric fields. This is essential for the optimisation of Rydberg-state-selective detection schemes for collision experiments involving Rydberg He atoms and ground-state NH $_3$. Results for these collision experiments performed at temperatures close to 1 K are presented in Chapter 5. Chapter 6 describes the observation of low-temperature spin-changing collisions between Rydberg He and O $_2$. Finally, future directions for the work described in this thesis are given in Chapter 7.

1.1 Rydberg-atom-molecule collisions

Collisions of Rydberg atoms with rare gas atoms, alkali atoms, polar molecules and nonpolar molecules have been studied in a wide range of experimental settings [19]. The particular interactions between the Rydberg atoms and each of these collision partners differ substantially and therefore result in different collision pathways and a wide variation in the observed cross-sections. Resonant energy transfer processes, which are of particular interest in the work described here, have been observed when the collision partner is another Rydberg atom, a polar molecule, and to a much lesser extent, nonpolar molecule.

1.1.1 Resonant energy transfer

When two atoms or molecules collide, energy can be transferred between the internal degrees of freedom of each of the collision partners if the intervals between the energy levels in both match exactly [20]. This process is known as resonant energy transfer. More specifically, the energy released upon, for example, an electronic transition in an atom can excite a rotational, vibrational or electronic transition in a molecular collision partner, if the transitions in the collision partners are equivalent in energy. Therefore, the energy transfer process is dependent on the energy-level structure of the collision partners. Another requirement for resonant energy transfer to occur is that there must be a long-range interaction between the collision partners. This requirement results from the fact that there exists a width to the energy transfer cross-section, the inverse of which corresponds to the minimum time duration that the collision partners must interact to allow energy transfer to occur. To interact long enough for energy transfer to occur, the collision partners therefore must interact at long range.

The types of interactions that occur when a Rydberg atom collides with a ground-state atom or molecule depend strongly on the nature of this collision partner [19]. Considering, first, the simplest case of a collision with another atom. Because in low-energy collisions (i.e., $E_{\rm kin}/k_{\rm B} < 300~{\rm K}$) a ground state atom is not likely to have energetically accessible excited states, the collision with the Rydberg atom may lead to ℓ -mixing of degenerate Rydberg levels, electron spin changing, electron transfer, or an ion-molecule reaction. On the other hand in the collision of a Rydberg atom with a nonpolar molecule such as N_2 , additional interactions are possible.

The longest-range Rydberg-atom $-N_2$ interaction is the dipole–quadrupole interaction. However, not all non-polar molecules have a quadrupole moment. Also, this interaction is shorter-range than the dipole–dipole interaction that exists between a Rydberg atom and a polar molecule, such as CO. Both N_2 and CO, however, have energetically accessible rotational and vibrational states; therefore collisions with Rydberg atoms can induce transitions between the states in the molecules via resonant energy transfer.

The electronic energy levels of an atom or molecule are spaced increasingly closer together at higher principal quantum numbers. Hence, electronic transitions between Rydberg-states in an atom or molecule lead to very small energy changes. These small electronic transition frequencies provide an opportunity to study resonant energy involving Rydberg atoms and low frequency transitions in a neutral collision partner, which are most commonly associated with rotational or fine-structure transitions. The most suitable partner for resonant energy transfer collisions with a Rydberg atom are polar molecules. These fulfil requirements due to the presence of electric-dipole–dipole-coupling, which allow for long-range interactions. The interaction potential associated with this coupling can be expressed as [15]

$$V_{\rm dd}(\vec{R}) = \frac{1}{4\pi\epsilon_0} \left[\frac{\vec{\mu}_{\rm A} \cdot \vec{\mu}_{\rm B}}{R^3} - \frac{3(\vec{\mu}_{\rm A} \cdot \vec{R})(\vec{\mu}_{\rm B} \cdot \vec{R})}{R^5} \right] \tag{1.1}$$

where $\vec{\mu}_A$ and $\vec{\mu}_B$ are electric dipole transition moments for transitions in systems A and B, respectively, and $R = |\vec{R}|$ is the distance between systems A and B. In this equation, the second term in the square brackets describes the angular dependence on the interaction.

1.1.2 Experimental methods

The most commonly used methods to study the collisions of Rydberg atoms with neutral molecules involve the direct measurement of the population changes of the Rydberg states. In these studies, the Rydberg atom is prepared by excitation from the ground-state, which then collides with a beam of neutral molecules and the population of each Rydberg state of interest is subsequently determined by selective electric field ionisation (SFI).

Rydberg atoms have been produced by electron impact and photoexcitation [19]. For experiments involving the collisions of Rydberg atoms with molecules, the chosen method of Rydberg state preparation is laser photoexcitation and generally involves resonance-enhanced two-colour two-photon transitions. For rare-gas atoms such as He or Xe this is often combined with the initial preparation of a long-lived metastable state by electron impact, or in an electric discharge. For example, an electron gun has been used to create metastable ${}^{2S+1}L_I={}^3P_0$ levels of Xe (where S is the total electron spin quantum number, L is the total orbital quantum number, and *J* is the total angular momentum quantum number), followed by photo excitation to $n\ell = nf$ Rydberg states (where n is the principal quantum number and ℓ is the orbital angular momentum quantum number) by a pulsed tuneable dye-laser [12]. Rydberg Rb (ns) and Rb (nd) states have been populated using two photon transitions via the ${}^5P_{3/2}$ intermediate level [13]. The main advantage of the two-step photoexcitation is that, particularly, in the case of the preparation of Rydberg states of molecules, often a single ro-vibrational state can be selected as the intermediate state. Therefore, the number of Rydberg series that are populated following the second excitation step is limited by the selection rules for electric dipole transitions [11]. There is also a technical advantage to this method as the wavelengths required are generally longer than the wavelength that would be required for single-photon excitation. However, in these schemes it is important to consider the decay of the intermediate state such that the rate of losses that occur by this decay process do not exceed the excitation rate.

In order to determine the population of each quantum state following Rydberg atom–molecule collisions, the Rydberg atom is ionised by applying a ramped electric field in the analysis region. The premise of this SFI process is that different Rydberg states will ionise at different field strengths [21]. High n levels are more weakly bound and ionise in lower fields, and hence the electron signal arising from the ionisation of these levels will be observed at the detector at earlier times. It is also possible to distinguish between different ℓ states. This makes it possible to infer the quantum state of the Rydberg atom before it was ionised by measuring the field strength at which ionisation occurred. The SFI spectrum is therefore a measure of electron signal as a function of electric field strength. A schematic diagram of the SFI process is shown in Figure 1.1.

1.1.3 Collisions with NH₃

Collisions of Rydberg atoms with polar NH₃ molecules (dipole moment, μ_{NH_3} , is 1.47 D) have been studied extensively. In fact, the first discrete energy transfer observed in a Rydberg-atom–polar-molecule collision system was between Xe (nf) and NH₃ [22]. In this collision system, it was observed

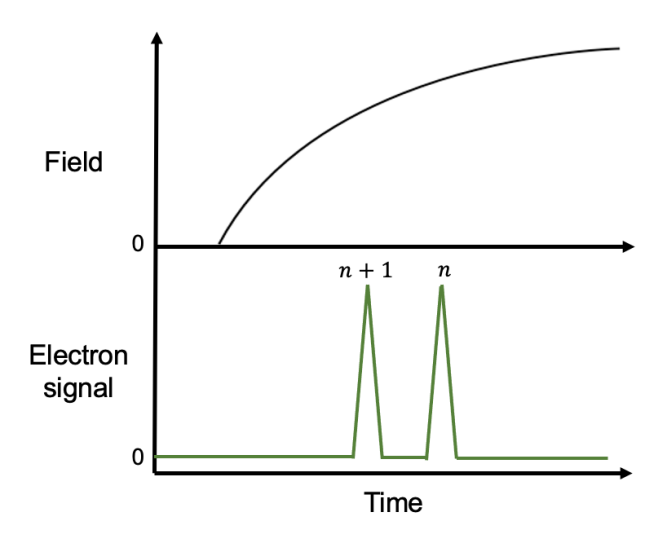


Figure 1.1: A schematic diagram of the selective electric-field ionisation process. A pulsed, slowly-rising, electric field is applied in the analysis region (top) and the electron signal from the ionised Rydberg atoms is collected by the detector as a function of time (bottom). The higher the value of *n* the lower the electric field required to ionise the Rydberg atom, and, therefore, the earlier the electrons will arrive at the detector.

that rotational energy of the NH₃ molecule was converted into electronic energy in Xe (nf), either to further excite the Rydberg atom (n-changing collisions) or to ionise it (collisional ionisation). However, a subsequent study of the same collision system identified an additional mechanism for collision depopulation where a change in the orbital angular momentum of the Rydberg atom occurs [12]. Collisions that induce a change in the orbital angular momentum, i.e. ℓ -changing collisions, differ from n-changing collisions and collisional ionisation of the Rydberg atom because they can be quasi-elastic, hence the internal energy remains the same. A collision between Xe (nf) and NH₃ can therefore proceed via three distinct

mechanisms:

 ℓ -changing collision:

$$Xe(nf) + NH_3 \rightarrow Xe(n\ell') + NH_3$$
 (1.2)

n-changing collision:

$$Xe(nf) + NH_3(J) \rightarrow Xe(n'\ell') + NH_3(J')$$
(1.3)

collisional ionisation:

$$Xe(nf) + NH_3(J) \rightarrow Xe^+(n'\ell') + e^- + NH_3(J')$$
 (1.4)

where *J* is the total rotational angular momentum.

The SFI method was used to identify the Rydberg-states of Xe produced following collisions with NH₃ and is shown in Figure 1.2. In the absence of NH₃, the only signal seen in the SFI spectrum [Figure 1.2(a)] is that from the field ionisation of the parent Xe (31f) state. In the presence of NH₃, the peak corresponding to the field ionisation of the 31f state, labelled as P₀ in Figure 1.2(b), is broadened and slightly shifted compared to the peak seen in Figure 1.2(a). This broadening is attributed to the adiabatic ionisation of products resulting from ℓ -changing collisions, i.e., products with n=31 and $\ell \neq 3$. Adiabatic ionisation refers to the process where as the products pass through the avoided crossings up to the ionisation limit, they remain in the same eigenstate. The peak labelled P₁ is within the range for which an atom with n=31 would ionise in a diabatic manner, i.e. as it goes through avoided crossings a transfer of population can occur to adjacent states. Therefore, this peak is also attributed to the ionisation of products resulting from ℓ -changing collisions. The peaks labelled P₂

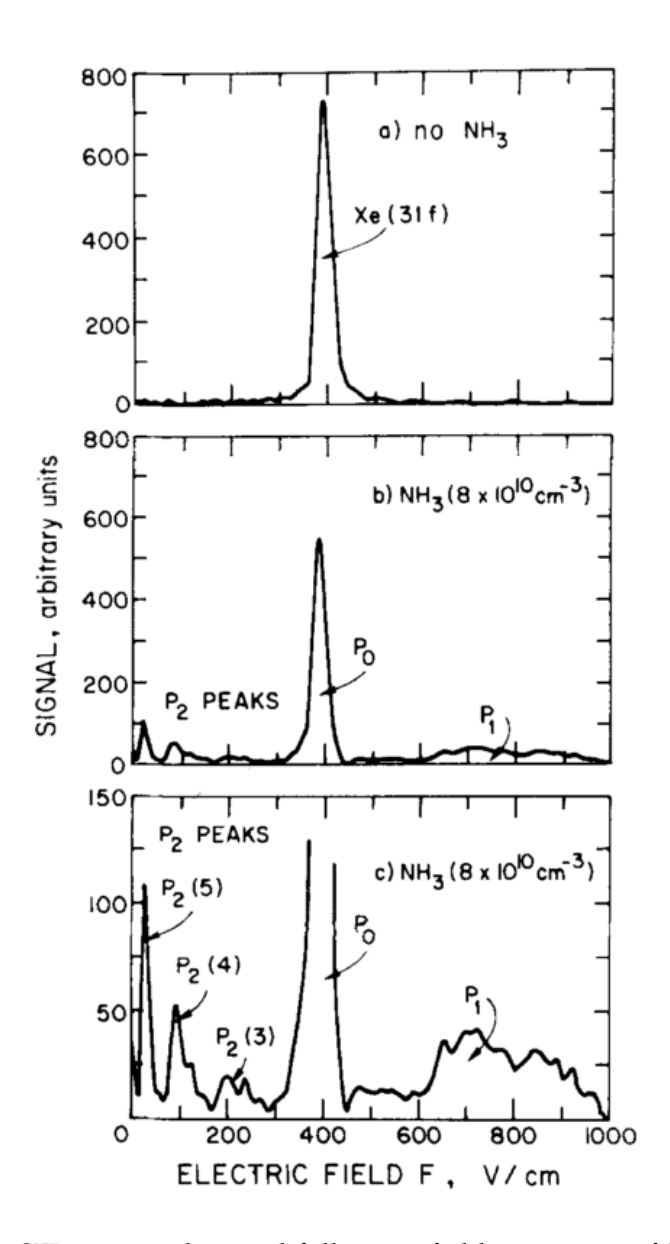


Figure 1.2: SFI spectra observed following field ionisation of Xe (31f) in (a) the absence of NH₃, and (b-c) in the presence of NH₃. Note: The data in (c) represents an expanded view of that in (b). From Ref. [12].

are expanded in Figure 1.2(c) and correspond to the adiabatic ionisation of Xe Rydberg states populated by n-changing collisions. It is also possible

to determine which rotational de-excitation transitions ($\Delta J = -1$) of NH₃ provide the energy for the excitation of the Rydberg atom. For example, the peak labelled P₂(3) corresponds to the $J = 3 \rightarrow J = 2$ rotational transition in NH₃. However, the energy released upon de-excitation of rotational levels for which $J \geq 6$ causes ionisation of the Rydberg atom, i.e., lead to collisional ionisation.

The collisional depopulation rate constants were reported to be large for the Xe (nf) + NH₃ collision system (where n = 22-39), ranging from 1 x 10⁻⁶ to 2 x 10⁻⁶ cm³ s⁻¹. The biggest contribution to the total depopulation rate constant was from n- and ℓ - changing collisions, which were on the order of 10⁻⁷ cm³ s⁻¹, while collisional ionisation was found to be less efficient. As expected, the collisional ionisation rate constant increases with an increase in the value of n of the initially prepared Rydberg state, however, there is no strong dependence of the total depopulation rate constant on the value of n.

Rotational de-excitation of NH₃ is not the only means of inducing transitions in Rydberg atoms in this collision system. The energy released by the inversion transition in NH₃ (inversion between symmetric and antisymmetric sublevels) is ~ 0.8 cm⁻¹ and this energy has been reported to induce ℓ - changes in Rb (ns) and Rb (nd) atoms in the absence of external fields, where $24 \le n \le 49$ [23]. It was found that for n = 30 - 40 the quenching cross-section of Rb (nd) by NH₃ was mostly independent of n, however, the cross-section increased substantially for n > 40, reaching a maximum at $n \sim 46$. The explanation for this n-dependence is that for n > 40, the energy imbalance, which is the difference in energy between

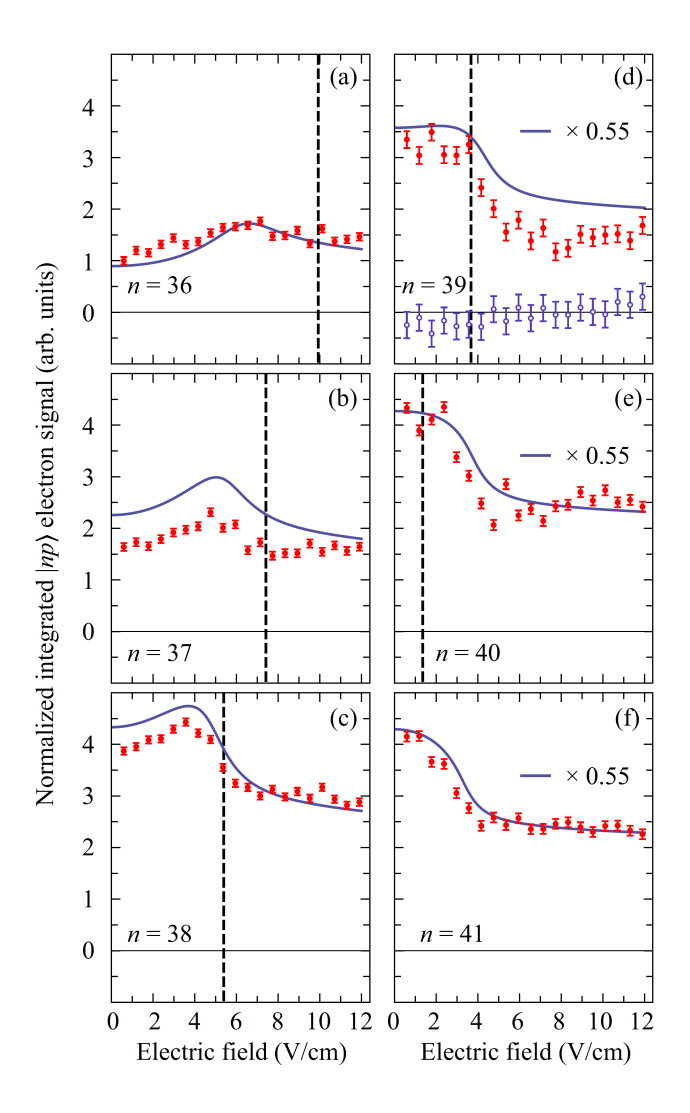


Figure 1.3: (a)-(f) Integrated $|np\rangle$ electron signal (closed circles) obtained following collisions of NH₃ molecules with He Rydberg atoms prepared in $|np\rangle$ states with n=36-41. The data sets are all normalised to the first data point in (a). Solid curves represent the normalised dependence of the calculated electron signal. The vertical dashed lines in each panel indicate the electric field for each n at which the $|ns\rangle \rightarrow |np\rangle$ transition is resonant with the centroid inversion transitions in NH₃. For reference, data recorded in the presence of an NO beam instead of NH₃ is indicated by the open circles in (d). From Ref. [15]

the ℓ -changing transition in the Rb (nd) atom and the inversion transition in NH₃, becomes smaller than 0.5 cm^{-1} . Therefore, the *n*-dependence of the quenching cross-section suggests that the ℓ -changing process is quasiresonant. Similarly, the energy released by the inversion transitions in NH₃ has been observed to induce 1sns ${}^3S_1 \rightarrow 1$ snp 3P_2 transitions in He Rydberg atoms for $36 \le n \le 41$ [15]. A unique aspect of this study, compared with earlier work, is that an electric field (0-12 V/cm) was applied after each $|ns\rangle$ state was prepared. The electron signal from the resulting $|np\rangle$ state following collisions with NH₃ was then measured as a function of the strength of this electric field and is shown in Figure 1.3. As the electric field strength was varied, the energy of the ns to np transition reduced due to the Stark effect. Hence, if this transition was slightly higher in energy than the inversion transitions in zero field, the two can be tuned into resonance by applying an electric field. Indeed, it was observed that the electron signal from the $|np\rangle$ state varied as the electric field was changed, and the highest electron signal was seen at the electric field strength when the $|ns\rangle$ to $|np\rangle$ transition was close to 0.8 cm⁻¹. This electric field dependent change in the measured electron signal for each n state investigated confirmed the resonant character of the energy transfer process between the He Rydberg atoms and ground-state NH₃.

1.1.4 Collisions with HF and HCl

Related experiments involving collisions of Xe (nf) with other polar molecules, HF ($\mu_{HF} = 1.82$ D) and HCl ($\mu_{HCl} = 1.08$ D), were reported to have total depopulation rate constants on the same order as the Xe (nf) and NH₃ colli-

sion system discussed above and proceed via the three mechanisms given by reactions (1.2)–(1.4) [24, 25]. The SFI spectra recorded following the collisions of Xe (23f) with HF was observed to have a peak corresponding to energy transfer to the Xe (21 ℓ) state [24]. This peak suggested, for the first time, that changes in the electronic energy of the Rydberg atom could induce rotational transitions in HF,

$$Xe(nf) + HF(J = 0) \rightarrow Xe[(n-2)\ell] + HF(J = 1).$$
 (1.5)

It is also important to note that an analogous peak was not seen in the SFI spectra of Xe (26f) and Xe (27f), which were also collided with HF molecules in the same study. The energy imbalances for reaction (1.5), i.e. the energy difference between the electronic transition in Rydberg Xe and the rotational transition in HF, are 1.5, 2.5 and 2.6 cm⁻¹ for the transitions from the 23f, 26f, and 27f states, respectively. This suggests that energy transfer from the Rydberg atom to HF is dependent on the energy match between the electronic and rotational levels involved. The same reasoning was proposed to explain why the rate constant for the energy transfer from Rb (ns) to rotational states in HF decreased as the energy imbalance increased [26]. This is shown in Figure 1.4, where when the energy imbalance for the reaction is below 1 cm⁻¹ the rate constant is on the order of 10^{-7} cm³ s⁻¹ but when this is increased the rate constant decreases to below 10^{-7} cm³ s⁻¹.

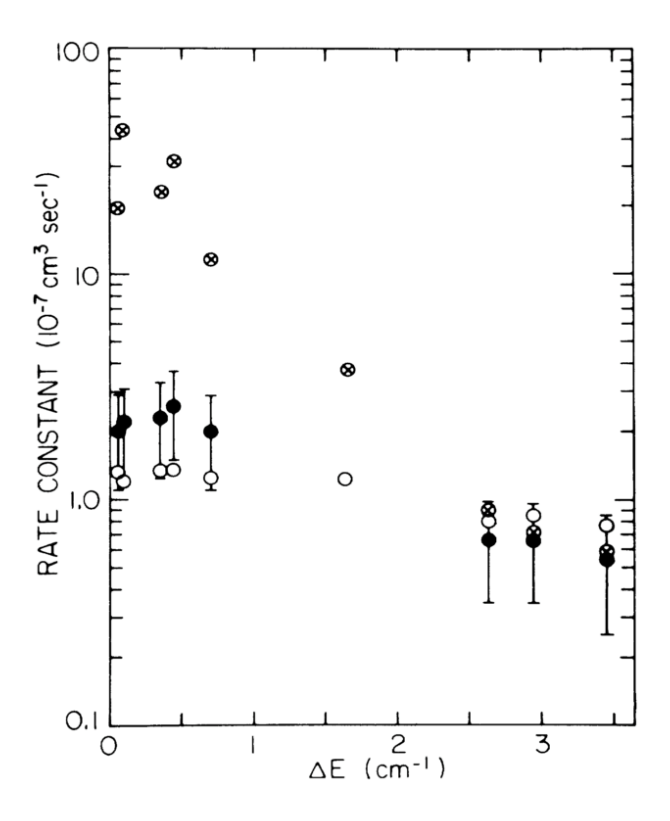


Figure 1.4: The dependence of the rate constant for reaction (1.5) on the energy imbalance, where filled black circles show observed values, open circles and circles with crosses show the rate constants calculated using a semiclassical model, and impulse approximation respectively. From Ref. [26].

1.1.5 Collisions with CO

Reactions (1.2)–(1.4) that were observed for collisions with polar molecules were also reported for the collision of Rb ($n\ell$) and CO, which has a small electric dipole moment in its ground electronic state ($\mu_{CO}=0.11$ D) [13]. The observed cross-sections were compared to cross-sections calculated using a model that only considered the Rydberg-electron–CO interaction.

This model includes a short-range interaction that leads to ℓ -changing collisions, and a long-range (dipole-dipole) interaction that leads to nchanging collisions and collisional ionisation. The observed cross-sections were highest for the *n*-changing process and the good agreement of these with the calculated values suggest that the long-range interaction between the Rydberg electron and molecular dipole is dominant, even in collisions with molecules that are weakly polar, leading largely to n-changing collisions. The quasi-resonant nature of the *n*-changing process was further highlighted in this collision system; it was found that the energy imbalance must be $\leq 1-2$ cm⁻¹ for this process to be efficient. However, the total depopulation cross-sections (including n-changing, ℓ -changing and collisional ionisation) measured following the collision of Rb ($n\ell$) with CO was reported to be two orders of magnitude smaller than the cross-sections for collisions of Xe (nf) with the more polar molecules (NH₃, HF and HCl) discussed above [23]. These comparisons suggest that even though resonant energy transfer occurs between Rydberg atoms and CO, and is the dominant process that takes place in such collisions, the magnitude of the cross-section is dependent on the dipole moment of the neutral molecule. The larger the dipole moment, the stronger the interaction between the collision partners and so the bigger the cross-section.

1.1.6 Collisions with nonpolar molecules

Collisions of Rydberg atoms with molecules that are nonpolar, e.g., N_2 and SF₆, have also been investigated [14, 27]. These studies have highlighted the difference in interactions of polar and nonpolar molecules with

Rydberg atoms. The longest-range interaction that is possible between a Rydberg atom and a non-polar molecule is the dipole–quadrupole interaction. This interaction is weaker than the dipole–dipole interaction, therefore n-changing collisions are expected to contribute little to the total depopulation cross-section. For the Rb (ns) + N_2 collision system, it was reported that less than 10% of the calculated cross-section arises from n-changing collisions [14]. Instead, the main depopulation pathway involves short-range (electron– N_2) interactions leading to the quasi-elastic process of ℓ -mixing in the Rydberg atom. The lack of a strong long-range interaction between the Rydberg atom and a nonpolar molecule leads to smaller total depopulation rate constants when compared with polar molecules. For example, the total depopulation rate constant is on the order of 10^{-7} cm 3 s $^{-1}$ for the Xe (nf) + SF $_6$ collision system, which is an order of magnitude lower than reported for the collisions with polar molecules [27].

1.2 Low-energy collision methods

A natural development in the investigation of collisions of Rydberg atoms with neutral ground-state molecules described in Section 1.1 is to perform the experiments at low energies. Low-energy collision methods not only allow replication of the conditions for reactions that are naturally prevalent in cold environments, such as the interstellar medium, but they also have other advantages that allow for more detailed study of chemical dynamics. A few of these advantages are [28]:

(i) The reaction dynamics are significantly simplified because only a few

partial waves are involved, and so the specific role of each reactant can be established

- (ii) Long-range interactions and non-adiabatic effects can be probed
- (iii) Parameters such as the rate coefficients, collision cross-sections, and branching ratios can be determined with high precision due to the higher achievable collision energy resolution
- (iv) New chemistry and unexpected chemical behaviour may be uncovered

For many years supersonic beams have been used to produce internally cold samples of gas-phase molecules. However, the translational kinetic energy of the particles can remain high and result, in general, in high collision energies with a collision partner. The most effective methods to achieve low collision energies in gas-phase atom-molecule collision studies are described in the following sections.

1.2.1 Crossed-molecular beams

The energy of a collision, E_{coll} , between two particles crossing at an angle θ with a reduced mass, $\mu = \frac{\mu_1 \mu_2}{\mu_1 + \mu_2}$, with μ_1 and μ_2 the masses of the two collision partners, and respective speeds of ν_1 and ν_2 is given by [29]

$$E_{\text{coll}} = \frac{1}{2}\mu(\nu_1^2 + \nu_2^2 - 2\nu_1\nu_2\cos\theta). \tag{1.6}$$

It is evident from this expression that the relative speeds of the collision partners, as well as the crossing angle are important in determining the collision energy. One simple way to decrease the collision energy is to reduce the crossing angle of the two beams. An alternative to this method is to utilise Stark or Zeeman deceleration to remove the translational kinetic energy from the particles in a supersonic beam.

Studies where the crossing angle of two beams was varied have had a strong focus on exploring inelastic collisions between important astronomical molecules, such as H₂ and H₂O, and using the results to test quantum mechanical calculations of the corresponding potential energy surfaces [30, 31]. For example, in the study of the CO-para-H₂ system [30], collisions performed near the threshold region of the $CO(J = 0 \rightarrow J' = 1)$ rotational transition at 3.85 cm⁻¹ revealed resonances in the integral cross sections corresponding to quasibound states that would have otherwise not been observed at high collision energies. This is because the quasibound states correspond to particular partial waves with a fixed J value, which become averaged out when the collision angle is high, so that the information is lost. Such experiments can, therefore, provide information on the contribution of each partial wave to the cross section in a collision. One study where this has been particularly clear is that of the O₂-para-H₂ collision system, where the low energy resonances revealed that the collision-induced transition of O_2 ($N = 1, J = 0 \rightarrow N = 1, J = 1$) is caused by the partial waves with J=2 to 4 [32]. Quantum mechanical calculations have long predicted low energy resonances and are in good quantitative agreement with the results of these experiments [33, 34].

Most recently, the cross sections for the first rotational excitations for para- and ortho- H_2O arising following inelastic collisions with H_2 have

been measured between collision energies corresponding to 15 to 105 cm⁻¹ [31]. The good agreement with theoretical cross-sections for this system validate the potential energy surface used for the calculation and, therefore, the rate coefficients calculated using this potential can be used with confidence to analyse interstellar spectra.

If one of the collision partners of interest in a particular experiment is a polar molecule, then Stark deceleration can be used to slow down a beam of these particles to achieve low collision energies. This approach works on the premise that when polar molecules in a low-field-seeking sublevel enter an inhomogenous electric field they can gain Stark energy, which results in a loss of kinetic energy [35]. Employing a series of such electric field gradients that the molecule passes through, and where each is rapidly switched off when the molecules approach the field maxima can, therefore, bring them to a standstill. A 2.6 m-long Stark decelerator has been used to slow a beam of NO radicals that then crossed a beam of He atoms at a 45° angle to study the scattering process using velocity map imaging [36]. The collision energy in these experiments was varied by tuning the velocity of decelerated NO between 350 and 460 m/s to reach energies between $E_{kin}/hc = 13$ and 19 cm⁻¹. Scattering resonances at collision energies close to the rotational transitions in NO were observed in the differential cross sections, and the exact partial waves involved in the formation of quasi-bound states were identified as well as the outgoing waves. In a similar study of the $NO + H_2$ collision system, an observed resonance structure separated two NO-H₂ potentials and thus pushed the need for even greater accuracy in the calculations of the intermolecular interaction potentials [37].

1.2.2 Merged beams

If collision energies below 1 K are required, the velocities of the beams would need to be approximately equal and the crossing angle between the two beams in a crossed beam collision apparatus would need to be 0°, in other words, one of the beams must be guided onto the axis of the other. In a collision system where one of the components is paramagnetic and the other not, a curved magnetic guide can be used to direct low-fieldseeking paramagnetic species onto the axis of the other beam [38, 39]. This method has been utilised to study chemi-ionisation reactions, where an electronically excited species collides with a target species, which either results in Penning ionisation or associative ionisation. The merged-beams study of the Penning ionisation reaction of Ar and H₂ with metastable He allowed for the observation of orbiting resonances at collisions as low as $E_{\rm kin}/k_{\rm B}$ = 8.7 mK [38]. Merged beams have also been used to study the effect that the orientation of the magnetic dipole moment in metastable Ne (Ne*) has on the branching ratio of Penning to associative ionisation in collisions with N_2 [40]. In this study, a 1.8 m-long magnetic guide was used to bend a beam of Ne* onto the axis of an N₂ beam, and an external magnetic field was applied to control the orientation of the Ne* atoms in the collision region. It was found that above 30 K the orientation of the Ne* had a significant effect on the outcome of the collision. However, below 30 K steric control over the Ne* molecule was no longer possible due to dynamic reorientation, this occurs when the force from the interatomic potential overcomes the force created by the external magnetic field. Similar orientation studies have also been performed with ND₃ and Ne* [41].

Another important set of reactions that the merged beam technique has been applied to is in the study of ion-molecule reactions. Ions are highly susceptible to stray electric fields and this makes ion-molecule reactions difficult to study at very low temperatures or collision energies, i.e., < 1K. However, due to the large size of a Rydberg electron orbit, or charge distribution, compared with the maximal impact parameter, the collision of the Rydberg atoms or molecules ion core with another groundstate molecule can be studied while ignoring the Rydberg electron as it is considered only a spectator in the reaction (see, for example, Ref. [42]). This has the added benefit that the Rydberg electron acts to shield the reactants from stray electric fields. This approach has been used to study the $H_2^+\,+\,$ $H_2 \rightarrow H_3^+ + H$ reaction, where Rydberg H_2 molecules were merged with a beam of ground-state H₂ using a Rydberg-Stark deflector and accelerator [17]. The collision energy was tuned between 10 K and 300 mK by varying the temperature of the pulsed valve that generated the beam of groundstate H_2 . The yield of H_3^+ ions in this work revealed that the rate coefficient for the reaction is enhanced at collision energies below 1 K. This points at a deviation from the classical Langevin-capture model. The explanation suggested for this is that the interaction between the charge of H₂⁺ and the ground-state ortho- H_2 (J = 1) molecules, which scales as $1/R^3$, leads to an anisotropy in the long-range scattering potential at low-energies. More recently, a similar setup was used to study the energy dependence of the rates of reactions in the He⁺ + NH₃ collision system at collision energies between 0.2 and 40 K [43]. Three classes of rotational states of NH₃ were identified to exist in the electric field of the He⁺ atom, and all three showed different low-energy capture behaviour. High-field-seeking states of NH₃ exhibited strongly enhanced rate coefficients, while low-field-seeking states caused a suppression of the rate at low collision energies. In addition, it has been suggested that the effect of molecular orientation in ion–molecule reactions can be investigated by combining a buffer gas cell, and a quadrupole guide apparatus, with a linear Paul ion trap to gain more detailed information on the dynamics and kinetics of the reaction [44].

1.2.3 Intrabeam collisions

An intrabeam collision set-up differs from the methods described above in that it requires only a single molecular beam source. Specifically, the reactants (collision partners) of interest undergo a simultaneous expansion into vacuum to form a single beam. In recent studies, this has been exploited together with the velocity slip between particles with different masses to produce a small velocity difference between the reactants and achieve low collision energies. This technique operates on the premise that if the 'faster' reactant is located at the back part of the beam, then it will catch up to the 'slower' reactant at an interaction region, where the reaction can take place.

In intrabeam studies of the ℓ -changing collisions between Xe Rydberg atoms and ground-state Xe atoms, collision energies as low as 2.5 mK were achieved [45]. Furthermore, control over the relative velocities of the reactants was attained using a dual-slit chopper, which allowed the collision

energy to be tuned between $E_{\rm kin}/k_{\rm B}=200$ and 450 mK. It was noted in this work that this method could be easily extended to other reactants. The rotationally inelastic collision of HD($\nu=1,J=2$) and D₂ was subsequently studied at temperature close to 1 K using this intrabeam method [46]. In that work, laser-induced alignment was utilised to prepare HD($\nu=1,J=2$) molecules aligned parallel or perpendicular to the laboratory-fixed relative velocity vector. It was found, through the scattering angular distributions, that there was a strong stereodynamic preference for the perpendicular alignment.

Chapter 2

Theoretical Background

2.1 Rydberg states of atoms

In the following, the term "Rydberg atom" is used to refer to atoms that have only one electron that is highly excited. The energy of each bound eigenstate in a Rydberg atom is given by the modified Rydberg formula [47]

$$E_{n\ell} = E_{\text{ion}} - \frac{hcR_M}{(n - \delta_{n\ell})^2}$$
 (2.1)

where E_{ion} is the energy associated with the Rydberg series limit, h and c are Planck's constant and the speed of light in vacuum respectively, R_M is the Rydberg constant corrected for the reduced mass of the atom, n is the principle quantum number, and $\delta_{n\ell}$ is the quantum defect. The quantum defect is dependent on the principal and orbital angular moment quantum numbers, n and ℓ , and reflects the penetration of the Rydberg electron into the electron distribution of the ion core. In hydrogen, where there is only one electron, the quantum defects are zero for all ℓ values; hence, to first

order, all states with the same value of n are degenerate in the absence of external electric or magnetic fields as shown in Figure 2.1. In the case of non-hydrogenic atoms, i.e., those with more than one electron such as helium, the quantum defects are non-zero and therefore states with same n but different ℓ are not degenerate. The quantum defect is larger for lower ℓ values because the electron is able to penetrate into the ion core better, resulting in a lower energy of the state than for higher ℓ values of the same n. However, typically only states with values of $\ell \le 3$ are lowered in energy substantially in non-hydrogenic atoms (also shown in Figure 2.1). The quantum defect tends towards zero as ℓ is increased (i.e., for $\ell > 3$) and therefore high ℓ states of the same n are almost degenerate.

2.1.1 Fluorescence lifetimes

When an electron in an atom is excited, the excited Rydberg state is energetically far from equilibrium and will eventually decay by spontaneous emission directly to the ground state, or in a series of transitions to lowerlying states. In this decay process a photon is emitted usually with a longer wavelength than the photon used for photoexcitation. The time taken for this to occur is the radiative lifetime, or more specifically, the fluorescence lifetime and it is given by the inverse of the sum of the Einstein-A coefficients associated with all the allowed decay pathways from a Rydberg state $|n\ell\rangle$ to the lower-lying states $|n'\ell'\rangle$ [49], i.e.,

$$\tau_{n\ell} = \left[\sum_{n'\ell'} A_{n'\ell',n\ell}\right]^{-1}.$$
 (2.2)

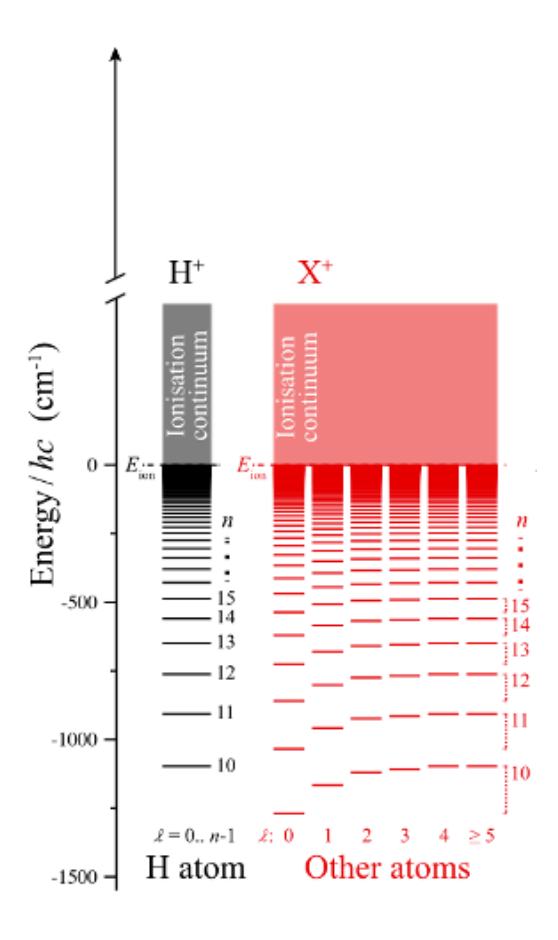


Figure 2.1: The Rydberg states of hydrogen and other non-hydrogenic atoms (adapted from Ref.[48]).

where *A* is the Einstein-A coefficient related to the rate of spontaneous emission of light.

For hydrogen, the np Rydberg states are dominated by the decay to the ground state and this results in short fluorescence lifetimes, while lifetimes of $\ell \neq 1$ Rydberg states are longer because decay to the ground-state via a single-photon transition is not possible [48]. This is in contrast to the fluorescence lifetimes of alkali atoms. The fluorescence lifetimes have been measured for low- ℓ Rydberg states of alkali atoms such as Na[50]

and Rb[51] using laser induced fluorescence for n < 15 and a time-delayed electric field ionisation method for n > 15. Comparing the lifetimes of Na Rydberg states to equivalent hydrogenic levels, it can be deduced that the np and nd lifetimes of the former are factors of 50 and 2 longer than the latter, but the lifetime of ns states in Na are $\sim 30\%$ shorter than their hydrogenic counterparts [19]. In general, the fluorescence lifetimes of individual low- ℓ states scale as $\sim n^3$, so that, for example, the fluorescence lifetime is greater than 20 μs for low- ℓ states where n > 30.

Apart from natural decay, there are processes that can decrease the measured lifetime of an excited state. Fluorescence lifetime calculations for alkali atoms have been made using a Coulomb approximation along with corrections for the effects of core polarisibility, spin-orbit interactions and blackbody radiation [52]. The good agreement of these calculations with the measured lifetimes highlighted the significant effect that blackbody radiation has on an excited state's lifetime, especially for higher n states and at higher temperatures, i.e., temperatures ~ 300 K. Collisional depopulation can also decrease the lifetime of a Rydberg state, again, especially for higher n states [53, 54]. The effect of collisions on the lifetime can be suppressed through the use of ultracold techniques and keeping the density of the Rydberg atoms low [55].

The application of external electric fields results in Rydberg atoms with an even longer fluorescence lifetimes than the zero-field equivalent states because of the ℓ -mixing induced by these fields. The fluorescence lifetime of ℓ -mixed Stark states scales approximately with n^4 (compared with n^3 scaling for zero-field pure low- ℓ states). Consequently, Stark states with

the highest electric dipole moment that can be generated via a two-photon excitation process results in fluorescence lifetimes on the order of $100\mu s$ when n > 30 [56].

2.2 Stark effect in helium

To calculate the energy-level structure of a non-hydrogenic Rydberg atom such as helium, a Hamiltonian matrix in spherical coordinates is constructed and its eigenvalues evaluated. In the presence of a homogenous electric field, $\overrightarrow{F} = (0,0,F)$, applied in the *z*-direction, the Hamiltonian operator for a Rydberg atom can be expressed as

$$\hat{H} = \hat{H}_0 + \hat{H}_{\text{Stark}} \tag{2.3}$$

$$=\hat{H}_0 + eFr\cos\theta \tag{2.4}$$

where \hat{H}_0 is the Hamiltonian in the absence of the electric field, \hat{H}_{Stark} is the Stark Hamiltonian that describes the interaction with the electric field, e is the electron charge, and r and $\cos\theta$ relate to the radial and angular positions of the electron. Neglecting spin-orbit effects, the zero-field Hamiltonian matrix, \hat{H}_0 , is diagonal in the $|n\ell m>$ basis and the corresponding matrix elements can be evaluated using Equation 2.1. In spherical polar coordinates, $\hat{H}_{\text{Stark}} = eFr\cos\theta$, where e is the charge of the electron. The matrix elements for the Stark Hamiltonian can, therefore, be written as

$$\hat{H}_{\text{Stark}} = \langle n'\ell'm'|eFr\cos\theta|n\ell m\rangle \tag{2.5}$$

and separated into radial and angular parts [56]

$$\hat{H}_{\text{Stark}} = eF \langle \ell' m' | \cos \theta | \ell m \rangle \langle n' \ell' | r | n \ell \rangle$$
 (2.6)

Since $\cos\theta = \sqrt{\frac{4\pi}{3}} Y_{10}(\theta\phi)$, the angular component of the Stark Hamiltonian can be evaluated by expanding in terms of the spherical harmonics, $Y_{\ell m}(\theta\phi)$. As a consequence, only angular matrix elements for which $\Delta m = 0$ and $\Delta \ell = \pm 1$ are non-zero. Therefore, the presence of an external field gives rise to mixing of states that differ by one quantum of orbital angular momentum but there is no m-mixing. Evaluation of the non-zero angular integrals can be achieved analytically by exploiting the properties of spherical harmonics [57], which give rise to the expressions [56]

$$\langle \ell + 1m | \cos \theta | \ell m \rangle = \sqrt{\frac{(\ell+1)^2 - m^2}{(2\ell+3)(2\ell+1)}}$$
 (2.7)

$$\langle \ell - 1m | \cos \theta | \ell m \rangle = \sqrt{\frac{\ell^2 - m^2}{(2\ell + 1)(2\ell - 1)}}$$
 (2.8)

While the angular integrals can be determined analytically, the radial component of Equation 2.6 cannot for non-hydrogenic systems. Instead, the Numerov method is employed to evaluate the radial integrals numerically for each pair of states [19, 56]. This method assumes that outside a certain radius, the Rydberg electron experiences a purely Coulombic potential. Integration is performed inwards from a large r, defined as a position outside the classical turning point of the Rydberg electron, to a predetermined, small, r. Over this range, however, the period of the Coulombic wavefunctions changes drastically and the integrals must be performed by either using an adaptive integration step-size or a change

of variable. The latter method is used in the work described here, where a change of variable to $x = \ln(r)$ introduces a logarithmic scaling yielding the wavefunctions $X(x) = \sqrt{r}R(r)$. The Numerov method can then be used to solve the second-order differential equation

$$\frac{\mathrm{d}^2 X}{\mathrm{d}x^2} = g(x)X\tag{2.9}$$

where

$$g(x) = 2e^{2x}[V(x) - E] + (\ell + 0.5)^2$$
(2.10)

with V(x) = -1/r and $E = -1/(2n*^2)$ in atomic units. Choosing the logarithmic stepsize h = 0.001, the recursion relation [58]

$$X_{i+1} = \frac{X_{i-1}(g_{i-1} - \frac{12}{h^2}) + X_i(10g_i + \frac{24}{h^2})}{(\frac{12}{h^2} - g_{i+1})}$$
(2.11)

can be used to determine the radial matrix elements

$$\left\langle n'\ell'|r^{\sigma}|n\ell\right\rangle = \frac{\sum_{i} X_{i}' X_{i} r_{i}^{2+\sigma}}{(\sum_{i} X_{i}'^{2} r_{i}^{2} \sum_{i} X_{i}^{2} r_{i}^{2})^{\frac{1}{2}}}$$
(2.12)

This method of calculating the energy-level structure of Rydberg atoms was first implemented for alkali metal atoms [56].

The calculated energy levels are displayed as a function of electric field for triplet Rydberg states in He near n=37-39 in Figure 2.2(a). At lower fields, the low- ℓ states experience quadratic Stark shifts, while high- ℓ states experience linear Stark shifts. At electric fields higher than the Inglis-Teller limit, $F_{\rm IT}=F_0/(3n^5)$ (F_0 is the electric field strength in atomic units), where manifolds of states that differ in their value of n by +1 first cross, avoided crossings are formed between adjacent energy levels. An example of such a crossing is marked within the green circle in Figure 2.2(a) and is shown in

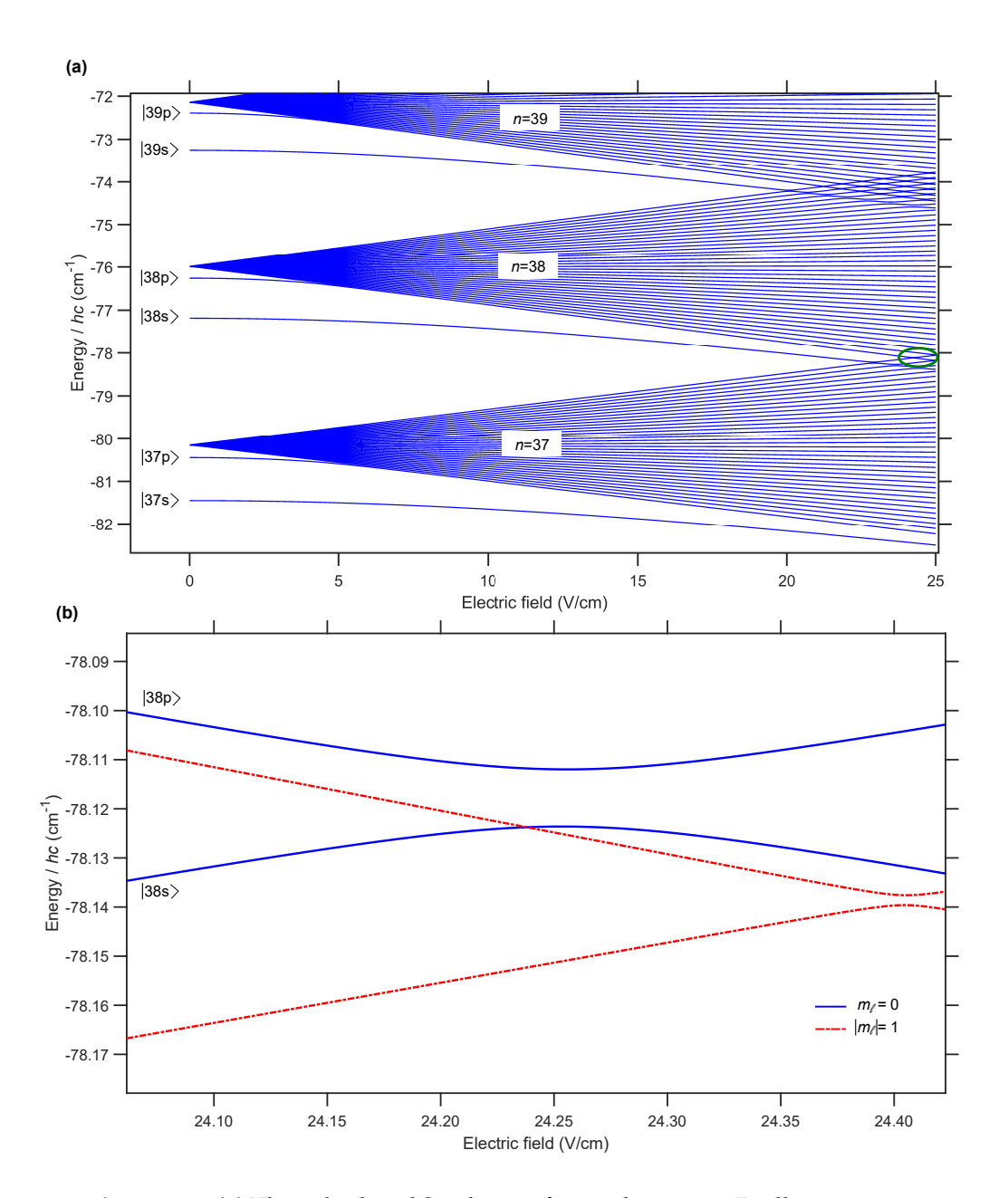


Figure 2.2: (a) The calculated Stark map for triplet $m_\ell = 0$ Rydberg states in He near n = 38, which are of interest in this work. (b) Avoided crossings formed between adjacent $m_\ell = 0$ states (continuous blue curves) and adjacent $|m_\ell| = 1$ states (dash-dotted red curves) that are found within the green circle in (a).

greater detail in Figure 2.2(b), along with another avoided crossing formed between two different $m_{\ell}=1$ states.

The basis set used in calculating a Stark map depends on the principle quantum number and electric fields of interest. For example, a convergence test of the calculated eigenenergies shows that only states from n = 36 to n = 40 need to be included to get an accuracy of 0.001 V/cm (1 MHz) for the Stark map at n = 38 in He up to the Inglis-Teller limit. In the work described here, a range of electric field values are of interest, therefore, for each experiment, separate convergence tests were performed.

2.3 Electric dipole transition moment

An electromagnetic field can drive a transition between two states $|n\ell m\rangle$ and $|n'\ell'm'\rangle$, the strength of this transition is governed by the electric dipole transition moment between them

$$d_{n'\ell'm',n\ell m} = \left\langle n'\ell'm'|\hat{\vec{\mu}}|n\ell m\right\rangle \tag{2.13}$$

$$= -e \left\langle n'\ell'm'|\hat{\vec{r}}|n\ell m\right\rangle \tag{2.14}$$

where $\hat{\vec{\mu}} = -e\hat{\vec{r}}$ is the electric dipole operator, with e being the electron charge.

If the electromagnetic field is linearly polarised in the *z*-direction then $\vec{r} = (0,0,z)$ and Equation 2.13 can be separated into angular and radial components when expressed in spherical coordinates

$$-e \langle n'\ell'm'|\vec{z}|n\ell m\rangle = -e \langle n'\ell'|r|n\ell\rangle \langle \ell'm'|\cos\theta|\ell m\rangle$$
 (2.15)

This is akin to the method used in Section 2.2 to calculate the Stark energy-levels. Here, Equation 2.15 leads to the selection rules for electric dipole transitions that $\Delta \ell = \pm 1$ and $\Delta m = 0$ based on the angular integrals in Equations 2.7 and 2.8. Again, the radial integrals are evaluated using the Numerov method.

The electric dipole transition moments for $\Delta \ell = \pm 1$ transitions are of particular interest in the work described here. For principle quantum numbers of n>35, the electric dipole transition moment for an ns to np transition is ≥ 3000 D in zero electric field. To calculate the electric dipole transition moment in the presence of an external electric field, the eigenvectors of the complete Hamiltonian described in Section 2.2 are used. In general, for an ns to np transition between triplet Rydberg states in He, the electric dipole transition moment decreases as the electric field strength increases.

Chapter 3

Experimental setup

For the experiments described in Chapters 4-6, the experimental set-up used is similar with small variations. These variations are noted in each respective chapter. The general setup that is applicable to all three experiments is given here.

A schematic diagram of the experimental setup is shown in Figure 3.1. A pulsed supersonic beam of metastable helium atoms in the $1s2s\ ^3S_1$ level was generated in a dc electric discharge at the exit of a pulsed valve operated at a repetition rate of 50 Hz [59]. In the discharge, a dc potential of $+250\ V$ was applied to a metal anode positioned $\sim 1\ mm$ away from the valve opening. This discharge was seeded by a constant current of electrons flowing from a heated tungsten filament positioned $\sim 30\ mm$ further downstream. The metastable beam of atoms generated in this discharge, traveling with a longitudinal speed of $2000\ m/s$, was collimated by a 2-mm-diameter skimmer and stray ions were filtered by applying a potential difference of $200\ V$ across parallel plates separated by $10\ mm$, before it entered the Rydberg state photoexcitation region of the apparatus. The use

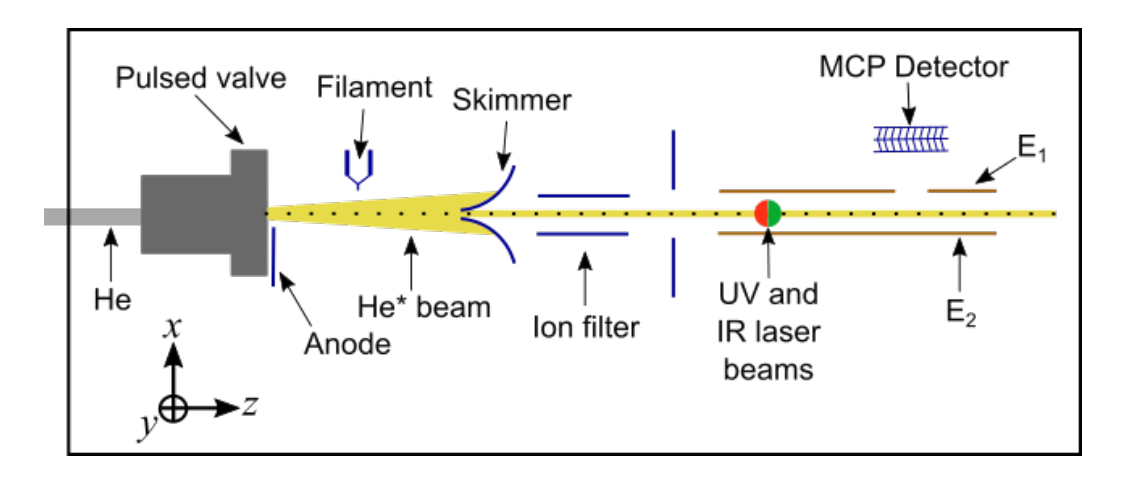


Figure 3.1: Schematic diagram of the experimental setup. A dc electric discharge at the exit of a pulsed valve created a beam of metastable helium atoms in the 1s2s 3S_1 level. This beam was then collimated and travelled through the skimmer into the photoexcitation and interaction region between the two parallel electrodes. Here, the helium atoms were excited in a two-photon excitation scheme to the Rydberg states of interest. Following photoexcitation, an electric field pulse was applied to electrode E_1 to probe the interactions of interest in this thesis. Lastly, the Rydberg atoms were ionised by applying a slowly rising potential to electrode E_2 , and the resulting electron were collected by the MCP detector. See text for more detail.

of the state-selective detection method means that any other impurities left in the beam at this point would not interfere with the interpretation of the data. Excitation of the atoms to the desired Rydberg states took place between two parallel copper electrodes labeled E_1 and E_2 in Figure 3.1. These electrodes were separated by 13 mm. The Rydberg states were prepared using a resonance-enhanced two-photon excitation scheme, with UV and IR laser beams [60], in the following sequence: $1s2s^3S_1 \rightarrow 1s3p^3P_2 \rightarrow 1sns/nd$. In all 3 experiments a short electric field pulse was applied to electrode E₁ following the photoexcitation to induce interactions or probe tunnel ionisation. This field is on the order of 1 V/cm and corresponds to a Stark shift of the NH₃ of less than 0.001 cm⁻¹, hence, the effect of the electric field on NH₃ can be neglected. After the potential on electrode E₁ returned to its initial value, a slowly rising potential was subsequently applied to electrode E₂ to ionise the surviving bound Rydberg atoms. The electrons resulting from this ionisation step were accelerated through an aperture in E₁ to a microchannel plate (MCP) detector and collected for detection.

It was important to minimise stray magnetic fields as well as stray electric fields in the experiments because these can shift energy levels significantly. Magnetic field cancellation was performed using coils that were wound on the outside of the vacuum chamber. While stray electric fields were minimised by varying the low-level voltage applied to electrode E_2 during the electric field pulse. These methods are explained in detail in subsequent chapters.

For the collision experiments described in Chapters 5 and 6, an intrabeam collision method was employed as described in Chapter 1.2.3. This resulted in low collision energies with minimal complexity in the implementation.

3.1 Supersonic beams

In supersonic expansions, gas from a high pressure reservoir expands through a small circular nozzle into a lower pressure region generating a beam with a well-defined kinetic energy, low internal temperature and low relative translational velocity. This supersonic expansion process is adiabatic and isentropic when the source pressure is high, hence, the effects of gas viscosity and heat transfer may be ignored [61]. For a gas with a heat capacity at constant pressure, C_p , the maximum flow velocity of the gas generated by the expansion is [62]

$$v_{\text{max}} = \sqrt{\frac{2C_p T_0}{m}} \tag{3.1}$$

where T_0 is the temperature of the source reservoir, and m is the atomic (or molecular) mass. Since $C_p = \frac{5}{2}k_B$ for an ideal monoatomic gas, the maximum velocity for He calculated using Equation 3.1 is 1765 m/s assuming that $T_0 = 300$ K, i.e., room temperature. The ratio of the initial temperature, T_0 , to the final temperature, T_1 , can be written as [62]

$$\frac{T_1}{T_0} = \left(\frac{p_1}{p_0}\right)^{(\gamma - 1)/\gamma} \tag{3.2}$$

where p_0 and p_1 are the initial and final pressures of the gas and $\gamma = C_p/C_v$, which is equal to 5/3 for monoatomic gases and 7/5 for diatomic gases, with C_v the heat capacity at constant volume. This equation suggests that to get the largest temperature decrease, the pressure ratio must be large.

Experimentally, this can be achieved by expanding the gas into a vacuum (typical values of $<1x10^{-5}$ mbar) while increasing the reservoir pressure (typical values of 1 to 10 bar).

The expansion of a gas can be considered supersonic when the ratio of the average flow velocity at a distance z from the valve, $\bar{u}(z)$, to the local speed of sound of the gas, s(z), exceeds 1. This ratio defines what is known as the Mach number, M(z). During the expansion, the cooling decreases the local speed of sound of the expanding gas while the trandom motion of the constituent atoms or molecules is transferred into directed mass flow, which increases the average flow velocity [62].

The mach number can also be expressed as [63]

$$M(z) = A\left(\frac{L}{D} - B\right)^{\gamma - 1} - C\left(\frac{L}{D} - B\right)^{1 - \gamma}$$
(3.3)

where D is the diameter of the nozzle and the constants A=3.26, B=0.075 and C=0.61 for a monatomic gas, while A=3.65, B=0.4 and C=0.82 for a diatomic gas [63]. The average flow velocity of the supersonic beam can then be written in terms of the Mach number [64]

$$\bar{v} = M(z) \sqrt{\frac{\gamma k_B T(z)}{m}}, \tag{3.4}$$

which never exceeds v_{max} and has a velocity distribution given by [64]

$$f(\nu) = N\nu^2 e^{-\frac{(\nu - \bar{\nu})^2}{2k_B T(z)/m}}$$
 (3.5)

with *N* being a normalisation factor.

In a real supersonic expansion the collision frequency will drop to a level where vibrational, rotational or translational degrees of freedom will fall out of equilibrium. The gas becomes considered as free flowing, rather than being in a continuum flow. Consequently, the translational temperature, T(z), given by

$$T(z) = \frac{T_0}{1 + \frac{1}{2}(\gamma - 1)M(z)^2}$$
(3.6)

cannot decrease any further when the terminal Mach number, $M_t = 133P_0D^{(\gamma-1)/\gamma}$ (where P_0 and D are in units of atm and cm respectively), is reached [65].

In the experiments described here, a pulsed valve with D=0.5 mm was operated at a repetition rate of 50 Hz to reduce the pumping requirements needed to achieve low temperatures. The source pressure, $P_0 \simeq 5$ bar, and the gas expands into a vacuum with a typical pressure of $\simeq 1 \times 10^{-7}$ mbar. A skimmer placed ~ 40 mm downstream from the exit of the valve selects the densest and coldest central portion of the beam. With these parameters, the typical Mach number that can be reached at the position of the skimmer is $M \simeq 60$ and the beam reaches a terminal Mach number at $M_T \simeq 76$. The translational temperature of the metastable He atoms at the skimmer could be as low as $T \sim 0.25$ K, as given by Equation 3.6. The longitudinal velocity reaches 2000 ms⁻¹ at operating temperatures of ~ 350 K as determined by the flight time of the Rydberg atoms from the excitation position to the detection position. This temperature is higher than room temperature due to the valve heating up when operating.

3.2 Laser excitation

The scheme employed to excite one electron in He from the ground state to a Rydberg state is depicted in Figure 3.2. The energy needed to ionise one electron from the ground state is 24.587 eV [66] (λ = 50.432 nm), while

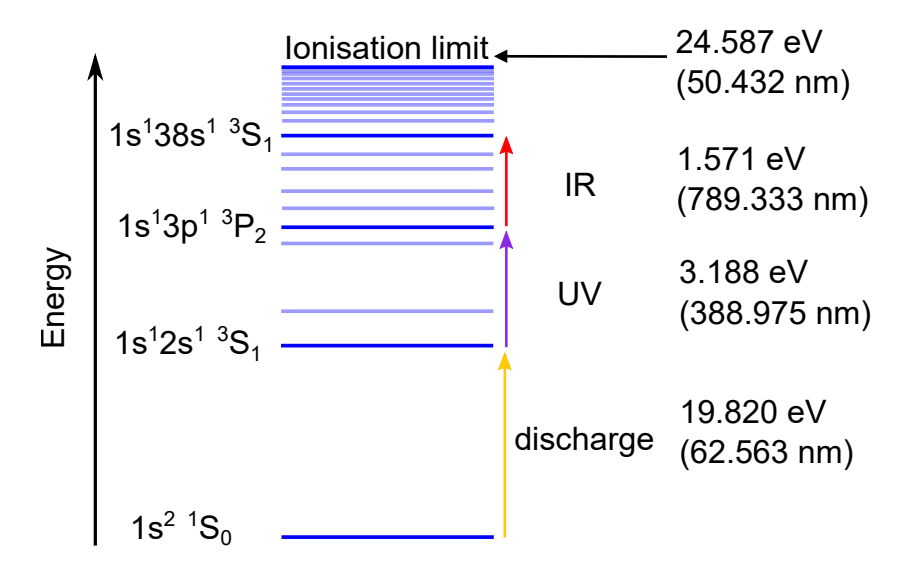


Figure 3.2: Schematic diagram of the two-photon excitation scheme used to prepare He Rydberg states (not to scale).

the electric discharge provides an energy of 19.820 eV and results in the formation of a metastable 1s2s 3S_1 level with a binding energy of 4.77 eV, and a lifetime of ~ 8000 s [67]. The metastable level allows for the Rydberg states to be accessible through the use of narrow-bandwidth tuneable lasers in the UV and visible region of the electromagnetic spectrum.

Continuous-wave diode lasers were utilised to generate the radiation for the resonance-enhanced two-photon excitation scheme shown in Figure 3.2. The UV laser (power: ~ 8 mW; focal spot beam waist: $\sim 100~\mu m$) was frequency stabilised to be resonant with the $1\text{s}2\text{s}^3\text{S}_1 \rightarrow 1\text{s}3\text{p}^3\text{P}_2$ transition at $25\,708.587\,6$ cm⁻¹ ($\equiv 388.975\,1$ nm). The lifetime of the $1\text{s}3\text{p}^3\text{P}_2$ level is ~ 100 ns [68], owing to the selection rules for electric dipole transitions that forbid a transition to the 1s^2 $^1\text{S}_0$ ground state. The IR laser (power: ~ 300 mW; focal spot beam waist: $\sim 100~\mu m$) was tuned to subsequently

drive $1s3p\ ^3P_2 \rightarrow 1sns/1snd$ transitions, where n=37-39. The laser radiation for both steps in this excitation process was linearly polarised (in the z-direction). Consequently, the strongest transitions are to the $|m_\ell|=0,1$ states. In the absence of external fields, 10^3-10^4 Rydberg atoms were prepared in each cycle of the experiment at number densities of $\sim 10^7 {\rm cm}^{-3}$. In the presence of an electric field, the number of Rydberg atoms prepared in each cycle is reduced to $\sim 10^2-10^3$. This is because in the presence of electric fields ℓ -mixing occurs, which reduces the s and d character of the Rydberg states so that there are no more pure transitions.

3.3 Detection

Approximately 12.5 μ s after the two-photon excitation scheme was implemented, a slowly rising, time-dependent, electric potential was applied to electrode E₂ in Figure 3.1. This potential ionised the Rydberg atoms, and the ejected electrons were accelerated through a small aperture in electrode E₁ onto a Micro-Channel Plate (MCP) detector. The MCP detector used in this experimental set up consists of two MCPs stacked in a chevron arrangement with densely distributed angled channels that are rotated 180° from each other. When an electron from an ionised Rydberg atom impinges on the wall of these micro channels, they act as electron multipliers leading to a cascade effect that amplifies the original signal by several orders of magnitude. The resulting electron current is then measured on an anode and converted to an electron signal in mV, allowing for direct detection of the Rydberg atoms.

The slowly rising, time-dependent, electric potential applied in the de-

tection region generated a time-dependent electric field, which allowed for state-selective detection of the Rydberg atoms. As discussed in Chapter 1.1.2, atoms in different Rydberg states ionise in different electric fields. This, in turn, means that electrons ionised from atoms in different Rydberg states will arrive at the detector at different times. Any other source of electron signal, i.e. from ionisation of any other species, would not contribute significantly to the electron signal measured. This is because of, firstly, the selective state nature of the detection method used, secondly, the fact that only a narrow range of ionisation fields is examined, and, thirdly, any background signal is subtracted from the collected data.

The detection region in the experimental setup was ~ 25 mm downstream from the laser-excitation region. Assuming the longitudinal speed of the Rydberg He atoms in the beam was 2000 m/s, it took the atoms $\simeq 12~\mu s$ to travel the distance from the laser-excitation region to the detection region. This flight time is smaller than the typical field-free radiative lifetimes of $\sim 40~\mu s$ of the low- ℓ triplet Rydberg states in He with values of n near 37. This lifetime has been previously calculated experimentally in our research group. Given this, the change to the radiative lifetimes of the Rydberg atoms caused by the time-dependent electric fields used in the experiments did not significantly effect the detected electron signal.

Chapter 4

Tunnel ionisation of high Rydberg states in strong electric fields

State-selective detection of Rydberg atoms in the experiments reviewed in Chapter 1.1 was, in general, achieved by ionisation in slowly-rising, pulsed, electric fields. For the collision studies involving Rydberg He and ground-state NH_3 discussed in Chapter 1.1.3, it was necessary to refine and optimise these detection schemes to allow new measurements at low temperature ($\sim 1 \, K$) and over the relative orientation of the collision partners. With this in mind detailed studies of electric field ionisation processes in Rydberg states of He were carried out. The results of these studies are presented in this chapter and, together with parts of the text, are based on Ref. [69] with adaptations to allow integration with the main themes of this thesis.

4.1 Introduction

Rydberg states of atoms and molecules represent ideal model systems with which to perform detailed studies of electric field ionisation, and develop schemes with which to manipulate and control ionisation processes [70]. Precise measurements of ionisation dynamics and electric-field ionisation rates of Rydberg states are of interest in the optimisation of schemes for quantum-state-selective detection [71]. These schemes are used in studies of collisions and interactions of Rydberg atoms and molecules in which state-changing occurs [12, 20], including, for example, the studies of resonant energy transfer in collisions of Rydberg atoms with polar ground state molecules [15, 16] discussed in Chapter 1.1 . The accurate characterisation of these ionisation processes is also of interest for studies of charge-transfer in Rydberg-atom and Rydberg-molecule—surface scattering [72, 73, 74].

In this chapter, experiments and calculations performed to study the ionisation dynamics and ionisation rates of triplet Rydberg states in helium with principal quantum numbers close to 37 in electric fields at the classical threshold of \sim 197 V/cm are described. The ionisation dynamics and ionisation fields of the states studied are of particular interest to the experimental studies of resonant-energy transfer in collisions of He Rydberg atoms with ground state NH $_3$ molecules discussed in Chapter 1.1.3.

4.2 Electric field ionisation of Rydberg atoms

4.2.1 Hydrogenic systems

In an electric field, $\vec{F} = (0, 0, F_z)$, the Hamiltonian for a hydrogenic atom with a single excited Rydberg electron, neglecting spin-orbit effects, can be expressed in atomic units as [75]

$$\hat{H} = \hat{H}_0 + \vec{f} \cdot \hat{\vec{r}} \tag{4.1}$$

$$=\hat{H}_0 + f_z \hat{z} \tag{4.2}$$

where \hat{H}_0 is the Hamiltonian in the absence of the field, $\hat{\vec{r}} = (\hat{x}, \hat{y}, \hat{z})$ is the position vector, and $\vec{f} = \vec{F}/F_0$, where $F_0 = 2hcR_M/ea_{0_M}$ with R_M and a_{0_M} the Rydberg constant and Bohr radius, respectively, corrected for the reduced mass of atom M, h is the Planck constant, c is the speed of light in vacuum, and e is the elementary charge. The introduction of the external electric field to the Coulomb field describing the interaction of the Rydberg electron with the ion core in the Rydberg atom results in the formation of a saddle point in the potential that is seen by the Rydberg electron [Figure 4.1]. Classically, a state that is found at an energy above the saddle point can spontaneously ionise.

Neglecting Stark energy shifts, the classical ionisation threshold, f_{class} , for a Rydberg atom is given by

$$f_{\rm class} = \frac{F}{16n^4} \tag{4.3}$$

where n is the principal quantum number. Considering the effect of the Stark shift, the ionisation threshold for high-field-seeking states, which

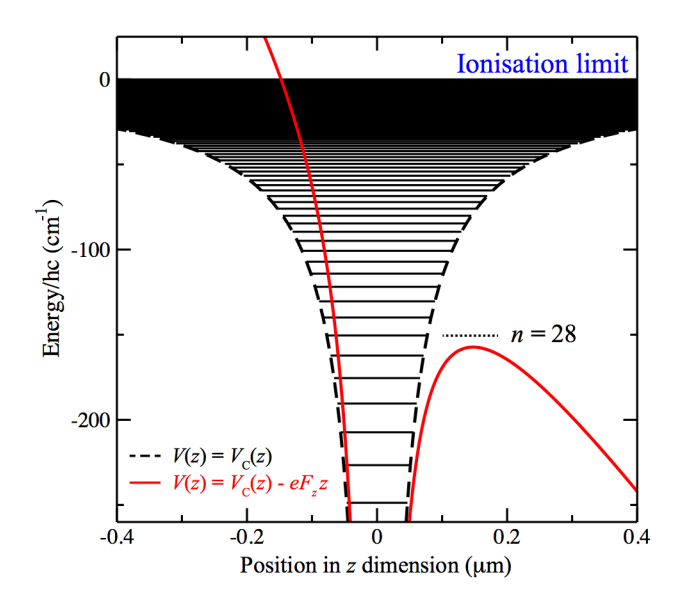


Figure 4.1: The Rydberg states of hydrogen in a pure Coulomb potential, $V_C(z)$, (dashed black curve) and the potential created when an electric field is introduced (red curve) resulting in a saddle point that opens to the continuum. From Ref. [76]

exhibit negative Stark energy shifts, is

$$f_{\rm class} = \frac{F}{9n^4} \tag{4.4}$$

while the ionisation threshold for low-field-seeking states, which exhibit positive Stark energy shifts, is typically twice that of the high-field-seeking states with the same n and for m=0. The difference in these thresholds arises because of differences in the orientation of the electric dipole moments. States that are high-field-seeking (low-field-seeking) possess static electric dipole moments oriented parallel (anti-parallel) to the field. Consequently, the corresponding electron charge density is located predominantly on the side of the ion core close to (far from) the saddle point.

As a result, in fields close to f_{class} states with negative Stark energy shifts readily ionise. On the other hand, in similar fields, states with positive Stark shifts have a lower probability of ionising and must be de-polarised by the field before ionisation occurs. This depolarisation occurs as a result of n-mixing.

Numerical methods can be used to calculate ionisation rates, however, it is convenient to first use a semi-empirical formula to obtain these. Damburg and Kolosov [75] derived an expression to calculate ionisation rates, Γ , using an asymptotic approach

$$\Gamma = \frac{(4R)^{2n_2+m+1}}{n^3n_2!(n_2+m)!} \exp\left[-\frac{2}{3}R - \frac{1}{4}n^3F\left(34n_2^2 + 34n_2m + 46n_2 + 7m^2 + 23m + \frac{53}{3}\right)\right] \tag{4.5}$$

where $R = (-2E_{\text{tot}})^{\frac{3}{2}}/F$ and the Stark Energy, E_{tot} , is calculated by performing a perturbation expansion up to $O(F^4)$. The ionisation rates calculated using Equation 4.5 do not differ by more than an order of magnitude from the rates obtained using numerical calculations for different sublevels of hydrogen, suggesting that Equation 4.5 can be used for any atomic state particularly in threshold field values of $10^7 \, \text{s}^{-1}$.

4.2.2 Non-hydrogenic atoms and molecules

The energy-level structure of Rydberg states in non-hydrogenic atoms such as helium can be calculated numerically by determining the eigenvalues of the Hamiltonian matrix, \hat{H} , in Equation 4.1, for a range of electric fields of interest. In doing this in the $|n\ell m\rangle$ basis, the diagonal matrix elements associated with \hat{H}_0 are obtained from the Rydberg formula as given in

CHAPTER 4. TUNNEL IONISATION OF HIGH RYDBERG STATES IN STRONG ELECTRIC FIELDS

$\overline{\ell}$	$\delta_{36\ell}$	$\delta_{37\ell}$
0	0.296 687	0.296 685
1	0.068346	0.068 347
2	0.002886	0.002887
3	0.000446	0.000446
4	0.000 127	0.000 127

Table 4.1: Quantum defects of n = 36 and 37 triplet Rydberg states in helium [77].

Equation 2.1 with quantum defects for the low- ℓ states in helium obtained from Ref. [77]. The values of these quantum defects for triplet states with n = 36 and 37 are listed in Table 4.1.

The radial integrals required in the calculation of the off-diagonal matrix elements associated with the electric field term in Equation 4.1 were determined using the Numerov method. This was implemented as described in Chapter 2.2 and Ref. [56] with logarithmic rescaling of the spatial coordinate, an integration stepsize of 0.005, and a pure 1/r potential. The corresponding angular integrals were determined using standard angular momentum algebra.

An example of a Stark map calculated using this approach for values of n close to 37, azimuthal quantum numbers |m| = 0 and 1, and fields up to 220 V/cm is displayed in Figure 4.2. To achieve convergence of the calculated energy-level structure to ~ 0.001 cm⁻¹ in the highest fields in this figure, a basis of states containing values of n from 28 to 55, and all corresponding values of ℓ was required. In this figure the energy associated with the

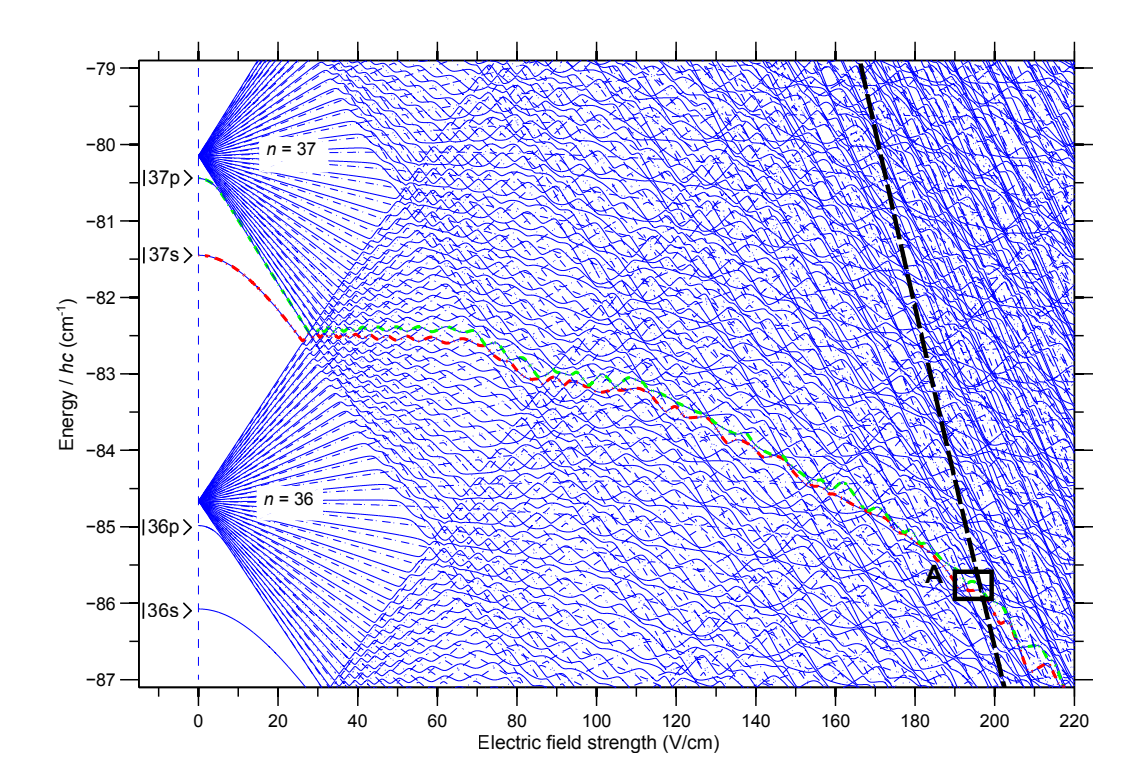


Figure 4.2: Calculated Stark map of triplet Rydberg states in helium in the vicinity of the field-free n=36 and n=37 states. Sub-levels for which m=0 (|m|=1) are indicated by the continuous (dash-dotted) curves. The classical ionisation threshold is denoted by the long-dashed black curve between 166 and 202 V/cm. The states that evolve adiabatically from the $|37s\rangle$ and $|37p\rangle$ field-free Rydberg states as the field is increased are indicated by the red and green thick dash-dotted curves, respectively. The region enclosed by the rectangle labeled A is discussed in the text.

saddle point in the potential experienced by the Rydberg electron in the presence of the field, i.e., the Stark saddle point, is indicated by the thick dashed curve between 166 and 202 V/cm.

For hydrogenic Rydberg states tunnel ionisation rates in strong electric fields can be calculated using the semi-empirical methods described above in Section 4.2.1. To treat these electric field ionisation processes for non-hydrogenic states, such as the low-|m| Rydberg states in helium that are of interest here, numerical methods must be employed. This can be achieved in a manner that is compatible with the matrix methods used in the calculation of the energy-level structure in Figure. 4.2 by the introduction of complex absorbing potentials (CAP) to the expression in Equation 4.1. This approach, and the methods implemented here, are based on the recent work in Ref. [78] in which ionisation processes in Rydberg states of rubidium were studied experimentally and theoretically.

As in Ref. [78], to numerically calculate the eigenstate tunnel ionisation rates, the total Hamiltonian for the system including the CAP is expressed as

$$\hat{H}_{\text{CAP}} = \hat{H} - i\eta W, \tag{4.6}$$

where η is a scaling parameter that is unique to each eigenstate in each electric field of interest, and W is the function chosen to act as the absorbing potential. In the experiments reported here, Rydberg state tunnel ionisation rates within $\sim 1~{\rm cm}^{-1}$ of the Stark saddle point, and hence the classical ionisation threshold, have been studied. Over this energy range the experimental data have been compared with the results of calculations performed using two different CAPs. Both of these potentials scale with

 r^6 . In the first [79]

$$W(r) = r^6, (4.7)$$

while in the second [78]

$$W(r, f) = \Theta[r - r_{c}(f)][r - r_{c}(f)]^{6}, \tag{4.8}$$

where $\Theta[r - r_c(f)]$ is a Heaviside function, and $r_c(f) = f^{-1/2}$ is the radial position associated with the Stark saddle point in the field f and is used to place the onset of r^6 in the potential $W(r, F_E)$ as depicted in Figure 4.3. The role of the absorbing potential is to define the inside and outside region of the atom so that only the parts of the wavefunction that extend outside the atom are absorbed. The form of the CAP in Equation 4.7 has previously been used in the calculation of ionisation rates of low-n states in hydrogen and lithium in strong electric fields [79]. The function in Equation 4.8 corresponds to that employed in recent studies of Rydberg states in rubidium [78]. This second form of the CAP is a well defined function of the applied field and offers, in part, the possibility of removing the dependence of η on the field strength. Because of the spherical symmetry of Equations 4.7 and 4.8, only the diagonal matrix elements associated with these CAPs, in the $|n\ell m\rangle$ basis in which the calculations were performed, were considered. The radial integrals required in the construction of these matrices were calculated using the Numerov method.

The complex eigenvalues

$$\lambda_j = E_j - i \frac{\Gamma_j}{2} \tag{4.9}$$

of the Hamiltonian in Equation 4.6, which includes the CAP, yield the eigenenergy E_j and Γ_j is the resonance width, which corresponds to the

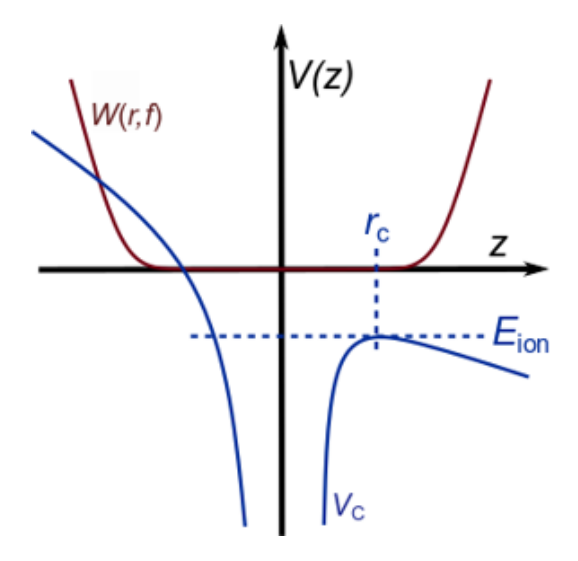


Figure 4.3: A graphical depiction of the complex absorbing potential, W(r, f), and the potential experienced by the Rydberg electron, V_C . The radial position of the saddle point, r_C marks the onset of r^6 in the potential given by Equation 4.8 and E_{ion} is the classical ionisation threshold.

ionisation rate of each eigenstate. The parameter η in Equation 4.6 can be obtained by comparison of E_j with the energy of the corresponding eigenstate obtained from Equation 4.1 in the absence of the CAP, or by comparison of E_j and Γ_j with experimental data. The values of the ionisation rates, Γ_j , are more sensitive to changes in η than the values of E_j .

4.3 Experiment

The general experimental setup used in the work presented in this chapter has been described in Chapter 3. The timing sequence for the excitation to the Rydberg states and the subsequent ionisation of the Rydberg atoms is shown in Figure. 4.4. Excitation of the atoms to Rydberg states with

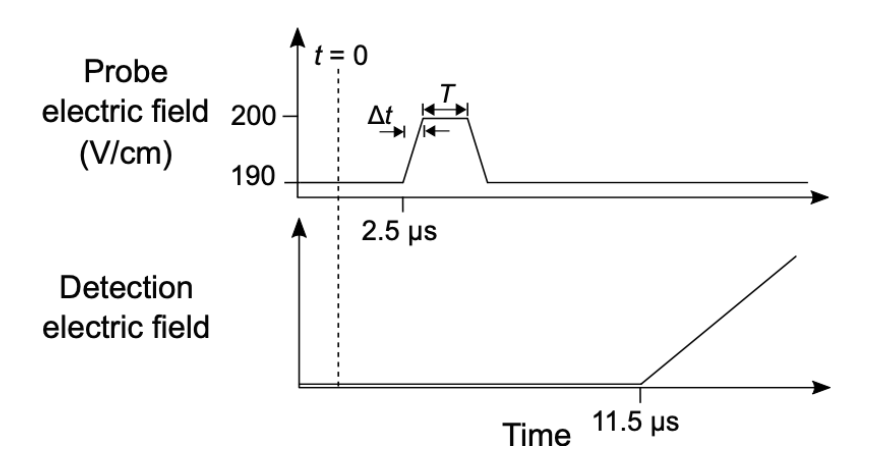


Figure 4.4: Timing sequence indicating the excitation (time t = 0), electric field switching, and detection steps of the experiments.

values of n close to 37 took place at t=0 between the two parallel copper electrodes [see Figure 3.1 in Chapter 3]. The excitation scheme was implemented in the presence of a strong electric field (190-200 V/cm) generated by applying a high negative potential to electrode E_2 . However, while the experiments were performed at these high electric fields, the states were firstly followed from 0 V/cm up to the area of interest at regular field intervals to ensure the correct states are being observed. In these fields $\sim 10^2-10^3$ atoms were excited in each cycle. The laser radiation for both steps in this two-photon excitation scheme was linearly polarised parallel to this field. Consequently, the strong transitions in the spectra recorded were to states for which |m|=0 and 1. 2.5 μ s after photoexcitation, the electric field was switched for a short period of time, T, by applying a pulsed potential of between -10 and +10 V to electrode E_1 as indicated in Figure 4.4. This permitted the measurement of electric-field-dependent changes in the Rydberg state ionisation rates. Two different power sup-

plies were used to apply the strong electric fields and weak electric fields in order to gain better control on the chosen electric fields. This implementation lead to field drifts of less than 0.01 V/cm. After the potential on electrode E_1 returned to its initial value, a slowly rising potential was subsequently applied at $t=11.5~\mu s$ to electrode E_2 to ionise the surviving bound Rydberg atoms. The electrons resulting from this ionisation step were accelerated to a microchannel plate (MCP) detector and collected for detection. In all of the measurements described here, the electron signal associated with the surviving Rydberg atoms was integrated and recorded to represent the number of detected atoms.

4.4 Results

The experiments described in this chapter were performed in the region of the Stark map in Figure 4.2 between electric fields of 190 and 200 V/cm, and wavenumbers of -86 to -85 cm⁻¹. This part of the Stark map lies within 1 cm⁻¹, or 10 V/cm, of the classical adiabatic ionisation thresholds of the $|37s'\rangle$ and $|37p'\rangle$ ℓ -mixed eigenstates, which evolve adiabatically from the $|37s\rangle$ and $|37p\rangle$ Rydberg states in zero electric field, and is enclosed by the dashed rectangle labeled A in Figure 4.2.

An expanded view of this energetic region is displayed in Figure 4.5. In this figure the continuous and dashed-dotted curves correspond to the calculated energies of m = 0 and |m| = 1 sub-levels, respectively. The energy associated with the Stark saddle point, i.e., the classical ionisation field, is indicated by the thick dashed black curve between 195.9 and 196.8 V/cm. To validate the results of the calculations, laser photoexcitation spectra of

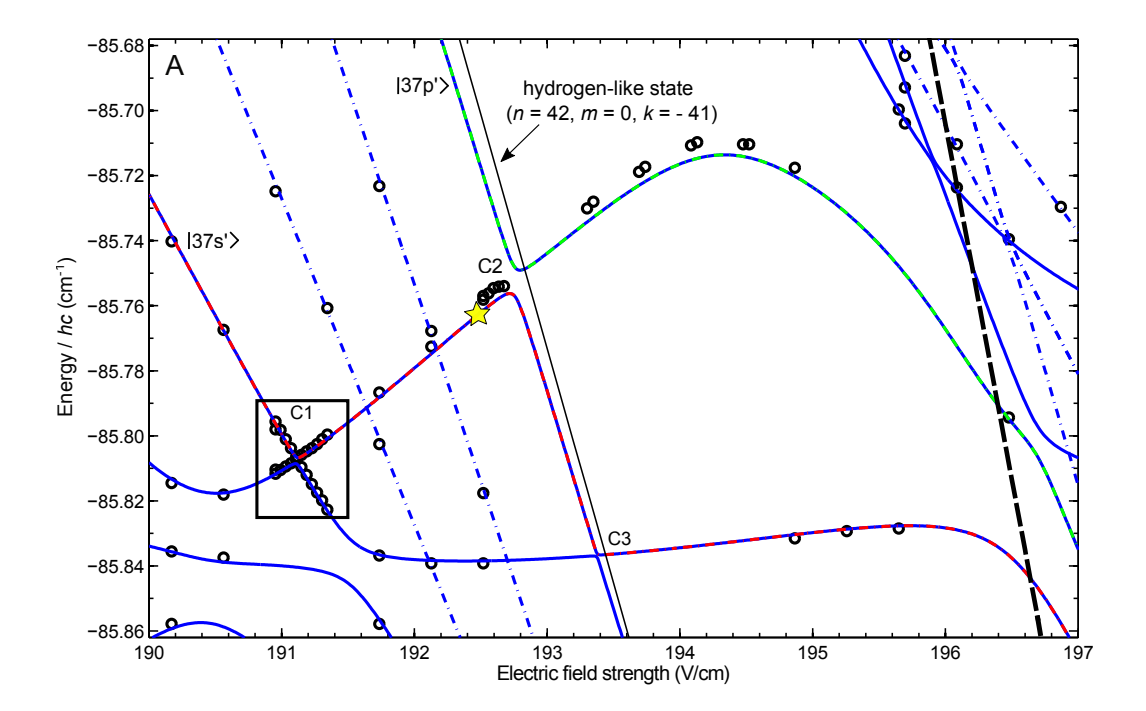


Figure 4.5: The region of the Stark map enclosed in the solid rectangle labeled A in Figure 4.2. The calculated energy-level structure (thick continuous and dash-dotted curves) is compared to the positions of resonances in the measured laser spectra (open circles). The positions in the Stark map at which the $|37s'\rangle$ state was excited for the ionisation rate measurements is marked by the yellow star. The thin continuous curve labeled n = 42, m = 0, k = -41 represents to the hydrogen-like state discussed in the text.

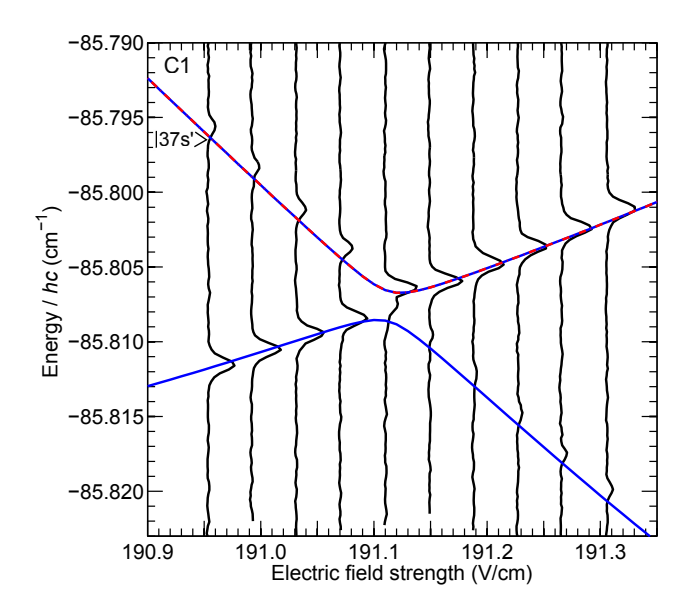


Figure 4.6: Laser photoexcitation spectra (vertical curves) of triplet Rydberg states in helium overlaid with the calculated energy-level structure in the region of the avoided crossing labeled C1 in Figure 4.5. The amplitude of the spectral features corresponds to the integrated electron signal.

transitions to the eigenstates within the range of electric fields and energies encompassed in Figure 4.5 were recorded. An example of such spectra, in the region surrounding the avoided level crossing labeled C1, are displayed in Figure 4.6.

In Figure 4.6 the observed spectral intensities arise from the combination of the relative transition strengths from the intermediate $1s3p\ ^3P_2$ level in each field, and excited state decay by tunnel ionisation. The experimental spectra are compared with the calculated eigenenergies of the two states at the crossing, where the upper curve in Figure 4.6 represents the $\left|37s'\right\rangle$ state. There is very good quantitative agreement between the measured and calculated energy-level structure in these fields. Repeated

measurements in this and other similar fields indicate that the deviation between the results of the experiments and calculations are dominated by slow fluctuations of $\sim \pm 10$ mV/cm (or $\pm 0.05\%$) in the magnitude of the applied electric fields. The spectral widths of the measured transitions are limited by the interaction time of the atomic beam with the focused laser beams and are ~ 0.001 cm⁻¹ [60]. To obtain a broader perspective on the agreement between the experimental data and the results of the calculations, the wavenumbers associated with the intensity maxima of each spectral feature in Figure 4.6 were determined and overlaid, together with the results of similar measurements in a range of other electric fields, on the calculated energy-level diagram in Figure 4.5. Each open circle in this figure represents an observed transition to a Rydberg state with a sufficient lifetime ($\gtrsim 1~\mu s$) to permit detection.

Rydberg state ionisation dynamics, over the range of electric fields and energies encompassed in Figure 4.5, were studied by photoexcitation of each state of interest in a field in which its tunnel ionisation rate was slow compared with the timescale of the experiment. The electric field was then switched to a higher or lower value to probe the field-dependence and timedependence of the ionisation dynamics. The first set of experiments were performed to study the threshold ionisation fields and ionisation rates of the $|37s'\rangle$ state. In these measurements, the atoms were first excited to the $|37s'\rangle$ state in a field of 192.5 V/cm (yellow star in Figure 4.5) up to which the tunnel ionisation rate is $< 10^5 \text{ s}^{-1}$. After photoexcitation the electric field in the apparatus was switched, in a time Δt , to a range of different values for $T = 4 \mu s$ [see Figure 4.4(b)]. After this, the field was switched

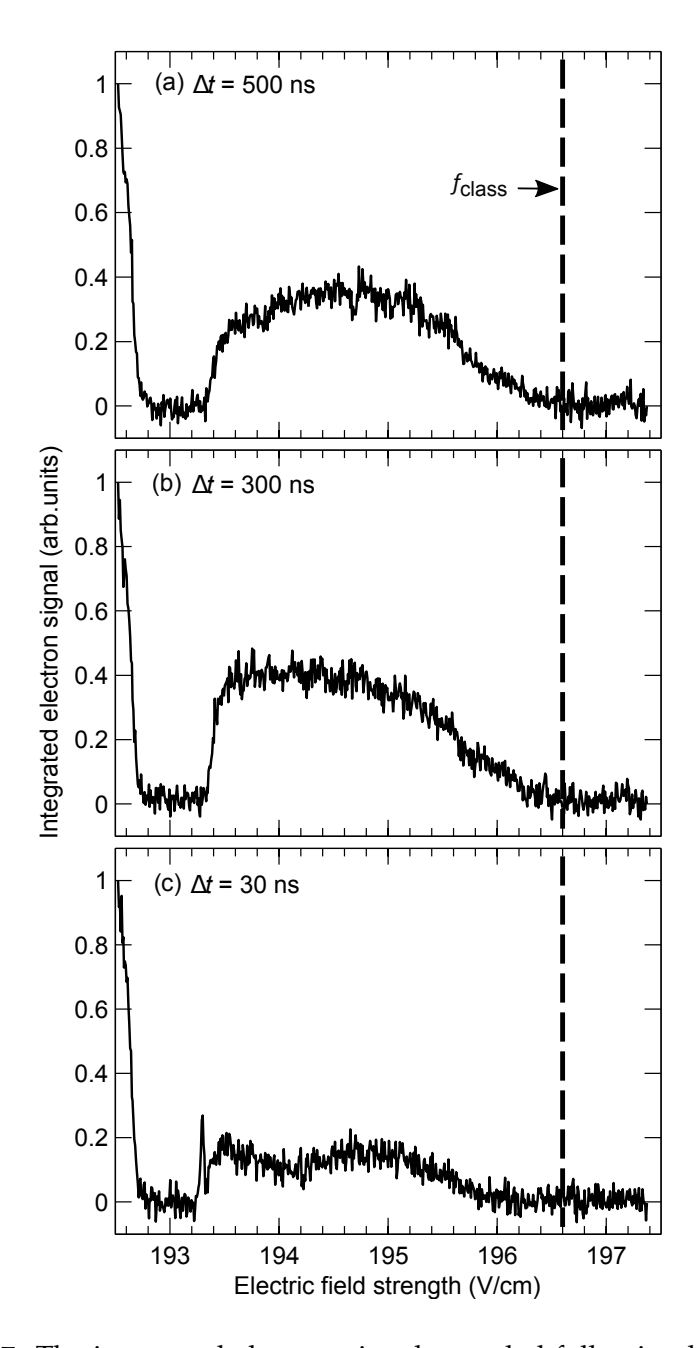


Figure 4.7: The integrated electron signal recorded following laser photoexcitation of the triplet $|37s'\rangle$ state in helium, as a function of electric field strength for the three different field-switching times, Δt , as indicated.

back to its initial value and the fraction of surviving bound Rydberg atoms was determined. This procedure, performed for switching times $\Delta t = 500$, 300 and 30 ns, resulted in the data presented in Figure 4.7 and yielded insights into the ionisation dynamics of the $|37s'\rangle$ state in this range of electric fields.

As can be seen in Figure 4.5, the $|37s'\rangle$ state crosses the classical ionisation threshold at a field of ~ 196.6 V/cm. However, the data in Figure 4.7 show that significant decay by ionisation occurs in fields up to ~ 4 V/cm below this threshold. When the field is switched slowly [$\Delta t = 500$ ns, Figure 4.7(a)] from its initial value of 192.5 V/cm to values up to 197.4 V/cm, significant signal loss is seen in fields between 192.8 and 193.3 V/cm. Over this range of fields the $|37s'\rangle$ state evolves adiabatically through the avoided crossing C2 (see Figure 4.5) from being a low-field-seeking state, with a positive Stark shift, and hence with electron density predominantly located on the side of the He⁺ ion core opposite to that of the Stark-saddle point, to high-field-seeking with a negative Stark shift. In this case, the electron charge density is transferred to the side of the He⁺ ion core close to the Stark saddle point, resulting in a higher propensity to tunnel ionise. Since in this range of fields almost all of the atoms are lost by ionisation within the duration of the 4- μ s-long electric field pulse, the tunnel ionisation rate must be in excess of $\sim 2.5 \times 10^5 \ s^{-1}$. For fields higher than 193.3 V/cm the |37s' \rangle state passes through the avoided crossing C3 in Figure 4.5. The linear Landau-Zener model [80, 81] indicates that when $\Delta t = 500$ ns (dF/dt ~ 2 $V/cm/\mu s$) the probability of adiabatic traversal of this avoided crossing is \sim 1. This is consistent with the increase in signal in Figure 4.7(a) for fields between 193.4 and 196 V/cm that occurs because the $|37s'\rangle$ state switches from being strongly high-field-seeking to having approximately zero static electric dipole moment. Therefore, there is an almost equal distribution of electron charge on both sides of the He⁺ ion core, close to and far from the Stark saddle point. This results in a reduced propensity to tunnel ionise. Finally, as the field approaches the classical ionisation field of 196.6 V/cm the loss of excited atoms increases. This increase arises in part because of the depression of the Stark saddle point in these fields, and in part because the $|37s'\rangle$ state becomes slightly more polarised, and high-field-seeking, in fields above 196 V/cm (see Figure 4.5).

A comparable set of measurements carried out for $\Delta t = 300$ ns [Figure 4.7(b)] yielded similar results. The only notable difference between these two sets of data is the slightly larger fraction of surviving Rydberg atoms in fields between 193.4 and 194.8 V/cm when $\Delta t = 300$ ns. This is a result of switching more quickly through the region between 192.8 and 193.2 V/cm in which rapid tunnel ionisation occurs. Therefore, the ionisation dynamics in Figure 4.7(a) and Figure 4.7(b) must be considered similar, with a similar evolution through the avoided crossings C2 and C3. However, if Δt is further reduced to 30 ns (dF/d $t \sim 30$ V/cm/ μ s) the surviving Rydberg atom fraction in fields beyond 193.2 V/cm is quite different [see Figure 4.7(c)]. In this case, the avoided crossing C2 is traversed adiabatically, while the Landau-Zener probability of adiabatic traversal of crossing C3 reduces to \sim 0.6. After passing through the crossing C3, the excited atoms evolve into a superposition of the two interacting states with their significantly different Stark energy shifts and hence tunnel ion-

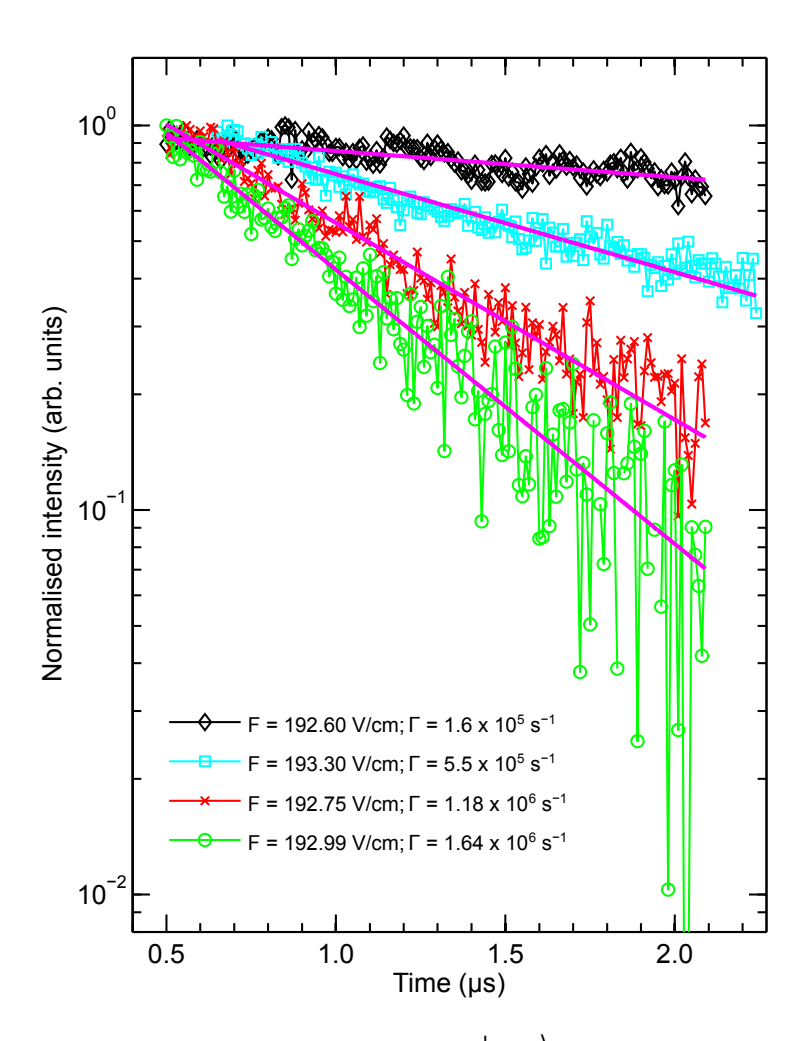


Figure 4.8: Tunnel ionisation of the triplet $|37s'\rangle$ state in helium recorded in the electric fields indicated. Fitted exponential functions (straight lines) yielded the ionisation rates listed. The uncertainties are on the scale of the variation in the data points, these are mostly dominated by the fluctuations in the signal. The data points are connected by lines for clarity.

isation rates. The time-evolution of this superposition contributes to the oscillatory behaviour of the surviving fraction of Rydberg atoms in fields between 193.2 and 196 V/cm.

In experiments in which ramped electric field ionisation of the $|37s'\rangle$ state is implemented beginning in fields close to zero, the electric field switching rates are typically on the order of 200 V/cm/ μ s [15]. Consequently, under such conditions the turning point at the avoided crossing C2 at 192.8 V/cm may be considered the threshold adiabatic ionisation field of the $|37s'\rangle$ state.

More detailed information can be obtained on the tunnel ionisation rates of the states in Figure 4.5 by direct measurements in the time domain. To perform these for the $|37s'\rangle$ state, laser photoexcitation was again carried out at the same position in the Stark map as when recording the data in Figure 4.7 (yellow star in Figure 4.5). However, after this was completed, the probe electric field pulse ($\Delta t = 300 \text{ ns}$) was applied for period of time, T, that was adjusted in the range from 500 ns to 2 μ s, The field was then switched back to its initial value of 192.5 V/cm before the surviving fraction of excited atoms was detected by pulsed electric field ionisation. The dependence of the integrated electron signal on the probe pulse duration was then recorded for a range of probe fields, with the corresponding loss rate of excited atoms reflecting the tunnel ionisation rate in each field. Examples of this data, recorded for pulsed electric fields with amplitudes of 192.60, 192.75, 192.99, and 193.30 V/cm, are displayed in Figure 4.8. The measured loss rates in each case can be described by a single exponential function. For the range of fields studied, the time constants of these functions range from 600 ns to 6.25 μ s.

A complete set of measured tunnel ionisation rates of the $|37s'\rangle$ state, determined from data recorded in pulse electric fields between 192.6 and 196.59 V/cm, are presented in Figure 4.9. To allow direct comparison with the corresponding energies of the $|37s'\rangle$ state a portion of the Stark map in Figure 4.5, containing only the states for which m=0, is included in Figure 4.9(a). The positions at which the ionisation rates were measured are shown as open circles in this Stark map, with the corresponding ionisation rates also indicated as open circles in Figure 4.9(b).

As can be seen from Figure 4.9(a) and the experimental data in Figure 4.9(b), in fields between 192.6 and 192.8 V/cm the $|37s'\rangle$ state is low-field-seeking and its tunnel ionisation, measured to occur at a rate between 1.6 x 10^5 and $5.3 \times 10^5 \text{ s}^{-1}$, is suppressed because the electron charge is located predominantly on the side of the He⁺ ion core opposite to the Stark saddle point. When it becomes high-field-seeking, in fields between 192.8 and 193.3 V/cm, the tunnel ionisation rate immediately increases to $> 10^6 \text{ s}^{-1}$. This change is a result of the electron charge being transferred to the side of the He⁺ ion core close to the Stark saddle point, and occurs despite the fact that in this range of fields the $|37s'\rangle$ state is more deeply bound than in the lower fields of 192.6 to 192.8 V/cm.

The experimental data in Figure 4.9(b) have been compared to the results of calculations of the corresponding tunnel ionisation rates performed using the CAP methods described in Section 4.2.2. The results of the calculations in which the electric-field-dependent form of the CAP in Equation 4.8 was used are indicated by the dashed and dash-dotted

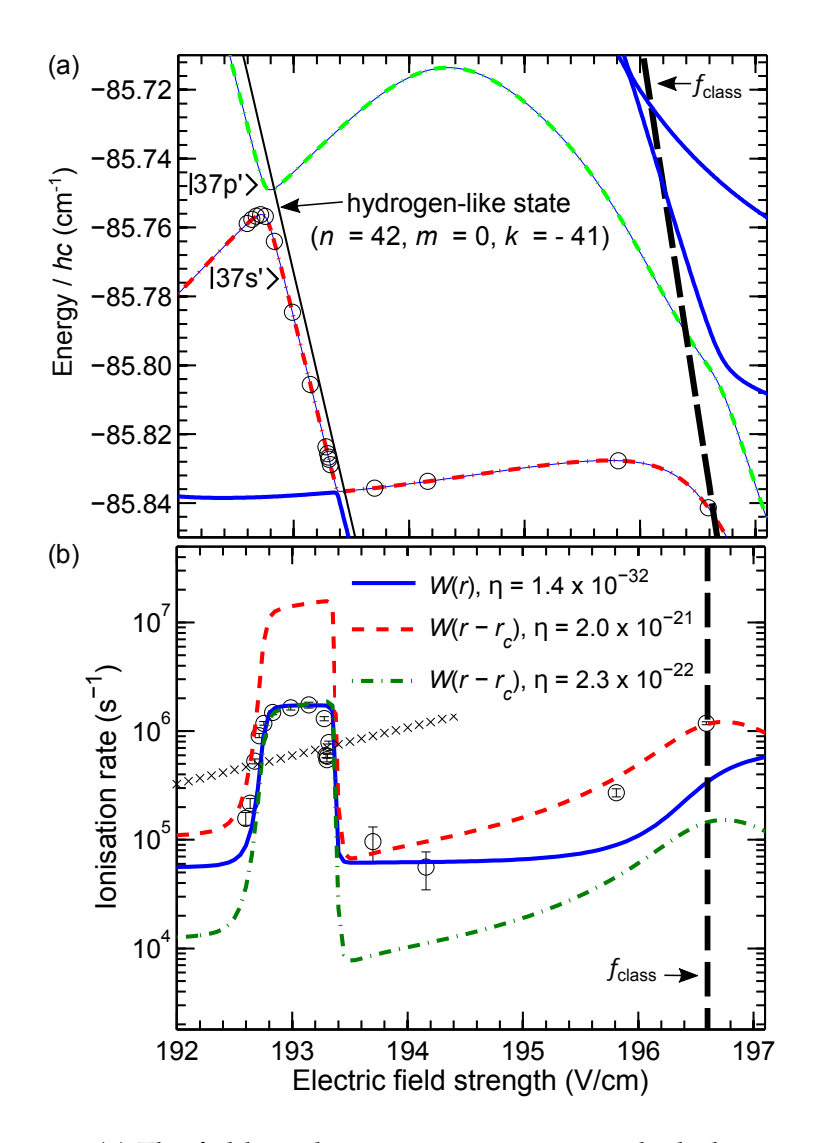


Figure 4.9: (a) The fields and energetic positions at which the ionisation rates of the $|37s'\rangle$ state were measured (open circles). (b) The corresponding ionisation rates (open circles) together with the results of the calculations. Ionisation rates calculated using the field-independent CAP are shown as the continuous blue curve in (b), while those calculated with the field-dependent CAP are represented by the dashed and dashed-dotted curves for the two different values of η listed.

curves. The use of the field-independent CAP in Equation 4.7 yielded the results indicated by the continuous curve. In using both of these CAPs, the value of the scaling factor η was obtained, in atomic units, by fitting the calculated results to the experimental data.

For the electric-field-dependent CAP, the value of η was first fitted to the measured ionisation rates in excess of $10^6~\rm s^{-1}$ in fields between 192.7 and 193.2 V/cm. This resulted in a value of $\eta = 2.3 \times 10^{-22}$ and the data indicated by the dash-dotted curve in Figure 4.9(b). The results of the calculations are in good quantitative agreement with the experimental data over the range of fields in which high ionisation rates were measured, i.e., when the $\left|37s'\right\rangle$ is high-field-seeking. But when the static electric dipole moment of the $\left|37s'\right\rangle$ state reduces towards zero, in fields above 193.5 V/cm, the calculated rates are approximately an order of magnitude lower than those measured in the experiments. With the measured ionisation rates extending over almost two orders of magnitude in the range of fields in Figure 4.9(b) the results of the calculations do however follow the same general trend as the field strength increases.

In fields above 193.5 V/cm, where the results obtained with $\eta = 2.3 \times 10^{-22}$ deviate most significantly from the experimental data, it was found that calculations in which $\eta = 2.0 \times 10^{-21}$ [dashed curve in Figure 4.9(b)] yielded closer agreement with the experimental data. However, in this case the calculated rates deviate from the experimental data by a factor of approximately 10 in the low-field region between 192.7 and 193.2 V/cm. These observations indicate that using the electric-field-dependent form of the CAP in Equation 4.8 is not sufficient to completely account for effects of

the sign of the static electric dipole moments, and hence Stark shifts, of the states, on the tunnel ionisation rates below the classical ionisation threshold. In these instances it would seem that it may be necessary to combine the electric-field-dependent form of W(r, f) with a dependence of η on the static electric dipole moment, or the derivative of the energy with respect to the field strength, of the states of interest to obtain more reliable results over a wider range of fields.

Further comparison of the experimental data in Figure 4.9(b) with the results of calculations performed with the electric-field-independent CAP in Equation 4.7 was also carried out. In this case the most appropriate value of η to fit the results of the calculations to the experimental data in the low-field region between 192.7 and 193.8 V/cm was $\eta = 1.4 \times 10^{-32}$ [continuous blue curve in Figure 4.9(b)]. This value of η gives good quantitative agreement with the experimental data over a wider range of fields than the calculated results obtained using the field-dependent CAP. Significant deviations are only seen when the energy of the $|37s'\rangle$ state approaches the classical ionisation threshold.

Finally, the ionisation rates measured for the $|37s'\rangle$ state can be compared with the tunnel ionisation rates for hydrogenic Rydberg states calculated using the semi-empirical approach in Ref. [75]. The hydrogen-like state with n = 44, m = 0, $k = n_1 - n_2 = -41$, where n_1 and n_2 are the parabolic quantum numbers [thin black line between 192.4 and 193.6 V/cm in Figure 4.5 and Figure 4.9(a)] lies within ~ 0.01 cm⁻¹ of the energy of the $|37s'\rangle$ state in fields between 192.3 and 193.8 V/cm. These are the fields that correspond to the highest measured ionisation rates in Figure 4.9(b). The

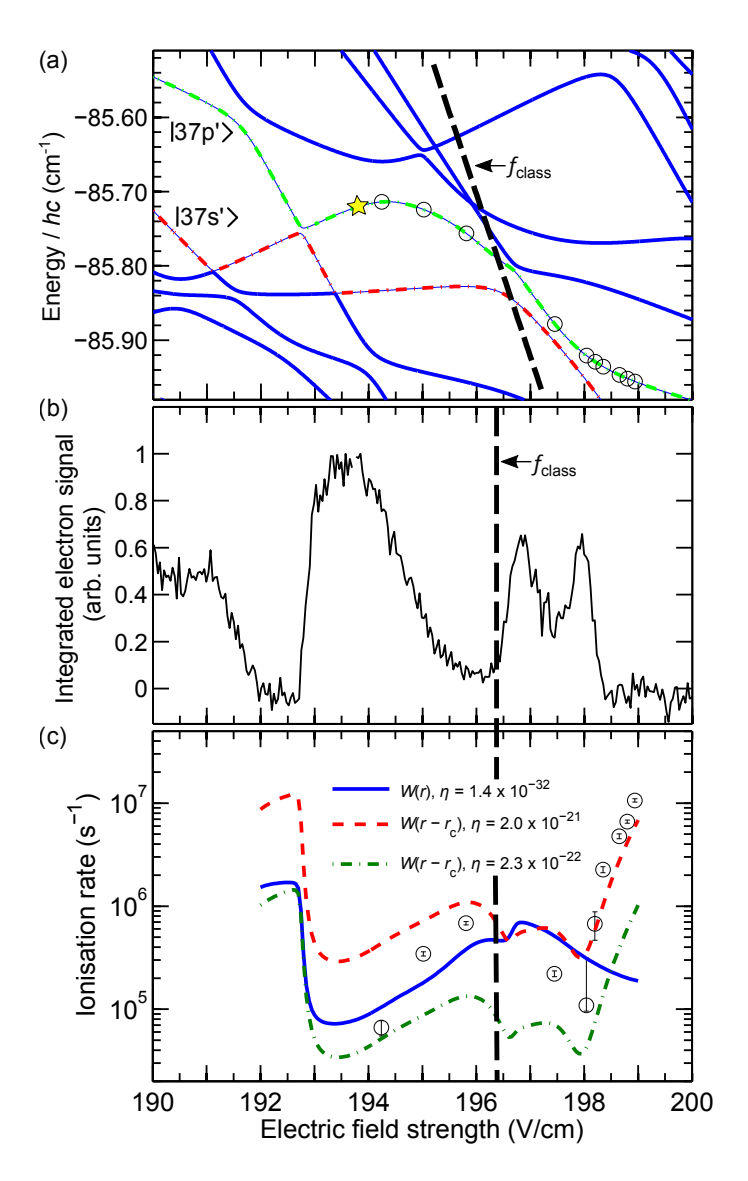


Figure 4.10: (a) The fields at which the ionisation rates of the $|37p'\rangle$ state were measured (open circles) and the initial photoexcitation field (yellow star). (b) The integrated electron signal of the $|37p'\rangle$ state for $T=4~\mu s$ and $\Delta t=300~ns$. (c) Measured (open circles) and calculated tunnel ionisation rates. The ionisation rates calculated using the field-independent CAP are indicated by the continuous blue curve in (c), while those calculated with the field-dependent CAP are represented by the dashed and dashed-dotted curves for the two different values of η indicated.

calculated ionisation rates for this hydrogen-like state are indicated by the crosses in Figure 4.9(b). The semi-empirical calculations for this hydrogen-like state yield tunnel ionisation rates that are a factor of 5 lower than those measured for the $|37s'\rangle$ state. This observation gives an indication of the accuracy of this semi-empirical method widely used in the calculation of tunnel ionisation rates of hydrogenic Rydberg states [82], and is of a similar scale to the expected deviations from the exact rates discussed in Ref. [75]. Indeed, because the $|37s'\rangle$ state is more tightly bound than the associated hydrogen-like state, it is likely that the semi-empirical approach underestimates the true ionisation rates by more than the observed factor of 5.

The procedure outlined above to measure the ionisation rates of the $|37s'\rangle$ state was also applied to determine the tunnel ionisation rates of the $|37p'\rangle$ state. The position in the Stark map at which this state was initially laser photoexcited in these experiments is indicated by the yellow star in Figure 4.10(a) and the fields in which ionisation rates were measured are shown as open circles. An overview of the field-dependence of the tunnel ionisation of the $|37p'\rangle$ state was first obtained by subjecting the excited atoms to a range of pulsed electric fields for $T=4~\mu s$ with $\Delta t=300~ns$. The results of these measurements, which indicate the fraction of atoms surviving in bound states following this process are displayed in Figure 4.10(b). These data indicate two regions of significant tunnel ionisation below the classical ionisation field: 192.0 to 192.8 V/cm and 195.8 to 196.2 V/cm. As in the case of the $|37s'\rangle$ state, these are regions in which the $|37p'\rangle$ state exhibits pronounced high-field-seeking character. The ionisation rates measured

at the fields indicated in Figure 4.10(a) are shown as open circles in Figure 4.10(c), together with the rates calculated using the field-independent (continuous curve) and field-dependent (dashed and dash-dotted curves) CAPs. The values of η in these CAPs are the same as those used in the calculations for the ionisation rates of the $|37s'\rangle$ state. Below the classical ionisation field the results obtained using the field-independent CAP are in good agreement with the experimental data. In fields above $f_{\rm class}$ the field-dependent CAP with $\eta = 2.0 \times 19^{-21}$ provides the closest agreement with the experimental data. But, as in the case of the $|37s'\rangle$ state, no one CAP completely describes the ionisation dynamics over the full range of fields in Figure 4.10. These observations for the $|37p'\rangle$ state lead to the same conclusion as that reached for the $|37s'\rangle$ state from the data in Figure 4.9(b): In order to calculate ionisation rates that accurately reflect the measured values, a field-dependent CAP with an additional dependence on the static electric dipole moment of the states of interest is needed.

It is evident from the data in Figure 4.10 that the measured electron signal of the $|37p'\rangle$ state is dependent on whether it is high-field-seeking or low-field seeking. Comparing the data in Figure 4.10(b) with the ionisation rates calculated using the field-dependent CAPs in Figure 4.10(c) indicates that when the measured electron signal is low, i.e., the lifetime of the Rydberg atoms is not long enough to permit detection, the corresponding calculated ionisation rate is higher than the ionisation rate in a field where the electron signal is high. In general, the tunnel ionisation rates calculated using the field-dependent CAPs match each corresponding structure in Figure 4.10(b). For example, the two intensity maxima in Figure 4.10(b),

in fields between 196.4 and 198.4 V/cm correspond to two dips in the ionisation rate in Figure 4.10(c) in the same range of fields. It can also be seen in Figure 4.10(b) that there remain structures observed beyond the classical ionisation threshold at 196.4 V/cm for the $|37p'\rangle$ state. However, in fields from 198 to 208 V/cm the electron signal does not rise above zero, suggesting that this state always ionises rapidly in fields higher than the classical ionisation field. Indeed, at 199 V/cm the measured ionisation rate is on the order of 10^7 s⁻¹ and for fields slightly lower than this the signal in Figure 4.10(b) is already zero.

4.5 Conclusions

Through the experimental and theoretical work described in this chapter the ionisation dynamics and tunnel ionisation rates of triplet Rydberg states in helium have been studied in fields within 1 cm $^{-1}$, or 10 V/cm, of the classical adiabatic ionisation thresholds of the $|37s'\rangle$ and $|37p'\rangle$ ℓ -mixed eigenstates. The experimental data, including direct measurements of tunnelling rates in the time domain, have been compared to the results of calculations performed using two types of complex absorbing potential. The calculated energy-level structure is in excellent quantitative agreement with the experimental data over the full range of fields and eigenstates studied. The calculated tunnel ionisation rates follow the same general trends as those seen in the experiments. However, the precision of the time-domain measurements, which encompass almost two orders of magnitude in tunnelling rate, highlights deficiencies in these methods of calculation. They also exceed the limit of the applicability of tunnel ionisation rate

CHAPTER 4. TUNNEL IONISATION OF HIGH RYDBERG STATES IN STRONG ELECTRIC FIELDS

calculations for hydrogen-like Rydberg states with similar characteristics.

These results now provide the foundations for: (1) improvements in the Rydberg-state-selective detection schemes used to study resonant energy transfer in collisions of Rydberg He atoms with ground-state NH₃ molecules at low collision energies as presented in Chapter 5, (2) investigations of the dynamics of Rydberg electron wave packets prepared and probed at the classical ionisation threshold in strong electric fields, and (3) the possibility to perform new experimental studies of quantum mechanical tunnelling processes in crossed electric and magnetic field conditions in which classically the electrons dynamics might be expected to be chaotic [83, 84].

Chapter 5

Resonant energy transfer in intrabeam collisions of NH_3 with Rydberg He atoms

The results of the investigation on the ionisation dynamics of Rydberg He atoms described in Chapter 4 provided both a detailed account of how low- ℓ triplet Rydberg states in He ionise, and a stringent test of the calculations used to compute the atomic energy-level structure in electric fields. With this in mind, this chapter describes intrabeam collision experiments performed to study interactions between Rydberg He atoms in 1sns 3S_1 levels and neutral ground-state NH $_3$ molecules at low energies, i.e., at low temperatures. This work, therefore, builds upon the earlier room temperature studies discussed in Chapter 1.1.3. Additionally, the experimental data is compared to a theoretical model of the resonant dipole–dipole interactions between the collision partners based on the impact parameter

method. The results and parts of the text presented in this chapter are based on the work reported in Ref. [85] with adaptations to align with the main themes of this thesis.

5.1 Introduction

In the study of gas-phase chemical dynamics at low temperature, i.e., when $T \lesssim 1$ K, long-range inter-particle interactions, which may be exploited to regulate access to short-range reaction processes, are of particular interest. These interactions can be isotropic or anisotropic, and arise as a result of the static electric dipole polarisabilities or static electric dipole moments of the collision partners, or resonant dipole–dipole interactions between them. The large static electric dipole polarisabilities, static electric dipole moments, and electric dipole transition moments associated with high Rydberg states of atoms and molecules have made them ideally suited to the study of long-range interactions of these kinds in ultracold atomic gases. This has led to the synthesis of long-range diatomic molecules with equilibrium internuclear distances of $\sim 1 \mu m$, known as Rydberg macrodimers, which are formed as a result of the interactions between pairs of Rydberg atoms [6, 7, 8]. In experiments performed at high atom number densities, $\sim 10^{11}$ cm⁻³, the properties of the Rydberg states that give rise to strong long-range interactions, i.e., the large spatial extent of the Rydberg electron wavefunctions and the high density of alternate parity states, have allowed the photoassociation of a class of ultralong-range Rydberg molecules in which an excited Rydberg atom is bound to a ground-state atom located within the Rydberg electron orbit [9, 10].

The evolution of studies of long-range interactions of cold Rydberg atoms or molecules to include those with cold molecules in their electronic ground-states, allows access to a distinct set of molecular interactions that occur on several different length scales. (1) At long range, where the spatial separation, R, between the centres of mass of the ground-state molecule and the atom or molecule in the Rydberg state is much larger than the spatial extent of the Rydberg electron wavefunction, i.e., $R \gg \langle r \rangle$, where $\langle r \rangle$ is the expectation value of the radial position operator acting on the Rydberg electron wavefunction, van der Waals and resonant dipole—dipole interactions dominate. (2) On the intermediate length scale, where $R \simeq \langle r \rangle$ and the ground-state particle is located within the Rydberg electron charge distribution, the formation of ultralong-range Rydberg molecules and electron transfer between the collision partners can occur. (3) At short range, where $R < \langle r \rangle$, the most significant interaction is that of the ground-state molecule with the ion core of the Rydberg atom or molecule.

Experimental studies at each of these length scales have been carried out. Resonant energy transfer in collisions between atoms in Rydberg states (Xe, Rb and He) and polar ground-state molecules (NH₃, HF, HCl, CO) emanating from effusive sources operated at 300 K have been studied [see Chapter 1.1] [12, 13, 22, 23, 24, 25, 26]. This work included, most recently, observations of electric-field controlled transfer of energy from the inversion sublevels in NH₃ to Rydberg states in He and Rb [15, 86]. The formation of negative ions by electron transfer in collisions of atoms in Rydberg states with polar ground-state molecules, such as acetonitrile and cyclobutanone, at collision energies of $\sim 1 \, \text{eV}$ have also been investigated [87].

Short-range ion–molecule reactions, e.g., the $H_2^+ + H_2 \rightarrow H_3^+ + H$ reaction, have been studied at a translational temperature of ~ 8 K in intrabeam experiments involving supersonic molecular beams containing ground-state and Rydberg H_2 [88]. More recently, this reaction, as well as the $He^+ + NH_3$ ion–molecule reaction, have been performed at collision energies as low as $E_{\rm coll}/hc = 0.24$ cm⁻¹ ($E_{\rm coll}/k_{\rm B} \simeq 0.3$ K) in experiments in which beams of Rydberg H_2 (or He) were merged with beams of ground-state H_2 (or NH_3) using the methods of Rydberg-Stark deceleration [17, 43].

5.2 Experiment

The apparatus and general experimental methods used in the work reported here are described in Chapter 3. These particular collision experiments were performed in pulsed supersonic beams of NH₃ seeded in He at a ratio of 1:19. To permit intrabeam collision studies involving the triplet Rydberg states in He, atoms in the metastable 1s2s 3 S₁ level were first generated in a pulsed electric discharge at the exit of a pulsed valve. The pulsed electric potential required to generate the discharge was applied for 30 μ s in the trailing part of the ~ 200 - μ s-long gas pulse. In the region between two copper electrodes [see Figure 3.1 in Chapter 3], the metastable He atoms were excited to the 1s38s 3 S₁ level (denoted $|38s_0\rangle$ in the following, where the subscript indicates the value of m_ℓ) through the 1s3p 3 P₃ intermediate level using a resonance-enhanced two-color two-photon excitation scheme in zero electric field. The CW laser used to drive the 1s3p 3 P₂ \rightarrow 1s38s 3 S₁ transition in this case was stabilised to 12668.919 cm⁻¹. The $|38s_0\rangle$ state (quantum defect $\delta_{38s} = 0.296\,683\,[77]$) was

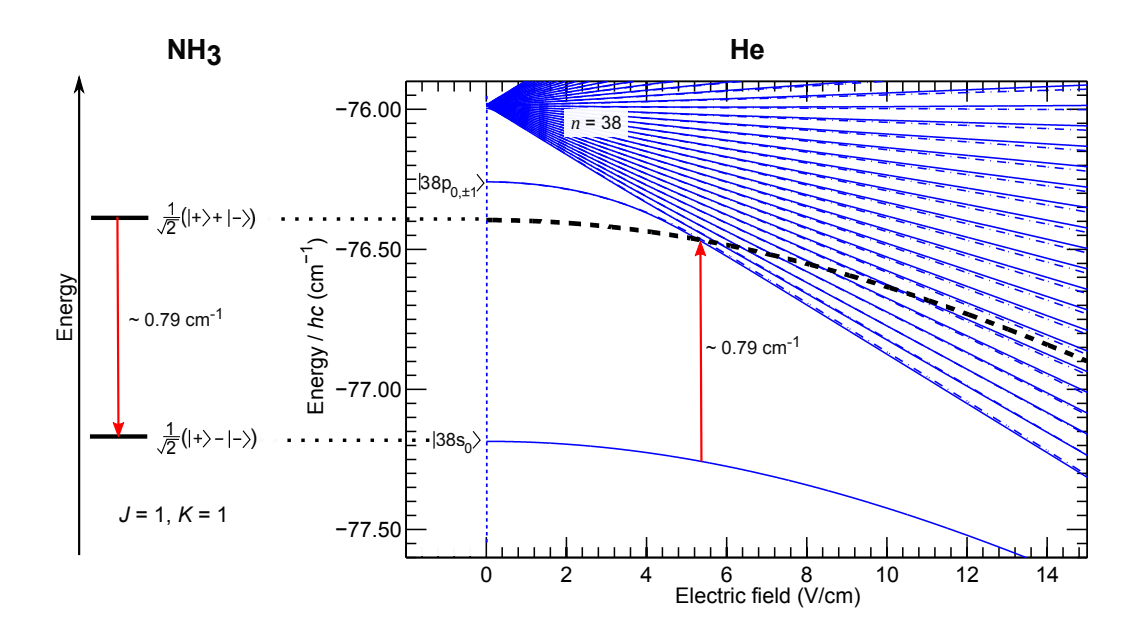


Figure 5.1: Energy-level structure associated with the 0.79 cm⁻¹ ground-state inversion transition in NH₃ (left), and the triplet Rydberg states in He near n = 38 (right). In the Stark map on the right, sub-levels for which $m_{\ell} = 0$ ($|m_{\ell}| = 1$) are indicated by the continuous (dash-dotted) curves. The thick dashed curve, 0.79 cm⁻¹ above the $|38s'_0\rangle$ state, corresponds to the energy of the $|38s'_0\rangle$ state offset by the NH₃ inversion transition wavenumber as indicated.

chosen for these experiments because transitions from it to the $\left|38p'_{0,\pm1}\right\rangle$ state ($\delta_{38p}=0.068\,347$) (the prime indicates the ℓ -mixed character attained in the presence of an electric field) can be readily tuned into resonance with the ground-state inversion transitions in NH₃ using weak electric fields as shown in Figure 5.1. In this particular case the resonance condition is achieved in a field of 5.41 V/cm. After laser photoexcitation, pulsed electric fields of between 0.5 and 14 V/cm were applied to control and study the resonant transfer of energy in collisions between the Rydberg He atoms

and the ground-state NH₃ molecules in the beam. Following an interaction time of 5.5 μ s, the Rydberg atoms were ionised upon the application of a slowly-rising pulsed negative potential to one of the parallel electrodes in the interaction region [see Figure 3.1 in Chapter 3]. The ionised electrons were then accelerated through an aperture in the opposite electrode to a microchannel plate (MCP) detector. This Rydberg-state-selective detection scheme was operated in such a way that individual low- $|m_{\ell}|$ Rydberg states could be identified from their distinct ionisation electric fields [15].

5.3 NH₃ inversion transitions

For the work described in this chapter, it was important to understand the energy-level structure of the NH₃ molecule in order to identify the transitions that occurred during the energy transfer process with Rydberg He atoms. The NH₃ molecule has a finite double-well potential that allows the N atom to tunnel through the plane of the hydrogen atoms and become 'inverted' [Figure 5.2(a)]. As a direct consequence, each rotational energy level, J, is split into a symmetric and antisymmetric component as shown in Figure 5.2(b), where K is the projection of J onto the symmetry axis of the molecule. Inversion transitions, on the order of 1 cm⁻¹, between the symmetric and antisymmetric sublevels within one rotational level are possible if the selection rules are satisfied. These selection rules are: $\Delta J = 0$, $\Delta K = 0$ where $K \neq 0$. The transition dipole moment of an inversion transition, $\langle J, K, +|\hat{\mu}|J, K, -\rangle$, is given by [89]

$$\mu_{J,K} = \sqrt{\frac{\mu_0^2 K^2}{J(J+1)'}} \tag{5.1}$$

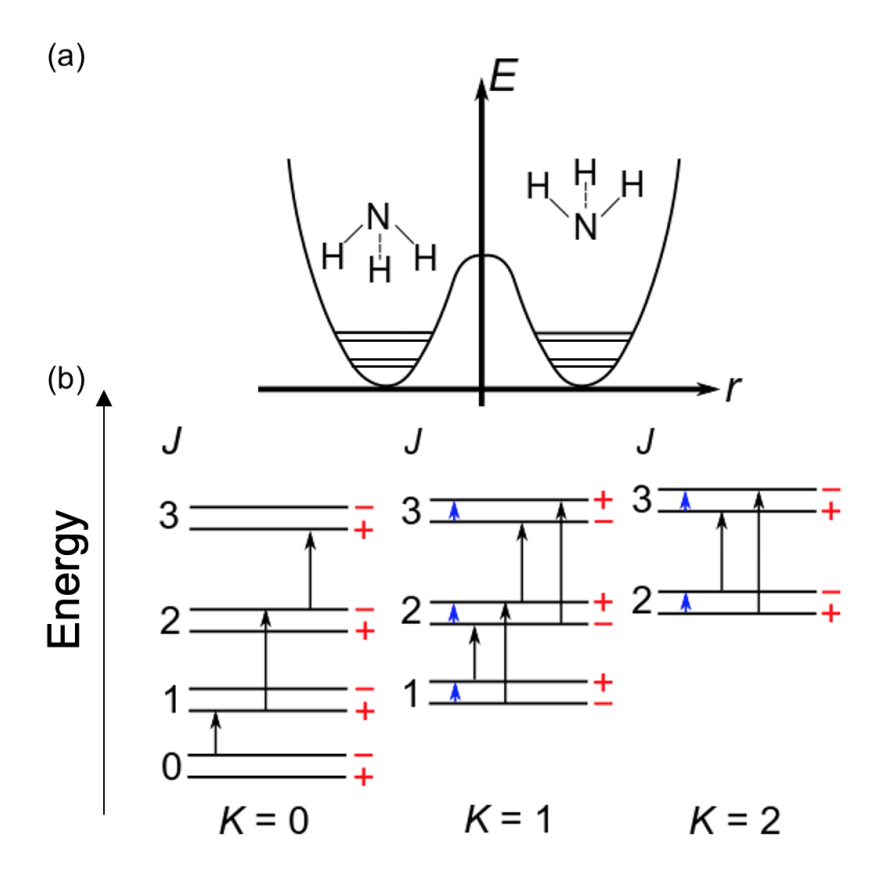


Figure 5.2: (a) The finite double-well potential that allows for the inversion of the NH₃ molecule. (b) Simplified energy-level structure of NH₃ depicting the splitting of each rotational energy level, J as a result of the double-well potential. Inversion transitions are shown with blue arrows, while rotational transitions are shown with black arrows. Due to the electric dipole selection rules, there are no inversion transitions between the rotational sublevels with K = 0 (see text).

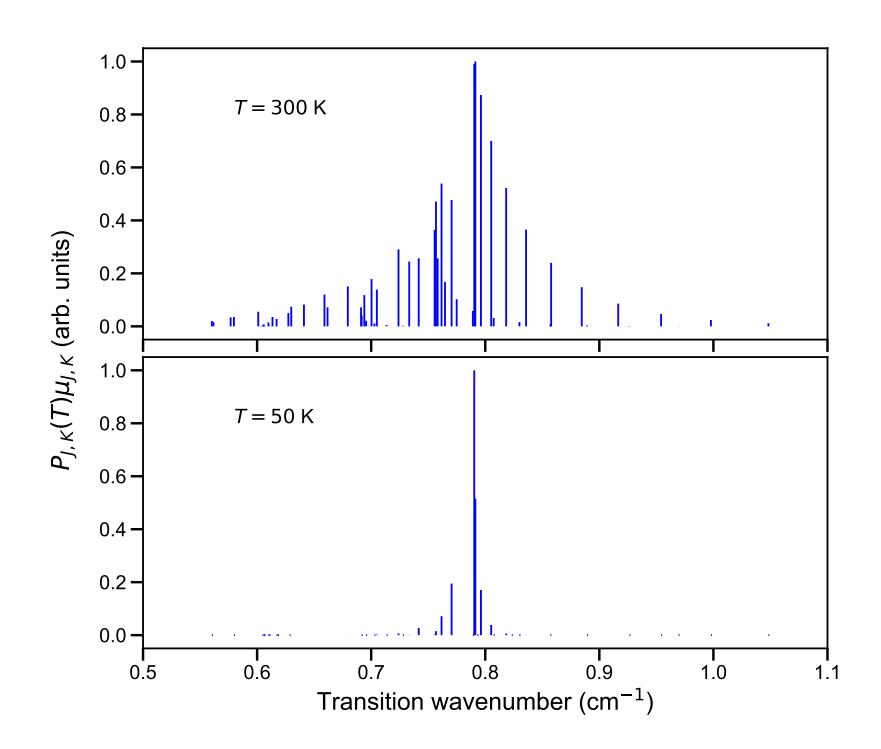


Figure 5.3: The inversion spectra of NH₃ calculated for a rotational temperature of 300 K (top panel) and 50 K (bottom panel). The intensity of a transition is given by the product of the transition dipole moment of an inversion transition, $\mu_{J,K}$, and the Boltzmann factor, $P_{J,K}(T)$. The transition wavenumbers used in the calculations were obtained from Ref. [90] and contain the transitions for J values between 1 and 17.

where μ_0 is the electric dipole transition moment of the molecule, which is 1.468 D for NH₃.

The intensity of an inversion transition is given by the product of $\mu_{J,K}$ and the Boltzmann factor, $P_{J,K}(T)$, which reflects on the relative distribution of the population in each $|J,K\rangle$ state and is given by [89]

$$P_{J,K}(T) = e^{E_{J,K}/k_BT}$$
 (5.2)

CHAPTER 5. RESONANT ENERGY TRANSFER IN INTRABEAM COLLISIONS OF NH₃ WITH RYDBERG HE ATOMS

J	K	\tilde{v} (cm ⁻¹)	Rel. Intensity	Resonance field $(m = 0)$ (V/cm)	Resonance field $(m = 1)$ (V/cm)
1	1	0.79036	1.00	5.29	5.41
2	2	0.79130	0.52	5.27	5.39
2	1	0.77049	0.20	5.64	5.76
3	3	0.79622	0.17	5.18	5.30

Table 5.1: The wavenumbers of the inversion transitions of NH₃ (from Ref. [90]) for selected $|J,K\rangle$ states, the relative intensity of these transitions calculated using $\mu_{J,K}P_{J,K}(T)$ at 50 K, and the expected electric field values at which the inversion transitions in NH₃ become resonant with the $|38s_0\rangle \rightarrow |38p'_{0,\pm 1}\rangle$ transitions in He.

where

$$E_{J,K} = BJ(J+1) + (C-B)K^2$$
(5.3)

is the energy of the $|J,K\rangle$ state. The rotational constants, B and C, are $9.44\,\mathrm{cm^{-1}}$ and $6.20\,\mathrm{cm^{-1}}$ for NH₃, respectively [89]. The calculated inversion spectra of NH₃ using the above values for μ_0 , B, C, and the transition wavenumbers from Ref. [90] are shown in Figure 5.3 for two different internal temperatures. At 300 K, many more rotational states are populated than at 50 K. The spectral lines with an intensity above 0.1 at $T=50\,\mathrm{K}$ are shown in Table 5.1, along with the electric fields at which these inversion transitions become resonant with the $\left|38\mathrm{s}_{0}\right\rangle \rightarrow \left|38\mathrm{p}_{0,\pm1}'\right\rangle$ electronic transition in He.

5.4 Impact parameter method

The calculations performed to aid in the interpretation of the experimental results in this chapter are based on the interaction of two classical electric dipoles. These calculations were performed, as described in Refs. [15, 16, 20], using the impact parameter method [91].

The interaction potential associated with the electric-dipole–dipolecoupling is given by

$$V_{\rm dd}(\vec{R}) = \frac{1}{4\pi\epsilon_0} \left[\frac{\vec{\mu}_{\rm A} \cdot \vec{\mu}_{\rm B}}{R^3} - \frac{3(\vec{\mu}_{\rm A} \cdot \vec{R})(\vec{\mu}_{\rm B} \cdot \vec{R})}{R^5} \right]. \tag{5.4}$$

In this case, the electric dipole moments, $\vec{\mu}_A$ and $\vec{\mu}_B$, are $\vec{\mu}_{He}(F_{int}) = \langle np | \hat{\vec{\mu}} | ns \rangle$ and $\vec{\mu}_{NH_3} = \langle J, K, + | \hat{\vec{\mu}} | J, K, - \rangle$, i.e., the electric-dipole transition moment in He in an electric field, F_{int} , and inversion transition moment in NH₃. The effect of the applied electric field on $\vec{\mu}_{NH_3}$ was neglected because the fields used in the experiments correspond to a Stark energy shift of $< 0.001 \, \text{cm}^{-1}$ for the NH₃ molecule. Hence, $\vec{\mu}_{NH_3}$ is unchanged in the presence of an external electric field and could be calculated using Equation 5.1, while $\vec{\mu}_{He}(F_{int})$ was calculated as described in Chapter 2.3.

Since there was no attempt in the experiments to orient the dipoles of the Rydberg He and NH₃ with respect to each other, the angular dependence of the second term in Equation 5.4 was averaged over all angles. Without considering the consequences that dynamic orientation has as the two dipoles approach each other, the angle averaged interaction potential, $\tilde{V}_{\rm dd}$, can be simplified to

$$\tilde{V}_{\rm dd}(R) = -\frac{\mu_{\rm He}(F_{\rm int})\mu_{\rm NH_3}}{4\pi\epsilon_0 R^3}.$$
 (5.5)

CHAPTER 5. RESONANT ENERGY TRANSFER IN INTRABEAM COLLISIONS OF NH₃ WITH RYDBERG HE ATOMS

Given that $\tilde{V}_{\rm dd}(R) \propto R^{-3}$, this allows for the consideration that

$$ilde{V}_{\mathrm{dd}} \simeq rac{\mu_{\mathrm{He}}(F_{\mathrm{int}})\mu_{\mathrm{NH}_3}}{4\pi\epsilon_0 b^3} ext{ for } R \leq b,$$
 $ilde{V}_{\mathrm{dd}} \simeq 0 ext{ for } R > b,$

where *b* is the impact parameter.

The resonant energy transfer process is assumed to occur when

$$\frac{\tilde{V}_{\rm dd}t}{h} \gtrsim 1,\tag{5.6}$$

where t is the atom–molecule interaction time during which $R \leq b$. When Equation 5.6 is equal to 1, the interaction time is t = b/v, where v is the relative collision speed. Assuming that only a single scattering channel exists, for which the cross section, $\sigma_{RET}(F_{int})$, is given by $\sigma = \pi b^2$, the cross section for resonant energy transfer is given by

$$\sigma_{\text{RET}}(F_{\text{int}}) \simeq \frac{\mu_{\text{He}}(F_{\text{int}})\mu_{\text{NH}_3}}{4\epsilon_0 v h}.$$
 (5.7)

The measured $|38p_1\rangle$ signal can be compared with a calculated quantity that is proportional to the product of Equations 5.2 and 5.7, $P_{J,K}(T)\sigma_{RET}(F_{int})$, and has a dependence on the detuning from resonance. This detuning is assumed to have a Gaussian lineshape, where the FWHM of the Gaussian is related to the atom—molecule interaction time

$$\frac{\Delta E_{\text{FWHM}}}{h} \simeq \frac{v}{b} = \sqrt{\frac{4\pi\epsilon_0 v^3 h}{\mu_{\text{He}}(F_{\text{int}})\mu_{\text{NH}_3}}}$$
 (5.8)

$$= \frac{C_{\text{width}}}{\sqrt{\mu_{\text{He}}(F_{\text{int}})\mu_{\text{NH}_3}}}.$$
 (5.9)

In the analysis of the experiments discussed below, C_{width} is a global fit parameter that is a constant of proportionality associated with the measured resonance width.

5.5 Results

5.5.1 Resonant energy transfer from the inversion intervals

In zero electric field, the electric dipole transition moments associated with the $|38s_0\rangle \rightarrow |38p_1\rangle$ transition in He, and the inversion transitions in NH₃ are $\mu_{38s_0-38p_1}$ = 2976 D and μ_{NH_3} = 1.4 D, respectively. These transitions are not resonant in zero field, as can be seen in Figure 5.1. The electron signal recorded on the MCP detector following the interaction of NH₃ and $|38s_0\rangle$ Rydberg He atoms is shown in Figure 5.4 as a function of both the interaction electric field in the interaction region, and the electron time-offlight in the detection region. In this case, t = 0 denotes the time at which the ramped detection field is switched on. In this figure, a decrease in signal is represented by blue shading, while an increase in electron signal is indicated in red. Since the arrival time at the detector of an electron (resulting from the ionisation of a Rydberg atom) is correlated with the ionisation field of a specific Rydberg state, each of the vertical features seen in Figure 5.4 represent the ionisation of an individual Rydberg state. It is the easiest to identify the strong signal representing the ionisation of the $|38s_0\rangle$ state between 1.44 and 1.49 μ s. From the work in Chapter 4 it is known that np states ionise at slightly higher electric fields than ns states, hence, the electron signal between 1.55 and 1.60 μ s (shown between the green vertical lines) is attributed to ionisation of the $|38p_1\rangle$ state. The electron signal beyond 1.60 µs is caused by secondary electrons created when the field ionised He⁺ ions collide with the metal electrode opposite the electron extraction aperture in the detection region. The cause of this

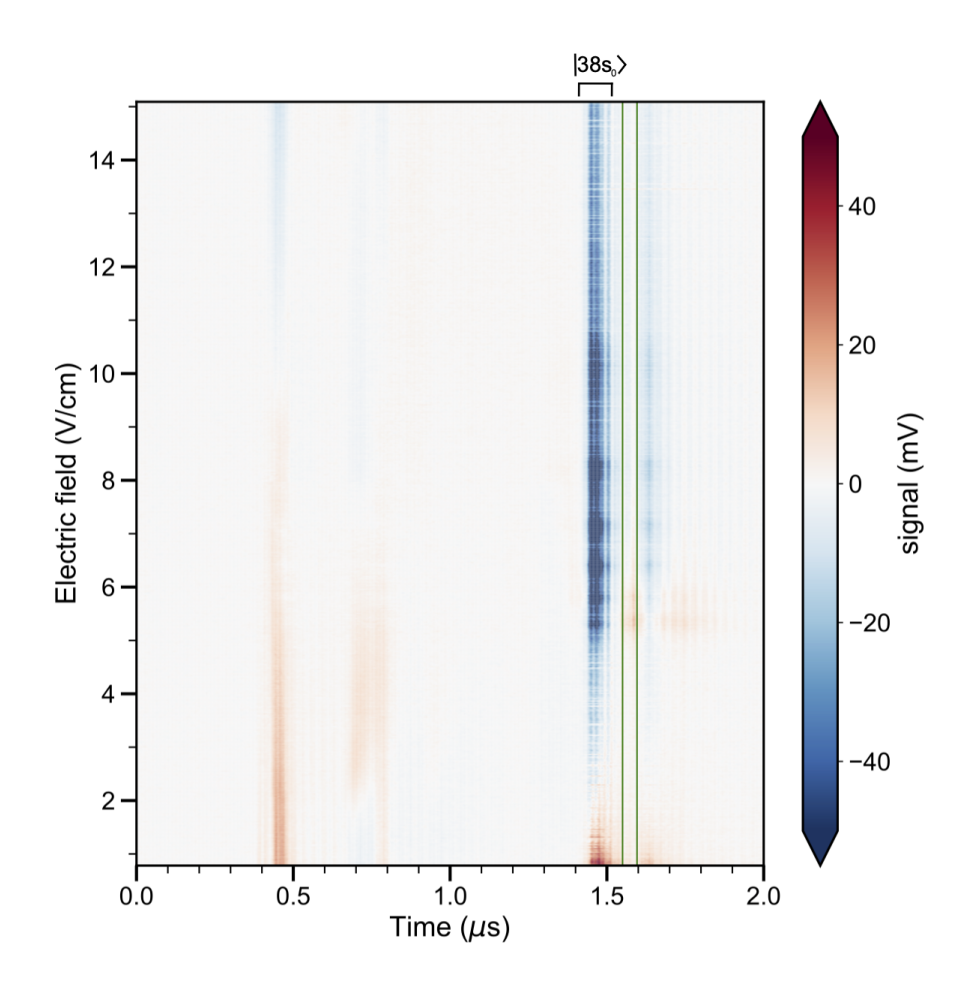


Figure 5.4: The raw electron signal recorded following intrabeam collisions between $|38s_0\rangle$ Rydberg He atoms and neutral ground-state NH₃ molecules. This signal is shown as a function of both the external interaction electric field and the arrival time of the electron at the detector, where t=0 denotes the start of the slowly-rising, ramped, ionisation field. The signal between the two, green, vertical lines results from the ionisation of the $|38p'_1\rangle$ state, while the signal at 1.44-1.49 μs and 0.4-0.8 μs corresponds to the ionisation of the $|38s_0\rangle$ and higher states of He, respectively. In the absence of NH₃ in the beam the only signal recorded on this map is the signal corresponding to the ionisation of the $|38s_0\rangle$ state and the secondary electrons between 1.5 and 1.55 μs

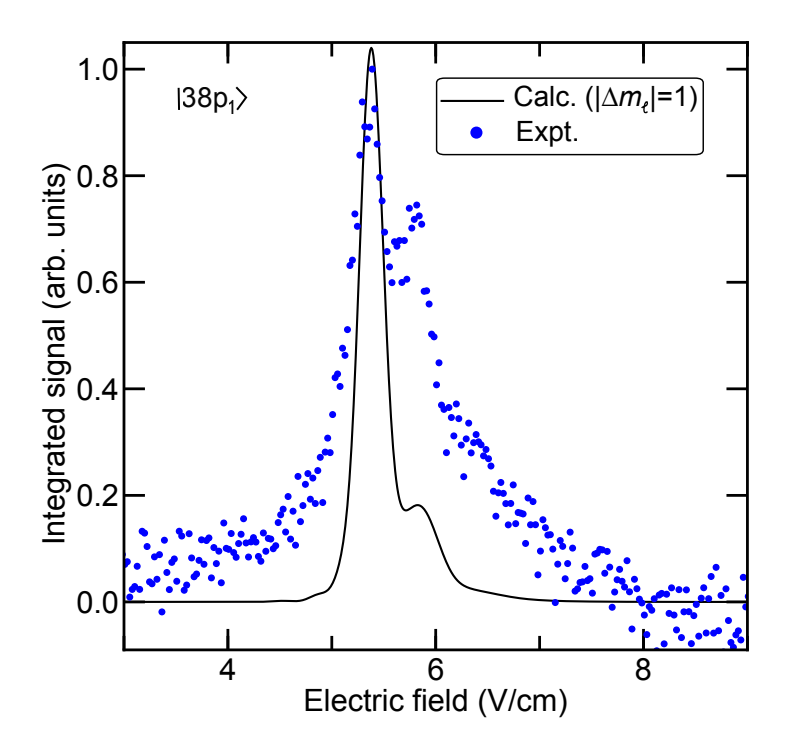


Figure 5.5: Integrated $|38p_1\rangle$ electron signal (blue points) recorded following collisions in the electric fields indicated on the horizontal axis. The resonance lineshape calculated considering only collision-induced energy transfer from the $|38s_0'\rangle$ state to the $|38p_1'\rangle$ state is indicated by the continuous curve.

effect was checked and confirmed in the work described in Chapter 4. Lastly, the signal between 0.4 and 0.8 μ s is attributed to the ionisation of higher-n ℓ -mixed Rydberg Stark states. This is discussed in detail further below.

There is a distinct increase in the $|38p_1\rangle$ electron signal within the green vertical lines in Figure 5.4 for interaction electric fields between 5.0 and 6.5 V/cm. This is shown in more detail in Figure 5.5, where the measured integrated electron signal in this region is represented as blue points. The

increase in the population of the $|38p_1\rangle$ state in fields between 4 and 7 V/cm, with a maximum at 5.39 V/cm and a shoulder at 5.84 V/cm, results from the resonant transfer of energy from the inversion sublevels in NH₃ to the He atoms. The intensity maximum of this resonance lies within 0.02 V/cm of the expected values (Table 5.1) for the energy transfer from the inversion transitions in the $|J,K\rangle = |2,2\rangle$ and $|1,1\rangle$ states. In this field, $\mu_{38s_0'-38p_1'} \simeq 1370$ D and μ_{NH_3} is unchanged from its zero-field value. The measured electric-field dependence of the energy transfer process has been compared to the results of calculations based on the interaction of two electric dipoles corresponding to the He and NH₃ transition dipole moments. These calculations were performed, as described in Section 5.4 using the impact parameter method. The experimental data are in good agreement with the results of these calculations (continuous curve in Figure 5.5). The broadening of the resonance on the high field side in the calculated curve is a consequence of the rotational state dependence of the inversion intervals in the molecules, which have a non-zero rotational temperature. The broadening observed in the experimental data arises from a combination of this, the limited Rydberg-Stark-state resolution in the detection of the $|38p_1\rangle$ atoms, and contributions from energy-level shifts arising from the dipole-dipole interaction between the atoms and molecules that are not accounted for in the calculations.

The resonant increase in the $|38p_1\rangle$ electron signal seen in Figure 5.5 corresponds to a decrease in the electron signal from the $|38s_0\rangle$ state over the same range of electric fields. This can be seen in the data presented in Figure 5.6(b). It is evident from this data that the transition to the $|38p_1'\rangle$

state does not represent the only resonance that occurs in the experiments. Five additional resonances, in fields between 5 and 11 V/cm, are seen. These correspond to transitions from the $|38s_0'\rangle$ state to consecutive ℓ -mixed Rydberg-Stark states that lie above the $|38p_1'\rangle$ state in energy. The spectral overlap of these transitions with the NH₃ inversion transitions can be seen by following the thick dashed curves in Figure 5.1 and Figure 5.6(a).

The fields in which the transitions to the $\left|38p_{1}'\right\rangle$ state, and the subsequent five Rydberg-Stark states, coincide with the inversion transition in the $\left|J,K\right\rangle=\left|1,1\right\rangle$ state of NH₃ at 0.79036 cm⁻¹ and are indicated in Figure 5.6(a) by the vertical lines. It can be seen from the positions of these lines in Figure 5.6(b) - which is presented with the same horizontal scale - that these crossing points correspond exactly to electric fields at which the resonances are observed in the experimental data. The results of the calculations for transitions to the $m_{\ell}=0$ states (rather than the $m_{\ell}=1$ states) or where the transition in He was considered to be resonant with a different rotational state in NH₃ did not yield a good agreement with the experimental data. As the electric field is increased, the observed resonances broaden because the induced electric dipole moment associated with the Stark shift of the $\left|38s_{0}'\right\rangle$ state tends toward that of the Stark states to which resonant energy transfer occurs. Consequently, the wavenumber interval between the $\left|38s_{0}'\right\rangle$ state and these Stark states changes more gradually with field strength.

Calculated spectra for $\Delta m_\ell = 0$ ($\Delta m_\ell = \pm 1$) transitions between the Rydberg states are shown as the continuous (dashed) curves in Figure 5.6(b). In the calculations, the features observed at low electric field strengths, i.e., in fields between 5 and 7 V/cm, are most sensitive to the centre-of-mass colli-

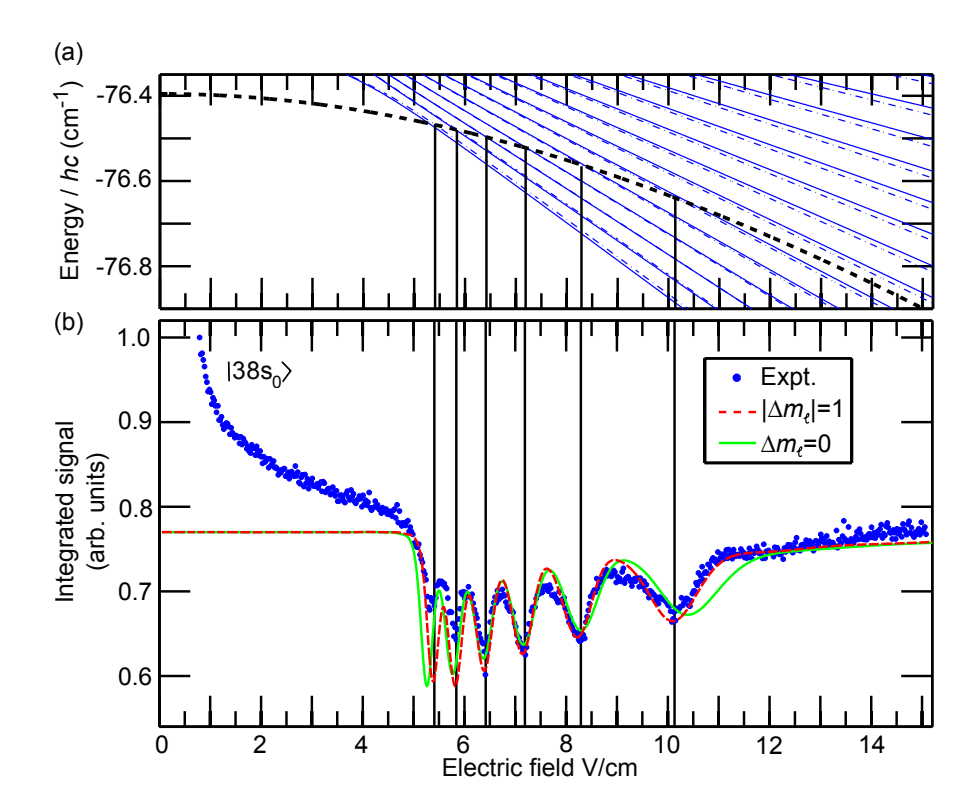


Figure 5.6: (a) A portion of the Stark map in Figure 5.1, and (b) the integrated $|38s_0\rangle$ electron-signal (blue points) recorded following collisions in the electric fields indicated on the horizontal axis. The calculated intensities of the resonances that result from transitions to $m_\ell = 0$ ($|m_\ell| = 1$) states are shown as the continuous (dashed) curves. The vertical lines connecting (a) and (b) indicate the electric fields for which transitions from the $|38s_0'\rangle$ state in He are resonant with the inversion transitions in NH₃.

sion speed. Best agreement between the experimental and calculated data was found for collision speeds of ~ 70 m/s, which corresponds to a typical center-of-mass collision energy $E_{\text{coll}}/k_{\text{B}} \simeq 1$ K. The widths of the resonances in the data in Figure 5.6(b) also depend on the rotational temperature of the NH₃ molecules. The resonances in fields above 7.5 V/cm are most sensitive to this temperature, with the broad curve in the data between fields of 11 and 14 V/cm especially so. It was found that best agreement between the experimental and calculated data, particularly in this higher electric field region, occurred for a rotational temperature of ~ 50 K. In the seeded supersonic molecular beam used in the experiment, relative translational temperatures of ~ 1 K are typical. Generally, the rotational and translational temperatures in these beams equilibrate. However, an increase in the rotational temperature caused by the application of the pulsed discharge used to prepare the metastable He atoms is not unexpected. We therefore attribute the 50 K rotational temperature, inferred by comparing the experimental data with the results of calculations, to heating in the discharge. With appropriate lasers, which were not available at the time, this could have been inferred directly using REMPI. In Figure 5.6(b), the results of the calculations for $\Delta m_{\ell} = \pm 1$ transitions between the Rydberg states is in slightly better agreement with the experimental data. This is most notable in electric fields above 8 V/cm, and the most likely reason for this preference is that statistically it is more probable for the NH₃ molecules to be aligned in such a way to give $|\Delta m_{\ell}| = 1$ transitions rather than $\Delta m_{\ell} = 0$. In general, the widths and intensities of the measured and calculated resonances in Figure 5.6(b) are in good quantitative agreement, with the exception of the

intensities of the first two features at 5.4 and 5.8 V/cm, which are weaker in the experiments than in the calculations. We attribute this discrepancy to effects of van der Waals interactions between the atoms and the molecules as they undergo resonant energy transfer.

The spectral widths of the sharp resonances in the data in Figure 5.6(b) can be determined from the calculated Stark shifts of each transition. The full-width-at-half-maximum of these range from 0.015 cm⁻¹ ($\equiv 460 \text{ MHz}$), for the resonance associated with the transition to the $\left|38p_{1}'\right>$ state at 5.39 V/cm, to 0.021 cm⁻¹ (\equiv 640 MHz), for the transition observed in the highest field. The impact parameter method used in the calculations in Figure 5.6(b) is based on the assumption that energy-level shifts arising from the resonant dipole-dipole interactions between the atoms and the molecules can be neglected. This is a valid assumption at high centreof-mass collision speeds, but less so at low speed where these energylevel shifts are on the same scale as the collision energy. To estimate the significance of these effects in the present experiments, the observed resonance widths may be compared to the typical resonant dipole-dipole interaction energy for an NH₃ molecule located at the edge of the Rydberg electron charge distribution, i.e., at $\langle r \rangle$. This is approximately the closest point of approach between the collision partners after which the NH₃ molecule enters the Rydberg electron charge distribution and the form of the interaction potential changes. Since $\langle r_{38s} \rangle \simeq 110$ nm, and $\mu_{38s'_0-38p'_1}(F=5.39 \text{ V/cm}) \simeq 1370 \text{ D}$, the corresponding dipole–dipole energy shift is $\Delta E_{\rm dd}/hc \simeq 0.007~{\rm cm}^{-1}~(\equiv 220~{\rm MHz})$. This energy shift is on the same order of magnitude as the widths of the resonances in the experiments. Therefore the conditions under which the experiments were performed must represent the limit of the range of validity of the impact parameter method used in the analysis of the data, as it does not account for effects of these types of energy-level shifts between the collision partners. This observation provides a strong motivation for a more complete theoretical treatment of the dipole—dipole interactions in this collision system. Such work will be essential for the accurate interpretation of future experiments at lower collisions energies.

By comparing the observed $|38p'_1\rangle$ signal in Figure 5.6(b) to the signal recorded by Zhelyazkova and Hogan [15] in Figure 1.3, the improvement in resolution that an intrabeam setup has over a cross-molecular setup with an effusive NH₃ beam is clearly seen. The intrabeam method allowed the energy of collisions to be reduced from 300 K to 1 K, while also decreasing the internal temperature of NH₃ through the supersonic expansion. Ultimately, these changes meant that fewer rotational levels in NH₃ contributed to the energy transfer process and resulted in resonance widths that are approximately one order of magnitude smaller for the intrabeam method than by using a cross-molecular setup with an effusive NH₃ beam. Additionally, in this intrabeam collision apparatus, resonances were resolved for each of the transitions from the $|38s_0\rangle$ state to the five closest ℓ -mixed Stark level states. This level of resolution was not achieved in the previous study.

5.5.2 Other population transfer mechanisms

The main aim of the experiments described in this chapter was to observe the energy transfer process between Rydberg He atoms and NH₃ molecules via the inversion transitions in the latter. However, the calculated curves in Figure 5.6(b) do not account for the notable decrease in the $|38s_0\rangle$ electron signal seen in fields between 0.5 and 5 V/cm. Given that the calculations assume a single scattering channel, this suggests that additional transitions, other than those associated with NH₃ inversion, also transfer population out of the $|38s_0'\rangle$ state in the experiments.

The additional features in the electric field ionisation profile of the Rydberg states that are shown in Figure 5.4 are observed at earlier times (i.e. arrive earlier at the detector), they, therefore, most likely correspond to the ionisation of Rydberg atoms in higher n states because these will ionise at lower fields. The slowly-rising, pulsed, voltage applied for detection by electric field ionisation was used to infer the ionisation fields of these features. The feature appearing between $0.4-0.8\mu s$ in Figure 5.4 corresponds to an ionisation field of ~ 30 V/cm, while the features between $1.44-1.49\mu s$ correspond to ionisation fields of 83-94 V/cm. Using a scaling based on the ionisation studies performed in Chapter 4, it was found that the former feature corresponds to the ionisation of a Rydberg state with n=51, while the latter corresponding to n=46.

The NH₃ rotational temperature of ~ 50 K in the experiments meant that several excited rotational states as well as rotational levels in vibrational states with v > 0 can be populated. Consequently, NH₃ can undergo rotational transitions such as the $|J,K\rangle = |2,2\rangle \rightarrow |3,2\rangle$ transition in the first

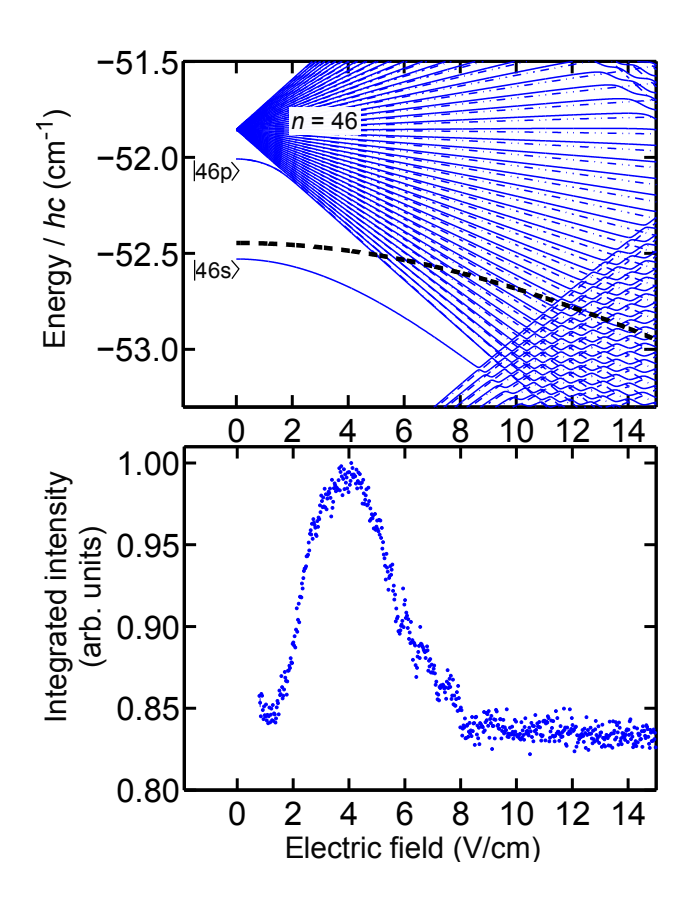


Figure 5.7: (a) Stark map calculated near the n=46 level in He, where the thick-dashed line depicts the energy of the $|38s\rangle$ state offset by the $|J,K\rangle=|2,2\rangle \rightarrow |3,2\rangle$ transition at ~ 24.74 cm⁻¹ in the first excited vibrational state in NH₃. (b) The integrated electron signal measured following the collisions of the $|38s_0\rangle$ state in He and ground-state NH₃ molecules.

excited vibrational level that occurs at $\sim 24.74~\rm cm^{-1}$ [92]. This rotational transition was found to be resonant with the $|38s\rangle \rightarrow |46p\rangle$ transition in He that occurs at 24.66 cm⁻¹ corresponding to an interaction electric field of ~ 5 V/cm. This is shown in Figure 5.7(a) where the thick-dashed curve represents the energy of the 38s state offset by the energy that is associated with the $|2,2\rangle \rightarrow |3,2\rangle$ rotational transition in NH₃. In Figure 5.7(b) the integrated signal associated with the additional feature observed between $1.44 - 1.49\mu$ s in Figure 5.4 is shown as a function of the interaction electric field. The maximum of the resonance observed in this signal occurs at ~4 V/cm. Assuming that the integrated signal shown in Figure 5.7(b) corresponds to the ionisation of the n=46 state, as inferred from from the ionisation field, then this resonance provides evidence that the $|2,2\rangle \rightarrow |3,2\rangle$ transition in NH₃ couples the $|38s\rangle \rightarrow |46p\rangle$ transition in He. Transitions between excited rotational states that are resonant with electronic transitions in Rydberg atoms have been observed previously to give rise to energy transfer [see Chapter 1.1], hence, this is the most likely cause for the overall decrease in the $|38s_0\rangle$ electron signal observed in low fields in Figure 5.6(b). However, with appropriate lasers, which were not available at the time, this interpretation could have been confirmed using REMPI.

Since the feature that appears at the earliest electron time of flight in Figure 5.4 corresponds to a state with even higher principle quantum number, the resolution of the observed signal did not allow a reasonable estimate of which rotational transitions in NH₃ could be causing the transfer of energy to the atoms. At this point, it is important to highlight that there

can also be other events occurring during the collisions. For example, it is possible that the NH₃ molecule can dissociate through the electron bombardment in the discharge, with the fragments then interacting with the Rydberg He atoms. This would provide a more complicated interpretation because a high-resolution spectra of the fragmented molecules must also be considered.

5.6 Conclusions

We have observed Rydberg-state-resolved and electric-field-controlled resonant energy transfer in collisions of ground-state NH $_3$ molecules with Rydberg He atoms. The intrabeam method used, where NH $_3$ was seeded in a pulsed supersonic beam of He, enabled the experiments to be performed at translational temperatures of ~ 1 K. The measured data exhibit resonance widths of ~ 0.017 cm $^{-1}$ ($\equiv 500$ MHz) and represent the limit of the impact parameter method use to calculate the energy transfer cross-section arising as a result of dipole—dipole interactions between the collision partners. The energy transfer from both inversion transitions, and rotational transitions in NH $_3$ were observed to occur with Rydberg He atoms. However, while it was possible to record high-resolution data for the former, it was not possible for the latter due to the limitations of the detection scheme.

The work presented here paves the way for experiments at even lower collision energies in which the resonant dipole—dipole interactions between the atoms and the molecules are more strongly affected by the energy-level shifts of the collision partners and may be exploited to regulate access to short-range chemical dynamics. It is foreseen that in future

CHAPTER 5. RESONANT ENERGY TRANSFER IN INTRABEAM COLLISIONS OF NH₃ WITH RYDBERG HE ATOMS

experiments, the centre-of-mass collision energies in these experiments can be manipulated using the methods of Rydberg-Stark deceleration [48].

Chapter 6

Spin-changing collisions

The atom-molecule collisions described in Chapter 5 resulted in a change in the orbital angular momentum of the Rydberg electron as a result of resonant electric dipole—dipole interactions with ground-state NH_3 molecules. The corresponding interaction potential can be expressed as

$$V_{\rm dd} \sim \frac{|\vec{\mu}_{\rm A}| \cdot |\vec{\mu}_{\rm B}|}{4\pi\epsilon_0 |\vec{R}_{\rm AB}|^3},\tag{6.1}$$

where $\vec{\mu}_A$ and $\vec{\mu}_B$ are electric dipole transition moments for transitions in systems A (the He atom) and B (the NH₃ molecule), respectively, and \vec{R}_{AB} is the distance between A and B. In this chapter, studies of cold atom–molecule collisions that result in a spin-flip of the Rydberg electron in He are presented. This process arises as a result of magnetic dipole–dipole interactions, for which the interaction potential can be expressed as

$$V_{\rm dd} \sim \frac{\mu_0(|\vec{\mu}_{\rm A}| \cdot |\vec{\mu}_{\rm B}|)}{4\pi |\vec{R}_{\rm AB}|^3}.$$
 (6.2)

In this case, $\vec{\mu}_A$ and $\vec{\mu}_B$ are magnetic dipole moments for transitions in

systems A and B, respectively, and μ_0 is the vacuum permittivity. These magnetic dipole-dipole interactions are generally much weaker than the electric dipole—dipole interactions discussed in Chapter 5 at the same interparticle distance. The difference in magnitude of the electric dipole-dipole and magnetic dipole-dipole coupling can be determined by calculating the respective interaction energies, using Equations (6.1) and (6.2). If $|\vec{\mu}_{\rm elec}| \sim 1ea_0$ and $|\vec{\mu}_{\rm mag}| \sim 1\mu_{\rm B}$, i.e., the typical atomic units of electric and magnetic dipole moment, then the interaction energy $V_{\rm dd}/hc \sim$ $3 \times 10^{-8} \text{ cm}^{-1}$ and $4 \times 10^{-13} \text{ cm}^{-1}$ for the electric dipole-dipole and magnetic dipole-dipole interactions, respectively, when the particle density is 1 x 10^{12} cm⁻³, and hence $\langle R \rangle \sim 1 \mu m$. Because magnetic dipole–dipole interactions are significantly weaker than electric-dipole-dipole interactions, for a magnetic dipole interaction to cause a change in the quantum state of an atom during a collision, the translational temperature must be low so that the interaction occurs for a long period of time, or the atoms must have near degenerate levels between which state changing can occur.

Many studies on spin-changing transitions and singlet-triplet mixing have focussed on the low Rydberg states in He. In particular, the observation by Lees and Skinner [93] of collisional spin changing that involved the reaction $\text{He}(1snp\ ^1P_1) + \text{He}(1s^2\ ^1S_0) \rightarrow \text{He}(1snd\ ^3D_2) + \text{He}(1s^2\ ^1S_0)$ has received a lot of attention (see Refs. [94, 95, 96, 97, 98]) because it is a spin forbidden transition. To explain this result, St John and Fowler[99] proposed the 'F cascade model' where the collision of the atom in the ¹P term with the ground state atom proceeds by first populating the ^{1,3}F term, followed by a 'cascade' transition to the ³D term. In this model, the wavefunction

for the nF level can no longer be written as pure singlet or triplet, because the spin-orbit interaction mixes the spin states. Instead, it is described as being an admixture of singlet and triplet states. The 'F cascade model', therefore, does not violate the Wigner spin-conservation rule and explains the occurrence of the $n^1P \rightarrow n^3D$ transition. The extent of the singlet-triplet mixing must, therefore, depend strongly on the orbital angular momentum of the outer electron. Both experiments [95] and calculations [94, 100, 101] agree that as the orbital angular momentum increases the extent of singlet-triplet mixing increases for low Rydberg levels in He. The extent of this mixing is zero for S states and becomes significant for F states, while for G states, the Russel-Saunders coupling scheme is no longer valid because the singlet-triplet mixing is complete [94].

In the experiments described in this chapter, Rydberg He atoms were prepared in the n=38-40 triplet-P levels, and underwent collisions with ground-state O_2 molecules in the presence of an external electric field in an intrabeam collision apparatus. The transfer of the Rydberg state population to ℓ -mixed singlet Stark states following these collisions was observed by quantum-state-selective, pulsed, electric-field ionisation. These experiments exploited the tunability of the energy level structure of the Rydberg atoms in weak electric fields to enhance the transfer of population from the triplet state to the singlet state. Accordingly, the interpretation of the experimental results requires calculations of the Stark effect in the Rydberg states that take into account spin-orbit effects and these are, therefore, also described in this chapter. The results presented here concern primarily Rydberg He atoms prepared near the n=39 level, however, experiments

were also performed for two other principle quantum numbers to confirm the interpretation of the data.

6.1 Experiment

The experimental setup used in this work was similar to that described in Chapter 3 and Chapter 5. The experiments were performed in two stages. In the first stage, pure He supersonic beams were generated, while in the second stage, seeded beams containing O_2 and He, at a ratio of 1:19 by pressure, were generated. Apart from this adjustment, the set-up and procedures were the same for both stages of the experiments. In the laser photoexcitation region, a UV laser was used to the drive the 1s2s ${}^{3}S_{1} \rightarrow$ $1s3p^{3}P_{2}$ transition at 25 708.587 6 cm⁻¹ (= 388.975 1 nm), and an IR laser then drove the 1s3p $^3P_2 \rightarrow 1s39s/39d$ transition to ℓ -mixed Rydberg-Stark states in weak electric fields. In the following, the excited state prepared in this way is referred to as the 1s39p 3 P_I level, since it would evolve to this level if the electric field was adiabatically switched off. The excitation scheme was implemented in a small electric field of ~ 5 V/cm generated by applying a negative potential to the upper electrode, E₁, in the excitation/interaction region [see Figure 3.1 in Chapter 3]. The energetic position of the triplet state excited is represented by the star in the Stark map in Figure 6.1. A pulsed potential, adjusted between -10 V and +10 V, was then applied to the upper electrode, E₁, [see Figure 3.1 in Chapter 3] after photoexcitation to generate the electric field in which atom-molecule collisions occurred for \sim 6 μs , i.e. the length of time of the applied electric field pulse. The Rydberg He atoms (or Rydberg He atoms and O₂ molecules), therefore,

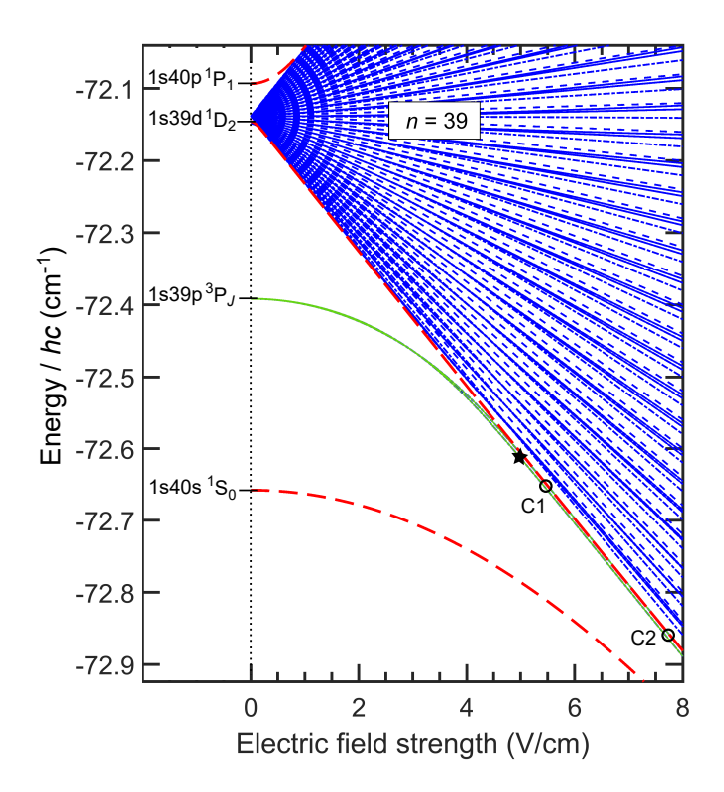


Figure 6.1: Stark map of triplet and singlet Rydberg states in He close to n = 39. The singlet levels are indicated as dashed red curves, while the triplet Rydberg states with $|M_J| = 0.1$, and 2 are shown as continuous, dash-dotted and dashed blue curves, respectively. The triplet state prepared in the experiments by laser photoexcitation (the $1s39p^3P_J$ state) is represented by the green curve. This state was excited in a field of ~ 5 V/cm, as indicated by the star. The two avoided crossings between the $39p^3P_J$ and $39d^4D_2$ states are enclosed by the circles labelled C1 and C2. See text for more details.

interacted for $\sim 6~\mu s$ in the specified electric field before the field was switched off. To detect the Rydberg He atoms, a slowly-rising potential was applied to the lower electrode, E_2 , [see Figure 3.1 in Chapter 3] after the excited atoms had travelled $\sim 25~\text{mm}$ from where excitation occurred. This potential rose to -250 V within 2 μs at a rate of \sim -60 V/cm/ μs at the time of ionisation. The electrons produced following ionisation were then accelerated through a $\sim 4\text{-mm-diameter}$ hole in E_1 to a microchannel (MCP) detector and collected for detection.

6.1.1 Cancelling stray magnetic and electric fields

To determine the parameters that best minimise the stray magnetic and electric fields in the excitation/interaction region in the apparatus, Rydberg He atoms were prepared in the $1\text{s}39\text{s}^3\text{S}_1$ level and high resolution microwave spectroscopy of the $1\text{s}39\text{s}^3\text{S}_1 \rightarrow 1\text{s}39\text{p}^3\text{P}_{0,1,2}$ transition was performed.

This was achieved by applying a pulse of microwave radiation in the presence of a small electric field, generated by applying a pulsed voltage to the upper electrode, E_1 [see Figure 3.1 in Chapter 3], for 2 μ s. The amplitude of this electric field pulse was varied to find the value that yields the narrowest resonance, i.e., the one that best minimised stray electric fields. It was found that the narrowest resonance with a FWHM of ~ 900 kHz occurred when the offset voltage was +40 mV.

The cancellation of magnetic fields was also carried out once the stray electric field was nullified. Magnetic field cancellation was achieved by applying currents to a set of coils wound around the outside of the vacuum

chamber. These coils were oriented parallel and perpendicular to the atomic beam propagation. Both sets of coils were connected to separate power supplies that controlled the current flowing through them. First, the parallel coils were used to minimise the stray magnetic fields, followed by the perpendicular coils. The parameters determined for this process, that resulted in the optimal stray magnetic field cancellation, were a current of -0.04 A for the parallel coils and a current of -0.5 A for the perpendicular coils, resulting in a resonance with a FWHM of ~ 400 kHz.

6.2 Spin-orbit Stark map calculation

To account for spin-orbit effects in the Rydberg states in helium, the Hamiltonian in Equation 2.3 can be expressed in the $|n, L, S, J, M_J\rangle$ basis, where L is the total electron orbital angular momentum quantum number, S is the total electron spin quantum number, J is the total angular momentum quantum number, and M_J is the projection of J onto the laboratory quantisation axis. In this basis, the matrix elements arising from the interaction with an electric field, can be expressed as

$$\left\langle n'L'S'J'M'_{J}|\hat{H}_{\mathrm{Stark}}|n,L,S,J,M_{J}\right\rangle = \delta_{M_{J},M'_{J}}eF_{z}\left\langle n'L'|r|nL\right\rangle \times \dots$$

$$\sum_{M_{L}=M_{J}+M_{S}} \left[(-1)^{L'+L-2S+2M_{J}} \sqrt{(2J+1)(2J'+1)} \begin{pmatrix} L & S & J \\ M_{L} & M_{J}-M_{L} & -M_{J} \end{pmatrix} \right] \times \dots$$

$$\begin{pmatrix} L' & S & J' \\ M_{L} & M_{J}-M_{L} & -M_{J} \end{pmatrix} (-1)^{L'-M'_{L}} \sqrt{\max(L,L')} \begin{pmatrix} L' & 1 & L \\ -M'_{J} & 0 & M_{L} \end{pmatrix}$$

where the radial integrals $\langle n'L'|r|nL \rangle$ were calculated using the Numerov method. The Stark map in Figure 6.1 shows the Rydberg states in He

with values of n close to 39. In this figure, the triplet Rydberg states with $|M_J| = 0.1$, and 2 are shown as continuous, dash-dotted and dashed blue curves, respectively, with the $1 ext{s} ext{39p}^3 ext{P}_J$ level labeled explicitly as it is the level of interest in this study. To calculate the Stark shifts of triplet levels shown in Figure 6.1 all Rydberg states from n = 35 to n = 45 were included. The three, long-dashed, red curves in Figure 6.1 are singlet levels. These include the $1 ext{s} ext{39d}^1 ext{D}_2$ level that is of particular interest in the work described here. All other the singlet levels, although accounted for completely in the calculations, were omitted from the figure for clarity.

It was important to test the accuracy of the Stark structure calculations carried out using the above approach. This was done by recording laser photoexcitation spectra near the transition to the levels with n=39 in weak electric fields and comparing the results with the calculated Stark map. In the laser spectra, the J=0 and J=1 levels of the $1 \text{s} 39 \text{p}^3 \text{P}_J$ level were too close in energy to resolve, however, the J=2 level was found to be separated from the J=0,1 levels by 0.0065 cm^{-1} (not shown). This separation was found to be the same to 4 decimal places as in the calculated Stark map, indicating a level of accuracy adequate for the work described here.

6.3 Electric-field-induced spin changing

The electron signal measured after preparing He atoms in the $1s 39p \,^3P_J$ levels and subsequent detection by ramped, pulsed, electric-field ionisation is shown for two different interaction electric fields in Figure 6.2. In this figure, the signal measured following the application of an electric field

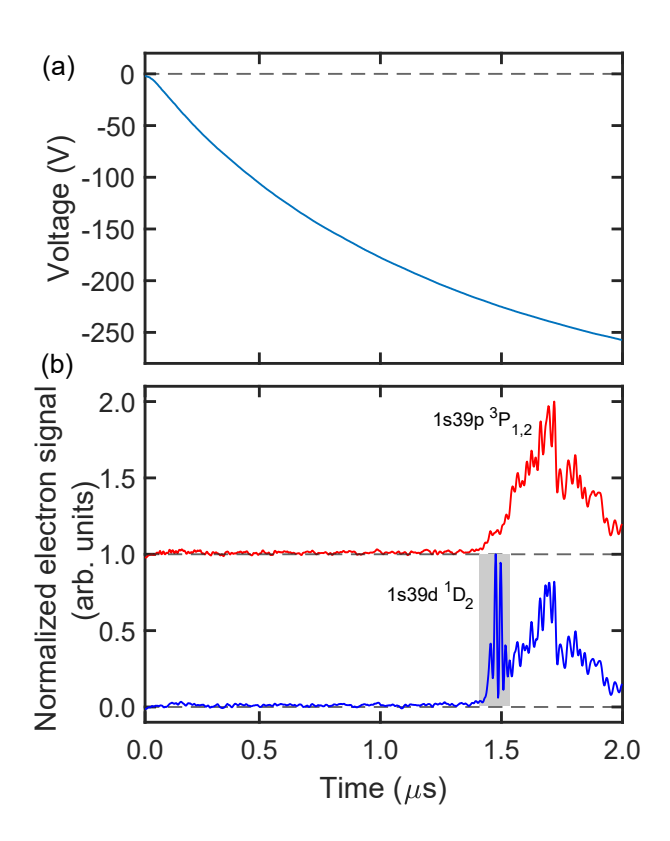


Figure 6.2: (a) The slowly-rising, ramped, potential applied to ionise the Rydberg He atoms during the detection step in the experiments. (b) The electron signals recorded at two different applied electric fields: at the crossing labelled C1 in Figure 6.1 (lower trace shown in blue) and away from the crossing (upper trace shown in red).

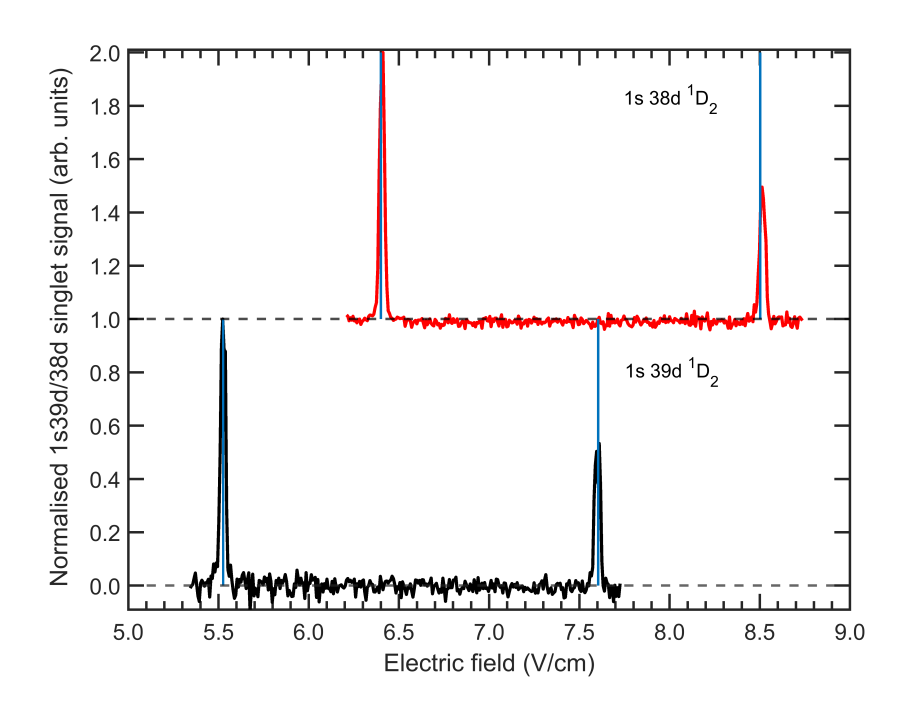


Figure 6.3: The integrated $1s \, 38d \, ^1D_2$ and $1s \, 39d \, ^1D_2$ electron signal recorded for Rydberg atoms prepared in the $1s \, 38p \, ^3P_J$ level and Rydberg atoms prepared in the $1s \, 39p \, ^3P_J$ level after an evolution time of 6 μs in the electric field indicated on the horizontal axis . The vertical lines represent the calculated electric fields at which there is an avoided crossing between the Stark shifted $1s \, 38p \, ^3P_1$ ($39p \, ^3P_1$) and $38d \, ^1D_2$ ($39d \, ^1D_2$) levels with $M_J = 0$.

at the crossing labelled C1 in Figure 6.1 and away from the crossing are shown in blue and red, respectively. Crossing C1 represents the avoided crossing between the Stark shifted $1s \, 39p \, ^3P_J$ and $1s \, 39d \, ^1D_2$ levels. For the signal measured at the crossing, there is a decrease in intensity of the signal from the initially prepared $1s \, 39p \, ^3P_J$ level, but there is also an additional feature observed at earlier arrival times at the detector when compared with the signal observed away from the crossing. A similar observation was made for the second crossing between the $1s \, 39p \, ^3P_J$ and $1s \, 39d \, ^1D_2$ levels labelled as C2 in Figure 6.1. This suggests that when the atoms evolve in the field at the avoided crossing, some population transfer from the triplet to the singlet state occurs as a result of the spin-orbit interaction.

The integrated electron signal associated with the population of the $1 \, s \, n d^{\, 1}D_2$ level, recorded as a function of electric field for Rydberg He atoms prepared initially in the $1 \, s \, n p^{\, 3}P_J$ level, is shown in Figure 6.3, for two different values of n. The energy difference between the $1 \, s \, 39 \, p^{\, 3}P_1$ and $1 \, s \, 39 \, d^{\, 1}D_2$ states for $M_J = 0$ is shown in Figure 6.4. In this figure, it can be seen that there are two "avoided" crossings between these states at ~ 5.5 and 7.6 V/cm, these fields are indicated by the vertical lines in Figure 6.3 and closely align with the resonances observed in the experiments. The calculated fields for the two avoided crossings between $1 \, s \, 38 \, p^{\, 3}P_1$ and $1 \, s \, 38 \, d^{\, 1}D_2$ levels also matched closely the resonances seen in the experimental data in the top panel in Figure 6.3. The agreement between the experiment and the results of the calculations suggests that the non-adiabatic evolution of the Rydberg helium atoms at the avoided crossings leads to population transfer from the triplet to the singlet state.

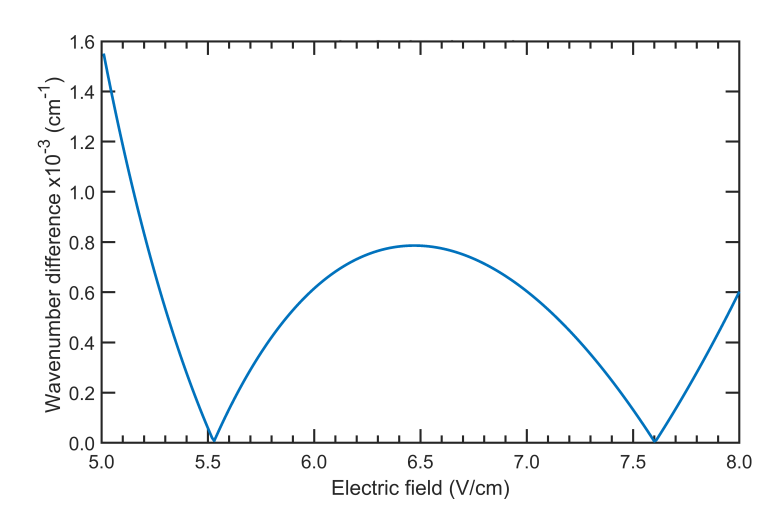


Figure 6.4: The wavenumber difference between the Stark shifted $1s \, 39p \, ^3P_1$ and $1s \, 39d \, ^1D_2$ levels as a function of electric field, as calculated from the energy level diagram in Figure 6.1. The minima in this plot indicate two avoided crossings formed between these states at ~ 5.5 V/cm and ~ 7.6 V/cm.

6.4 Collision-induced spin changing

Following the observation of spin-changing induced by the application of external electric fields, O_2 molecules were mixed with He atoms in the supersonic beam at a ratio of 1:19, in a set of experiments aimed at investigating the effect this would have on the results described in the previous section. The reason O_2 was chosen as a collision partner was because in its $X^3\Sigma_g^-$ ground electronic state it is paramagnetic, due to having two unpaired electrons. This allows for the occurrence of magnetic dipole—dipole interactions between the ground-state O_2 and the Rydberg He atoms.

For this set of experiments, the Rydberg He atoms were, once again, prepared in the 1s 39p 3P_I level and underwent intrabeam collisions with O_2

molecules in the presence of an applied electric field. The recorded electron signal, originating from the $1s\,39d\,^1D_2$ level, showed two resonances at the same electric field values as seen in the experimental data in Figure 6.3, suggesting that electric-field induced spin-changing is still occurring in the presence of O_2 . However, an additional feature of these resonances was also observed. For both of the resonances, a broad shoulder is apparent on the low electric-field side with the O_2 in the beam. This broadening is not seen in the absence of the O_2 molecules. This feature is shown in detail for the first resonance in Figure 6.5, where the error bars correspond to the standard deviation of 5 repeated measurements. The signal strength on the low-field side of the main resonance is significantly larger than the uncertainty, suggesting that the interaction of the Rydberg He atoms with the O_2 causes this additional contribution to the spin-changing.

The electric field switching process, which induces the non-adiabatic evolution of the excited atoms from the singlet to the triplet Stark states in the absence of the O_2 molecules, is expected to be most effective in fields just beyond each avoided crossing that occurs in the Stark maps, in which the spin-orbit interactions is taken into account. However, the singlet-triplet mixing is of a comparable strength before and after each crossing. The collisional spin-changing arising from the interaction with the ground-state O_2 is most clearly seen on the low-field side of the avoided crossing in Figure 6.5 because it is not masked by the non-adiabiatic evolution of the excited states in the electric field.

To calculate the cross-section for the collision-induced spin changing reaction between Rydberg He and ground-state O₂, Equation 5.9 can be

used. In this case, the magnetic-dipole-magnetic-dipole interaction results in a cross section on the order of 10^{-18} cm². This is a lot lower than the electric-dipole – electric-dipole interaction cross-section described in Chapter 5 that resulted in the energy transfer collisions between Rydberg He and ground-state NH₃ molecules, which is on the order of 10⁻¹⁰ cm². This significant difference would indicate that the signal corresponding to the spin changing would be 10⁻⁸ smaller than the signal that was observed for the energy transfer collisions. However, the transfer of population was observed to be on the same order for both of these processes. The most likely explanation for this is that the spin changing collision that occurs between the Rydberg He atom and the ground-state molecule needs to be considered as the interaction of the molecule with a diffuse electron cloud of the Rydberg atom rather than a point charge. Although the cross-section for the spin-changing collision between O₂ and an isolated electron would be on the order of 10^{-18} cm², if we consider the Rydberg electron as having a large charge distribution with a large area, the cross-section for collision induced spin-changing is closer to 10^{-10} cm².

It is worth noting here that O_2 was also replaced by ground-state N_2 molecules in the same experiment as mentioned in this section. In this case, however, the shoulder resonance that is seen in Figure 6.5 for the reaction between the Rydberg He atoms and O_2 molecules was not observed to be significantly larger than the uncertainty. This is most likely because N_2 is not paramagnetic so is unable to have the same magnetic dipole—dipole interactions with the Rydberg He atoms that O_2 molecules can.

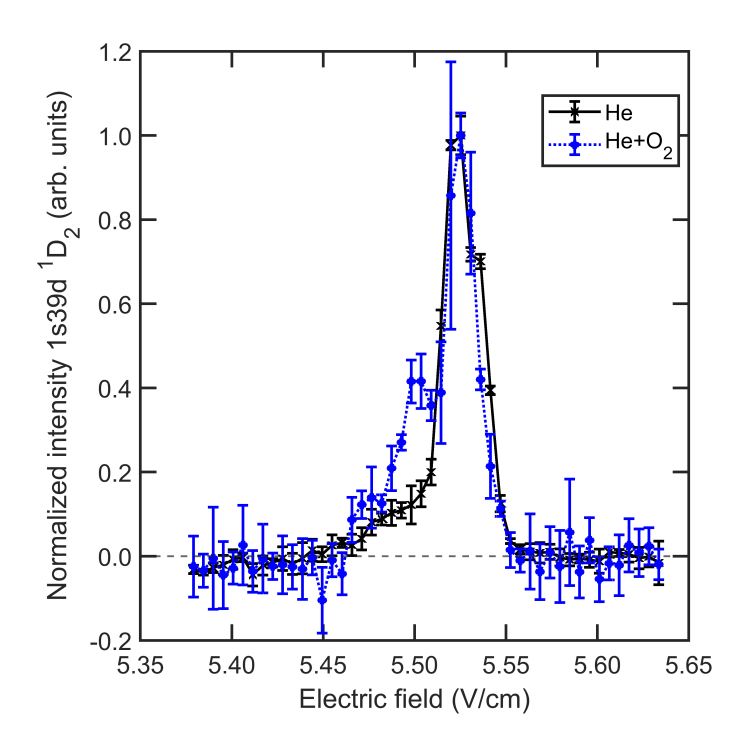


Figure 6.5: The He $1s39d^1D_2$ signal recorded following collisions between Rydberg He atoms prepared in the $1s39p^3P_1$ level and ground-state O_2 molecules (blue-dotted curve). This signal was collected at electric fields near to the first avoided crossing between the $1s39p^3P_1$ and $1s39d^1D_2$ states in He as seen in Figure 6.1. A shoulder peak is observed on the low-field side of the main resonance that is not seen when O_2 molecules are absent (black-solid curve). The error bars correspond to the standard deviation of 5 repeated measurements.

6.5 Conclusions

In this chapter, it was shown that for He atoms prepared in the n = 38 - 40 triplet-P levels, electric fields can be used to control singlet-triplet mixing, which arises as a result of spin-orbit interactions. This was achieved by exciting triplet-P states and experimentally recording the evolution into singlet-D states while the electric field in the interaction region was varied.

In addition, if a ground-state molecule with a magnetic-dipole moment is introduced, in this case O_2 , it was shown that collisions of Rydberg He atoms with O_2 can induce spin-changing to occur on the low-electric-field side of each of the observed electric-field induced spin-changing resonances. This is the first observation of a near-resonant collision-induced spin-changing process involving Rydberg atoms and molecules. The intrabeam collision setup used in this work led to favourable conditions for this observation because it allowed for low-energy collisions and long interaction times between cold O_2 and the Rydberg He atoms. This approach now opens a new route to studying the effects of electron spin in these types of atom–molecule interactions.

Chapter 7

Conclusions and outlook

The work described in this thesis has shown that Rydberg atoms and ground-state molecules can be used as model systems to study resonant energy transfer and spin-changing at low temperatures. The key experimental techniques that enabled the studies presented in Chapters 5 and 6 were quantum-state-selective detection of the Rydberg atoms by pulsed electric field ionisation, and access to the low-temperature collision regime in an intrabeam collision apparatus.

Accurate interpretations of the results presented in Chapters 5 and 6 required thorough understanding of the ionisation dynamics of triplet Rydberg states. Precise calculations of the Rydberg energy-level structure in the presence of electric fields were used throughout to both guide the experiments and interpret the observations. The validity of this state-selective technique was proven in the work described in Chapter 4, where Rydberg states were prepared in a range of electric fields including at fields within 1 cm⁻¹ of the classical adiabatic ionisation threshold for the Rydberg He states of interest and, at each field, was in good quantitative agreement

with energy-level structure calculations.

The electric-field pulse sequence used to ionise the Rydberg He atoms in the work in Chapters 5 and 6 was evidently adequate for the experiments described in this thesis. However, based on studies of tunnel ionisation in strong electric fields presented in Chapter 4, improvements would be needed in order to achieve higher state selectivity. This improvement could, for example, involve applying ionisation pulses with a fast initial rising component followed by a reduction in the time-dependence close to the ionisation threshold of the states of interest for maximal selectivity.

In Chapters 5 and 6, the collisions between Rydberg He atoms and ground-state neutral molecules were performed using the intrabeam collision method. This was ideally suited to these types of experiments. Due to the dispersion of the beam between the valve and the excitation region, Rydberg excitation selects a subset of the velocities from the distribution resulting in velocity selection. The velocity slip arising as a result of the different masses of the atoms and molecules resulted in translation temperatures of $\lesssim 1$ K. In Chapter 5, this collision technique led to the observation of the first fully Rydberg state resolved resonant energy transfer between Rydberg He atoms and ground-state NH $_3$ molecules. This work expanded on previous studies by Hogan and Zhelyazkova that investigated resonant energy transfer between Rydberg He atoms and room temperature NH $_3$ molecules using a crossed molecular beam setup. This crossed beam apparatus lead to higher collision energies and, hence, did not make it possible to resolve the energy transfer to individual He Rydberg states.

In the future, investigations of resonant energy transfer between Ryd-

berg He atoms and ground-state NH₃ molecules could be further improved by gaining more detailed information on the velocity distribution of both the collision partners, and the orientation of the NH₃ molecules. This can be achieved using resonance-enhanced multiphoton ionisation (REMPI) spectroscopic techniques, as used, for example, in Ref. [44]. Furthermore, the upper inversion sublevel in NH₃ is low-field seeking so molecules in this state can be guided in an electrostatic guide, such as a quadrupole or hexapole guide, allowing for the state-selection of the NH₃ beam and giving greater control over the collision process. Another improvement would be to optimise the mixing ratio of the He and NH₃ as this could lead to even lower energy collisions. This is because the smaller the proportion of NH₃ in the beam the less collisions that occur between the NH₃ molecules and, therefore, the closer the velocity and velocity spread of the beam are to a pure He beam.

As mentioned in Chapter 5, it was not possible to obtain high-resolution measurements of rotational energy transfer from the NH_3 to Rydberg He atoms during the collision process. Firstly, understanding the rotational state distribution of NH_3 would narrow down the possible rotational states that could be involved in this additional energy transfer process. Also, cooling the valve with, for example, water or liquid nitrogen, would stabilise the temperature and potentially lower the rotational temperature of the NH_3 molecules so that only lower-lying levels are occupied. However, there is also the limitation of the detection scheme which makes it hard to resolve the close lying high n levels in Rydberg He. The suggestion above by which higher state selectivity could be achieved using modified electric

field ionisation pulse sequences could also be employed here.

The impact parameter method, used to calculate the intensity and widths of the resonances expected following energy transfer between Rydberg He atoms and NH₃, showed good agreement with the observed experimental data, especially in terms of the resonance widths. To identify the limit of the impact parameter model, Rydberg states with different electric dipole moments would need to be studied. Follow on work on this topic by others in the group now suggests that these resonance widths are strongly dependent on the transition moments. For weak transitions moments, the widths of the resonances increase as the transition moment increases. This indicates that they are dominated by the rate of energy transfer between atoms and molecules rather than transit time in the collision.

This work identified the threshold at which the simple model of two interacting dipoles can be used to accurately describe the energy transfer collisions between Rydberg atoms and neutral molecules. For collision energies lower than those achieved in this thesis, this model would no longer suffice. This is because at lower collision speeds other interactions between the Rydberg atom and the neutral molecule would need to be considered. One of these interactions is, for example, the Rydberg electron scattering from the neutral molecule, the other is the interaction between the molecule and the ion core of the Rydberg atom.

Bibliography

- [1] E. AMALDI and E. SEGRE, Nuovo Cimento 11, 145 (1934).
- [2] E. Fermi, Nuovo Cimento 11, 157 (1934).
- [3] F. Merkt, Annu. Rev. Phys. Chem. 48, 675 (1997).
- [4] J. Lim, H. Lee, and J. Ahn, J. Korean Phys. Soc. 63, 867 (2013).
- [5] J. Alexander and S. Gulyaev, *Astrophys. J.* **828**, 1 (2016).
- [6] S. M. Farooqi, D. Tong, S. Krishnan, J. Stanojevic, Y. P. Zhang, J. R. Ensher, A. S. Estrin, C. Boisseau, R. Cote, E. E. Eyler, and P. L. Gould, *Phys. Rev. Lett.* 91, 183002 (2003).
- [7] K. R. Overstreet, A. Schwettmann, J. Tallant, D. Booth, and J. P. Shaffer, *Nat. Phys.* **5**, 581 (2009).
- [8] J. Deiglmayr, H. Sassmannshausen, P. Pillet, and F. Merkt, *Phys. Rev. Lett.* **113** (2014).
- [9] V. Bendkowsky, B. Butscher, J. Nipper, J. P. Shaffer, R. Löw, and T. Pfau, *Nature* 458, 1005 (2009).

- [10] A. Gaj, A. T. Krupp, J. B. Balewski, R. Loew, S. Hofferberth, and T. Pfau, *Nat. Commun.* **5**, 4546 (2014).
- [11] T. P. Softley, Int. Rev. Phys. Chem. 23, 1 (2004).
- [12] F. G. Kellert, K. A. Smith, R. D. Rundel, F. B. Dunning, and R. F. Stebbings, *J. Chem. Phys.* **72**, 3179 (1980).
- [13] L. Petitjean, F. Gounand, and P. R. Fournier, *Phys. Rev. A* **30**, 71 (1984).
- [14] L. Petitjean, F. Gounand, and P. R. Fournier, *Phys. Rev. A* **30**, 736 (1984).
- [15] V. Zhelyazkova and S. D. Hogan, *Phys. Rev. A* **95**, 042710 (2017).
- [16] V. Zhelyazkova and S. D. Hogan, J. Chem. Phys. 147, 244302 (2017).
- [17] P. Allmendinger, J. Deiglmayr, K. Hoveler, O. Schullian, and F. Merkt, J. Chem. Phys. 145 (2016).
- [18] M. Zeppenfeld, Euro. Phys. Lett. 118, 13002 (2017).
- [19] T. F. Gallagher, *Rydberg Atoms*, Cambridge University Press, Cambridge, 1994.
- [20] T. F. Gallagher, *Phys. Rep.* **210**, 319 (1992).
- [21] T. F. Gallagher, L. M. Humphrey, W. E. Cooke, R. M. Hill, and S. A. Edelstein, *Phys. Rev. A* **16**, 1098 (1977).
- [22] K. A. Smith, F. G. Kellert, R. D. Rundel, F. B. Dunning, and R. F. Stebbings, *Phys. Rev. Lett.* **40**, 1362 (1978).

- [23] L. Petitjean, F. Gounand, and P. R. Fournier, *Phys. Rev. A* **33**, 143 (1986).
- [24] C. Higgs, K. A. Smith, G. B. McMillian, F. B. Dunning, and R. F. Stebbings, *J. Phys. B At. Mol. Phys.* **14**, L285 (1981).
- [25] R. F. Stebbings, F. B. Dunning, and C. Higgs, J. Electron Spectrosc. Relat. Phenom. 23, 333 (1981).
- [26] A. KALAMARIDES, L. N. GOELLER, K. A. SMITH, F. B. DUNNING,M. KIMURA, and N. F. LANE, *Phys. Rev. A* 36, 3108 (1987).
- [27] F. G. Kellert, C. Higgs, K. A. Smith, G. F. Hildebrandt, F. B. Dunning, and R. F. Stebbings, *J. Chem. Phys* **72**, 6312 (1980).
- [28] J. Toscano, H. J. Lewandowski, and B. R. Heazlewood, *Phys. Chem. Chem. Phys.* **22**, 9180 (2020).
- [29] M. Costes and C. Naulin, Chem. Sci. 7, 2462 (2016).
- [30] S. Chefdeville, T. Stoecklin, A. Bergeat, K. M. Hickson, C. Naulin, and M. Costes, *Phys. Rev. Lett.* **109**, 023201 (2012).
- [31] A. Bergeat, A. Faure, S. B. Morales, A. Moudens, and C. Naulin, *J. Phys. Chem. A* **124**, 259 (2020).
- [32] S. Chefdeville, Y. Kalugina, S. Y. T. van de Meerakker, C. Naulin, F. Lique, and M. Costes, *Science* **341**, 1094 (2013).
- [33] M. Wernli, P. Valiron, A. Faure, L. Wiesenfeld, P. Jankowski, and K. Szalewicz, *Astron. Astrophys.* **446**, 367 (2006).

- [34] B. Yang, P. C. Stancil, N. Balakrishnan, and R. C. Forrey, *Astrophys. J.* **718**, 1062 (2010).
- [35] H. L. Bethlem, G. Berden, and G. Meijer, *Phys. Rev. Lett.* **83**, 1558 (1999).
- [36] S. N. Vogels, J. Onvlee, S. Chefdeville, A. van der Avoird, G. C. Groenenboom, and S. Y. T. van de Meerakker, *Science* **350**, 787 (2015).
- [37] S. N. Vogels, T. Karman, J. Klos, M. Besemer, J. Onvlee, A. van der Avoird, G. C. Groenenboom, and S. Y. T. van de Meerakker, *Nat. Chem.* **10**, 435 (2018).
- [38] A. B. Henson, S. Gersten, Y. Shagam, J. Narevicius, and E. Narevicius, *Science* 338, 234 (2012).
- [39] J. Jankunas, B. Bertsche, K. Jachymski, M. Hapka, and A. Osterwalder, *J. Chem. Phys.* **140**, 244302 (2014).
- [40] J. Zou, S. D. S. Gordon, and A. Osterwalder, *Phys. Rev. Lett.* **123**, 133401 (2019).
- [41] S. D. S. GORDON and A. OSTERWALDER, *Phys. Chem. Chem. Phys.* **21**, 14306 (2019).
- [42] P. Allmendinger, J. Deiglmayr, O. Schullian, K. Höveler, J. A. Agner, H. Schmutz, and F. Merkt, *Chem. Phys. Chem.* 17, 3596 (2016).
- [43] V. Zhelyazkova, F. B. V. Martins, J. A. Agner, H. Schmutz, and F. Merkt, *Phys. Chem. Chem. Phys.* **23**, 21606 (2021).

- [44] E. W. Steer, L. S. Petralia, C. M. Western, B. R. Heazlewood, and T. P. Softley, *J. Mol. Spec.* **332**, 94 (2017).
- [45] C. Amarasinghe and A. G. Suits, J. Phys. Chem. Lett. 8, 5153 (2017).
- [46] W. E. Perreault, N. Mukherjee, and R. N. Zare, *Science* **358**, 356 (2017).
- [47] M. J. SEATON, Rep. Prog. Phys. 46, 167 (1983).
- [48] S. D. Hogan, EPJ Tech. Instrum. 3, 2 (2016).
- [49] H. A. Bethe and E. E. Salpeter, Quantum mechanics of one- and twoelectron atoms, Springer, Berlin, 1957.
- [50] D. Kaiser, *Phys. Lett. A* **A 51**, 375 (1975).
- [51] F. GOUNAND, P. R. FOURNIER, J. CUVELLIER, and J. BERLANDE, *Phys. Lett. A* **59**, 23 (1976).
- [52] C. E. Theodosiou, *Phys. Rev. A* **30**, 2881 (1984).
- [53] M. Mack, J. Grimmel, F. Karlewski, L. Sárkány, H. Hattermann, and J. Fortágh, *Phys. Rev. A* **92**, 012517 (2015).
- [54] D. B. Branden, T. Juhasz, T. Mahlokozera, C. Vesa, R. O. Wilson,
 M. Zheng, A. Kortyna, and D. A. Tate, J. Phys. B: At. Mol. Opt. Phys.
 43, 015002 (2010).
- [55] Z.-G. Feng, L.-J. Zhang, J.-M. Zhao, C.-Y. Li, and S.-T. Jia, *J. Phys. B: At. Mol. Opt. Phys.* **42**, 145303 (2009).

- [56] M. L. ZIMMERMAN, M. G. LITTMAN, M. M. KASH, and D. KLEPPNER, *Phys. Rev. A* **20**, 2251 (1979).
- [57] R. N. Zare, Angular momentum, John Wiley & Sons, New York, 1988.
- [58] J. M. Blatt, J. Comp. Phys. 1, 382 (1967).
- [59] T. Halfmann, J. Koensgen, and K. Bergmann, *Meas. Sci. Technol.* **11**, 1510 (2000).
- [60] S. D. Hogan, Y. Houston, and B. Wei, J. Phys. B: At. Mol. Opt. Phys.51, 145002 (2018).
- [61] H. W. LIEPMANN and A. Roshko, *Elements of Gas Dynamics*, Dover Publications, New York, 2001.
- [62] M. D. Morse, 2 Supersonic Beam Sources, in *Atomic, Molecular, and Optical Physics: Atoms and Molecules*, edited by F. Dunning and R. G. Hulet, volume 29 of *Experimental Methods in the Physical Sciences*, pp. 21–47, Academic Press, 1996.
- [63] H. Ashkenas and F. S. Sherman, The structure and utilization of supersonic free jets in low density wind tunnels, in *Rarefield Gas Dynamics*. *Proceedings of the 4th International Symposium 1964*, edited by J. H. de Leuuw, volume 2, pp. 84–105, Academic Press, New York, 1966.
- [64] H. Haberland, U. Buck, and M. Tolle, *Rev. Sci. Instrum.* **56**, 1712 (1985).

- [65] J. B. Anderson, R. P. Andres, and J. B. Fenn, *Adv. Chem. Phys.* **10**, 275 (1966).
- [66] M. Capitelli, C. M. Ferreira, B. F. Gordiets, and A. I. Osipov, *Plasma Kinetics in Atmospheric Gases*, Springer, Berlin, 2000.
- [67] S. S. Hodgman, R. G. Dall, L. J. Byron, K. G. H. Baldwin, S. J. Buckman, and A. G. Truscott, *Phys. Rev. Lett.* **103**, 053002 (2009).
- [68] A. Wedding, A. Mikosza, and J. Williams, J. Electron Spectrosc. Relat. *Phenom.* **52**, 689 (1990).
- [69] K. Gawlas and S. D. Hogan, Phys. Rev. A 99, 013421 (2019).
- [70] R. Feynman, J. Hollingsworth, M. Vennettilli, T. Budner, R. Zmiewski, D. P. Fahey, T. J. Carroll, and M. W. Noel, *Phys. Rev. A* 92, 043412 (2015).
- [71] T. W. Ducas, M. G. Littman, R. R. Freeman, and D. Kleppner, *Phys. Rev. Lett.* **35**, 366 (1975).
- [72] S. B. Hill, C. B. Haich, Z. Zhou, P. Nordlander, and F. B. Dunning, *Phys. Rev. Lett.* **85**, 5444 (2000).
- [73] G. R. LLOYD, S. R. PROCTER, and T. P. SOFTLEY, *Phys. Rev. Lett.* **95**, 133202 (2005).
- [74] J. A. GIBBARD, M. DETHLEFSEN, M. KOHLHOFF, C. J. RENNICK, E. So, M. FORD, and T. P. SOFTLEY, Phys. Rev. Lett. 115, 093201 (2015).
- [75] R. J. Damburg and V. V. Kolosov, *J. Phys. B: At. Mol. Phys.* **12**, 2637 (1979).

- [76] S. D. Hogan, Cold atoms and molecules by Zeeman deceleration and Rydberg-Stark deceleration, Habilitation Thesis, ETH, Zürich, 2012.
- [77] G. W. F. Drake, Phys. Scr. T83, 83 (1999).
- [78] J. Grimmel, M. Stecker, M. Kaiser, F. Karlewski, L. Torralbo-Campo, A. Günther, and J. Fortágh, *Phys. Rev. A* **96**, 013427 (2017).
- [79] S. Sahoo and Y. K. Ho, J. Phys. B: At. Mol. Opt. Phys. 33, 2195 (2000).
- [80] L. D. LANDAU, Phys. Z. Sowjetunion 2, 46 (1932).
- [81] C. Zener, Proc. Math. Phys. Eng. Sci. 137, 696 (1932).
- [82] A. M. Alonso, L. Gurung, B. A. D. Sukra, S. D. Hogan, and D. B. Cassidy, *Phys. Rev. A* **98**, 053417 (2018).
- [83] G. Raithel and H. Walther, *Phys. Rev. A* 49, 1646 (1994).
- [84] C. Dong, P. Wang, M. Du, T. Uzer, and Y. Lan, *Mod. Phys. Lett. B* **30**, 1650183 (2016).
- [85] K. Gawlas and S. D. Hogan, J. Phys. Chem. Lett. 11, 83 (2020).
- [86] F. Jarisch and M. Zeppenfeld, New J. Phys. 20, 113044 (2018).
- [87] C. Desfrancois, H. Abdoul-Carime, J. P. Schermann, L. J. Dube, J. B. A. Mitchell, J. W. McConkey, and C. E. Brion, Charge transfer between rydberg atoms and polar molecules or clusters, in *Physics of Electronic and Atomic Collisions*, number 360, pp. 599–608, AIP Press, 1995.

- [88] S. T. Pratt, J. L. Dehmer, P. M. Dehmer, and W. A. Chupka, *J. Chem. Phys.* **101**, 882 (1994).
- [89] C. Townes and A. Schawlow, *Microwave Spectroscopy*, McGraw-Hill, London, 1955.
- [90] C. C. Costain, Phys. Rev. 82, 108 (1951).
- [91] M. J. SEATON, Proc. Phys. Soc. 79, 1105 (1962).
- [92] A. R. Al Derzi, T. Furtenbacher, J. Tennyson, S. N. Yurchenko, and A. G. Csaszar, *J. Quant. Spectrosc. Radiat. Transf.* **161**, 117 (2015).
- [93] J. H. Lees and H. W. B. Skinner, *Proc. Roy. Soc.* **A137**, 186 (1932).
- [94] R. M. Parish and R. W. Mires, Phys. Rev. A 4, 2145 (1971).
- [95] D. Krause and E. A. Soltysik, *Phys. Rev. A* **6**, 694 (1972).
- [96] A. F. J. van Raan and van Eck J., J. Phys. B: At. Mol. Phys. 7, 2003 (1974).
- [97] A. F. J. VAN RAAN and H. G. M. HEIDEMAN, J. Phys. B: At. Mol. Phys.7, L216 (1974).
- [98] J. E. CHILTON and C. L. CHUN, *Phys. Rev. A* **58**, 4572 (1998).
- [99] R. M. St. John and R. G. Fowler, *Phys. Rev.* **122**, 1813 (1961).
- [100] G. W. F. Drake, Phys. Rev. 181, 23 (1969).
- [101] R. K. VAN DEN EYNDE, G. WIEBES, and T. NIEMEYER, *Physica* **59**, 401 (1971).